TECHNISCHE UNIVERSITÄT WIEN
Vienna University of Technology

INSTITUT FÜR MECHANIK UND MECHATRONIK
Mechanics & Mechatronics

in collaboration with

Design of a nonlinear decoupling control strategy for an advanced Hardware-In-the-Loop system to assess implantable blood pumps

executed to obtain an academic degree as Master of Science
under supervision of

Univ.Prof. Dr. Stefan Jakubek
Department for Control and Process Automation
Vienna University of Technology

Marcus Granegger PhD.
Department of Cardiac Surgery
Medical University of Vienna

submitted to the Vienna University of Technology

Faculty of Mechanical and Industrial Engineering

by

Moritz Bender
11902081

Vienna, June 2023

Moritz Bender

Statutory Declaration

I declare that I have authored this thesis independently, that I have not used other than the declared sources / resources, and that I have explicitly marked all material which has been quoted either literally or by content from the used sources.

Vienna, June 2023

Moritz Bender

Acknowledgement

I would like to express my sincere gratitude to Prof. Stefan Jakubek, for the invaluable support and guidance during the time of my master's thesis. Your insightful advice and mentorship have been invaluable in shaping this research work.

I would like to thank my supervisor Marcus Granegger for the unwavering support and guidance. Your dedication and expertise have been a great motivation during the whole research work. I am grateful for the opportunity to work under your supervision and for the valuable experiences that I have gained from your mentorship.

Appreciation is also extended to the Cardiovascular Research and Engineering group, that supported my mission through their great interest, thoughtful advises and welcoming teamwork.

I want to extend my gratitude to Michaeal Röhrich for the supportive teamwork and access to his laboratory, which was the perfect working environment. I am thankful for your willingness to share your ideas, knowledge, and expertise which led to great solutions and for always being there to lend a hand whenever I needed it.

I want to especially thank my girlfriend for the love, and support during this period of my life. With your unwavering belief in me, you have been a constant source of strength and motivation.

Preface

This thesis follows on a project work [1], which presented a hardware-in-the-loop system to test implantable blood pumps based on a single-input single-output control structure. The conducted results of the project work provided the background and motivation for this thesis, to design and implement an advanced multiple-input multiple-output control structure for a novel mock circulatory loop.

While working on this thesis, a paper was prepared and submitted for publication, with the title "An atraumatic mock loop for realistic hemocompatibility assessment of blood pumps". This paper shares content with this thesis.

Abstract

Mock circulatory loops (MCL) have become a favorable platform for in-vitro testing of blood pumps. To date, conventional MCLs are not suitable to mimic realistic hemodynamic conditions without inducing hemolysis. Accordingly, in-vitro hemocompatibility assessment of blood pumps is limited to constant operating conditions that do not comply with the clinical application. The aim of this thesis was to develop an atraumatic MCL based on a hardware-in-the-loop concept (H-MCL) that allows hemocompatibility examinations under realistic pressure and flow conditions. The novel atraumatic H-MCL was designed for a low blood volume suitable for one blood bag (450±50 mL), with hemocompatible materials, atraumatic sensors and actuators, and a heating module in compliance with the standards of the American Society for Testing and Materials. These design choices required an advanced control structure, to control the pressures and the blood level within the system, based on a cardiovascular model that is calculating the hemodynamic response (new set pressures) to the current pump support (measured flow rate): To ensure physiologic reference tracking and to account for inherent coupling effects a decoupling pressure control was derived by feedback linearization and dynamic extension. Moreover, the level control was addressed by an optimization task, which provides a feasible control trajectory to overcome periodic loss of controllability and to ensure atraumatic actuator effort. As blood pump, the HeartMate 3 (HM3) was deployed to evaluate the H-MCL's accuracy at characteristic hemodynamic conditions within partial and full support settings, which were assessed for different dynamics in simulative and experimental studies. With the novel control approach all hemodynamic scenarios were replicated with marginal coupling effects while the mean fluid level consistently met the target value. Of note, this quality could not be achieved with a SISO control approach. The presented novel atraumatic design extends state-of-the-art H-MCLs[1] and enables hemocompatibility assessment of blood pumps within realistic hemodynamic conditions.

[1] A second design was described within this thesis, which is characterized by the same low-volume design, yet with an additional pump as known from state-of-the-art H-MCLs. This features analogously a control structure based on the method of feedback linearization and dynamic extension, not hampered by periodic loss of controllability. With this decoupling control structure the conducted hemodynamic scenarios were replicated with marginal coupling effects and steady fluid levels. This introduces an advanced control structure for state-of-the-art H-MCL designs.

Kurzfassung

Hybride Testkreisläufe (HTK) stellen eine verbreitete Plattform für präklinische Untersuchungen von Blutpumpen dar. Dennoch sind herkömmliche Testkreisläufe bisher nicht in der Lage realistische hämodynamische Bedingungen zu reproduzieren, ohne dass zusätzliche Blutschädigung durch verwendete Komponenten entsteht. Dies beschränkt in-vitro Hämokompatibilitätsuntersuchungen von Blutpumpen auf statische Experimente, die die klinische Anwendung nicht realistisch wiedergeben. Das Ziel dieser Arbeit ist die Entwicklung eines atraumatischen Testkreislaufs, auf der Grundlage eines Hardware-in-the-Loop Konzeptes, um in-vitro Hämokompatibilitätsbetrachtungen unter realistischen hämodynamischen Bedingungen zu ermöglichen. Dieser neuartige atraumatische Testkreislauf ist für eine geringe Blutmenge von 450±50 mL ausgelegt, wobei zwei Reservoire, Schlauchelemente und die zu untersuchende Blutpumpe die einzigen Komponenten mit direktem Blutkontakt darstellen. Diese Designmaßnahmen orientieren sich an aktuellen Standards der American Society for Testing and Materials. Das neue Hardware-Design erfordert eine fortschrittliche Regelungsstrategie um die Drücke und Füllstände des Systems zu regeln, zugehörige Referenzdrücke werden dabei auf der Basis der aktuellen Unterstützung der Blutpumpe durch ein Modell des kardiovaskulären Systems berechnet. In diesem Rahmen wird eine entkoppelnde nichtlineare Regelungsstrategie für die Systemdrücke entworfen, um internen Kopplungseffekten entgegenzuwirken und eine hohe Regelgenauigkeit sicherzustellen. Die Regelungsstrategie basiert auf der Methode der globalen Linearisierung und wird durch einen Regelungsansatz für die Füllstandshöhe der Reservoirs ergänzt. Mit dem atraumatischen Design ist die Füllstandshöhe periodisch nicht regelbar. Diese Problematik wird mit Hilfe eines Optimierungsproblems adressiert, woraus eine Regeltrajektorie resultiert, die den Füllstand bei minimaler Aktuatorbetätigung sicher innerhalb der Randbedingungen führt. Um die Genauigkeit des neuen HTKs zu evaluieren werden typische hämodynamische Zustände von Patienten die mit einem HeartMate 3 (HM3) unterstützt werden simulativ und experimentell nachgebildet. Die untersuchten hämodynamischen Zustände entsprechen Patienten die teilweise oder vollständig mit einem HM3 entlastet werden, wobei unterschiedliche Herzfrequenzen berücksichtigt sind – diese Zustände werden durch die entworfene Regelungsstrategie mit marginalen Kopplungseffekten und hoher Genauigkeit abgebildet, wobei der Füllstand stabil um den Sollwert schwankt. Diese Genauigkeit lässt sich in diesem Rahmen nicht mit herkömmlichen Eingrößenregelungen abbilden. Der präsentierte atraumatische HTK erweitert den Stand der Technik und ermöglicht Hämokompatibilitätsuntersuchungen von Blutpumpen unter realistischen hämodynamischen Zuständen.

Contents

List of Figures

List of Tables

1 Introduction

Today, cardiovascular disease (CVD) is one of the leading health challenges in developed countries, in the EU solely, about 49 million people live with CVD. Within CVD, heart failure (HF) is a common but complex diagnosis with a prevalence that is predicted to rise in the upcoming decades, due to an aging population and improved treatment of acute cardiac events [2]. According to the New York Heart Association (NYHA), HF is classified starting from class I, when patients are not physically limited, ending with class IV, when patients are unable to carry out physical activity with dyspnea at rest [3]. At end-stage (class IV) HF patients most treatment methods have been exhausted, and a heart-transplantation becomes the therapy of choice. This therapy is increasingly challenged by a mismatch of recipients and donors, e.g. Eurotransplant reported 1150 patients on the active heart transplant list facing only 572 donor organs in 2021 [4].

Mechanical circulatory support (MCS) addresses this imbalance: such devices provide a vital treatment option as bridge-to-transplantation and thus significantly increase survival and quality of life of the patient. The largest share of MCS devices implanted in the recent years are rotodynamic blood pumps (RBP) in form of left ventricular assist devices (LVAD). LVADs relief the heart by unloading the left ventricle and directing the blood directly to the aorta, which raises the cardiac output and improves the supply of organs and body tissue. Due to technical improvements, LVADs are increasingly used as destination therapy, with survival rates about 80% one year, and 70% two years after implantation [5, 6], which also enables a valuable long-term treatment option when patients are not eligible for transplantation. However, only 30% of LVAD patients are not suffering from severe adverse events one year post implantation [5, 6]. Among others, this can be attributed to the risk of severe hemocompatibility related adverse events (HRAEs), e.g. pump thrombosis and gastrointestinal bleeding, which restrict the clinical outcome [6, 7].

The high number of HRAEs with RBPs points up that ongoing research is needed: Today, the hydraulic conception based on classical turbomachinery for optimized efficiency at one defined operating point represents one important limitation of current RBPs, since this conception results in potentially disturbed flow regimes in off-design conditions [8]. The assumption of an idealized constant mode of operation does not comply with the clinical application, as LVAD support addresses a diverse group of patients and consequently a wide range of hemodynamic conditions: The characteristic arterial and pulsatile left ventricular pressures cause dynamic changes in the pumps head pressure, which affects the pump flow rate and frequently leads to off-design operation. Such off-design operation of LVADs is observed within 50% of the

cardiac cycle [9] leading to impaired pump hemocompatibility [10, 11, 12] and an increased risk for adverse events [11, 13, 14].
Currently, the lack of suitable experimental models impedes investigation of blood trauma mechanisms under realistic hemodynamic settings. Accordingly, in-vitro analysis of hemocompatibility is still standardized as experiment with constant flow and pressure conditions [15, 16]. Although a wide range of mock circulatory loops (MCL) was suggested [17], none of the published setups is designed to replicate realistic hemodynamics without inducing hemolysis by improper design features (e.g. artificial valves [18] and additional pumps [19]).
In compliance with the standards of the American Society for Testing and Materials (ASTM) [15, 16], requirements for the design of an atraumatic MCL include: consistently hemocompatible materials, sensors, actuators and heating components without blood contact, and a low volume design which allows the use of one standard blood bag (450±50 mL).
Today, advanced MCLs are based on a hardware-in-the-loop (HIL) setup as described by Ochsner et al. [19]. Such setups are referred to as hybrid MCLs (H-MCLs) and characterized by a real-time communication between a numerical model of the cardiovascular system and the physical RBP under investigation: The RBP is placed between two characteristic reservoirs, which represent an interface that is mimicking a physiologic environment for the RBP, while the numerical model of the cardiovascular system is calculating the hemodynamic response to the current level of pump support. In line with the physiological relationships the flow rate of the RBP is affected by the present hemodynamic pressures, this flow rate is measured and fed back to the cardiovascular model, which allows the calculation of a hemodynamic response in the form of a new set of pressures. This interaction between the RBP and the cardiovascular model is enabled by a set of sensors and actuators which create a multiple-input multiple-output (MIMO) system. Such system is characterized by inherent coupling effects (e.g. one input affects multiple outputs). Conventional H-MCLs rely on single-input single-output (SISO) control strategies [19], where coupling effects are reduced by hardware settings e.g. large volumes and long tubing to increase inherent resistances. Further, additional pumps are used to control the reservoir levels. Yet, such design choices do not comply with the requirements for an atraumatic H-MCL.

The aim of this thesis was to demonstrate a novel atraumatic H-MCL design, which enables hemocompatibility assessment of RBPs under realistic hemodynamic conditions, which to date has not been studied in the open literature: The novel H-MCL is similarly based on a HIL setup, yet incorporates all requirements for an atraumatic setup. To balance the fluid within the system a pinch valve is implemented replacing additional pumps that were required in conventional H-MCLs. During the development of this atraumatic design, initially a SISO control structure was implemented [1] as proposed in the literature [19], which showed severe coupling effects within the system (cf. Fig. 1.1), leading to substantial reference-tracking errors. Therefore an advanced control strategy based on feedback linearization was chosen, to decouple the system and to account for inherent nonlinearities of the system. The advanced control strategy further considers atraumatic pinch valve control, which was derived from an optimization task.

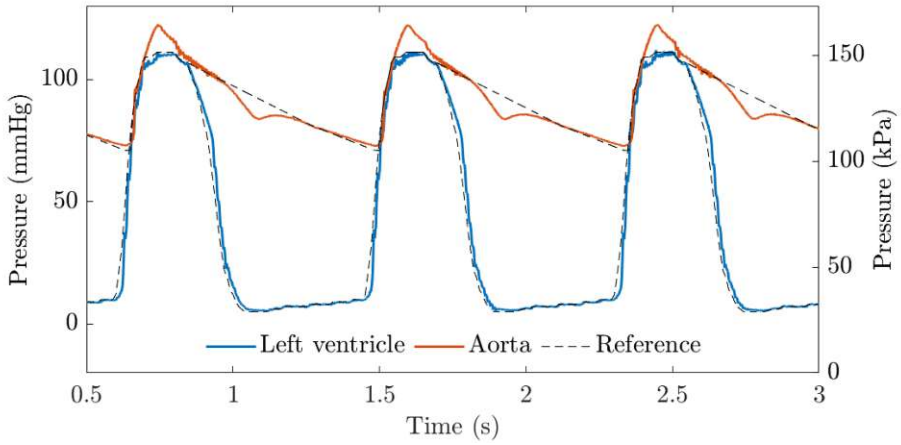

Figure 1.1: Reference tracking of measured left ventricular and aortic pressures with a conventional SISO control approach. [1]

The performance of this novel control strategy was assessed in a simulative and experimental study by comparing the atraumatic design with a similar (low-volume) state-of-the-art design where a gear pump was used for level control. Within these studies, realistic hemodynamic conditions were replicated, including partial support and full support conditions with different heart rates.

This thesis is organized as follows: Material and Methods includes a description of the novel H-MCL design with its hardware, numerical models of relevant components including a model of the cardiovascular system and the RBP under investigation, the control strategy based on the methodology of feedback linearization, and the description of the experiments conducted. Results and Discussion present the overall performance examined from the conducted experiments and simulations based on the described hemodynamic conditions. Finally, the Conclusion is summarizes the achievements made with the novel atraumatic MCL and its potential for future studies.

Of note, appendix A provides valuable information on the background of the research field which addresses readers without biomedical engineering background.

2 Materials and Methods

Within this thesis two design variations are presented: A *state-of-the-art* design, characterized by a gear pump, which enables a wide range of hemodynamic experiments without blood as working fluid. And the *atraumatic* design highlighted by a pinch valve, which enables hemocompatibility assessments of RBPs with blood as working fluid. Other design features than the hydraulic actuators were chosen identically for both design variations.

For the development of an atraumatic H-MCL, novel features and requirements had to be considered in the hardware design:

- Human blood is not available in any quantity and is subject to ethical questions. In compliance with the ASTM standards [15, 16], the design has to be suitable for one standard blood bag (450±50 mL).
- Blood must be kept at body temperature (37°C) to ensure adequate results.
- The sensors and actuators must be chosen without direct blood contact to ensure atraumatic properties.
- The setup must have small blood contacting surfaces with consistently hemocompatible properties.

The hardware adaptions implemented for an atraumatic H-MCL also resulted in new requirements addressing the control strategy:

- With the low volume design non-physiologic strong coupling effects occurred within the system, therefore a decoupling control strategy is necessary.
- The decoupling control must achieve fast and precise reference tracking of the hemodynamic pressures to ensure physiologic conditions.
- The blood level must be balanced with marginal actuator effort (pinch valve) to ensure atraumatic properties.

To achieve all requirements for an atraumatic H-MCL, a four stage approach was chosen: First, the setup was iteratively optimized. Second, a nonlinear model of the system was derived, including the numerical models of the cardiovascular system, the RBP under investigation and the numerical-hydraulic interface. Third, an advanced decoupling control strategy was derived based on the novel hardware choices. And fourth, the performance was evaluated within a simulative and experimental assessment.

Table 2.1: Clinical convention and SI units with its conversion factors

	Clinical	SI	Conversion factor
Pressure	mmHg	Pa	1 mmHg = 133.322 Pa
Flow rate	L/min	m^3/s	1 L/min = 1,66667e-5 m^3/s
Volume	L	m^3	1 L = 0,001 m^3
Speed	rpm	1/s	1 rpm = 0.0166667 1/s

Of note, the clinical convention is not using SI units. As this thesis addresses a clinical subject all parameters are stated according to the clinical convention. A summary of frequently used units and its conversion factor is given in Table 2.1.

2.1 Hardware

The novel H-MCL design is described, considering both hardware variations (*state-of-the-art* and *atraumatic* design) by outlining their similarities and dissimilarities explicitly. The hardware of the state-of-the-art design (Fig. 2.2a) and the atraumatic design (Fig. 2.2b) differs only within the hydraulic subsystem and is described in more detail in [1].

Fig. 2.1 shows the implementation of the numerical-hydraulic interface of the novel H-MCL, with its sensors and actuators (yet without heating system). The setup consists of a transparent polypropylene box (SAMLA, IKEA, Netherlands, 780x560x180 mm / 55 L) that accommodates the hydraulic subsystem of the H-MCL and holds the fluid in case of leakage. A compact modular frame made of aluminum profiles is used for mounting and flexible arrangement of the pneumatic components (Profile 6 30x30, RS Components, United Kingdom, 860x600x730 mm). On the rear side, the power supply and connection boxes for the sensors and actuators of the HMC are mounted on a DIN rail. For safety reasons an emergency stop button (7) is placed on the top of the setup, that disconnects the pneumatic and hydraulic subsystems and allows to stop the current experiment.

Hydraulic system. Here the *state-of-the art* design is described as representative for both design variants, whereas different features of the *atraumatic* setup are appended. The hydraulic system describes a hydraulic loop, filled with 550±50 mL of working fluid (diluted blood volume from blood bag with 450±50 mL), that consists of two reservoirs (12) made from sealed cylindrical polycarbonate (Ø 75x3x130 mm), specifically designed for this setup. Interchangeable inlet and outlet ports, which are additive manufactured (Formlabs Form 3, Clear Resin V4), allow a flexible adaption to the RBP under investigation. Nondetachable connections are made by an UV-hardening glue (UHU LED Light Booster, Bolton Adhesives, Rotterdam, Netherlands). The reservoirs are placed upstream and downstream of the RBP under investigation (15) (here the Heartmate 3 ((HM3), Abbott Inc, Chicago, USA), replicating the left ventricle and aorta, respectively. The pumps inflow cannula is inserted directly

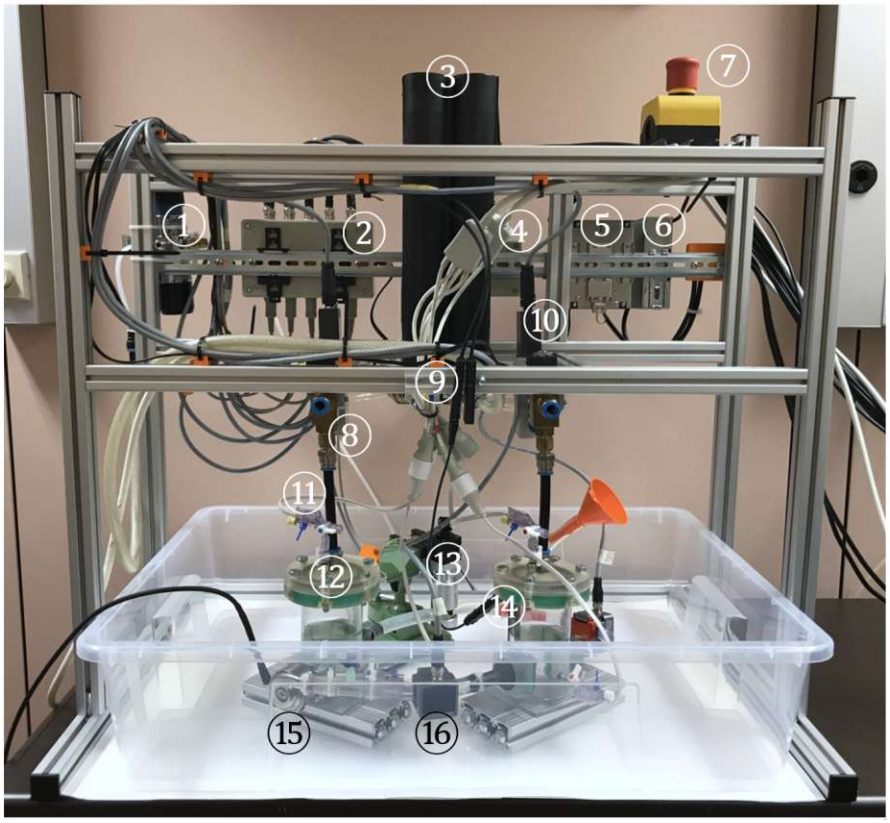

Figure 2.1: Front view of the hardware of the novel H-MCL and numbered components.

into the left ventricular reservoir, while the outflow is connected, in analogy to the clinical outflow graft, via a tube (200 mm) to the aortic reservoir. A clamp-on flow sensor (16) (Sonoflow CO55, Sonotec GmbH, Halle, Germany) is attached to the tube measuring the resulting pump flow rate. A backflow path closes the hydraulic loop which allows to maintain an equal fluid level within the system. Therefore a gear pump (UP3-R, MARCO s.p.a., Brescia, Italy) is implemented within the *state-of-the-art design*, that conveys a water-glycerol mixture adjusted to the viscosity of blood (3.5 cP). The pump is controlled by a motor controller (SMC 24v23, Pololu Corporation, Las Vegas, USA) and enables arbitrary flow rates up to 15 L/min in both directions, regardless of the current pressure gradient between the reservoirs. The gear pump allows precise adaptations of fluid flow and therefore a control of the blood level monitored by capacitive level sensors (14) (BCW0004, Balluff GmbH, Neuhausen, Germany) attached to the outside of both reservoirs. The level sensors can be calibrated by a corresponding amplifier (9) (BAE00LA, Balluff GmbH, Neuhausen, Germany). For all connections, hemocompatible 1/2 inch (12.7 mm) silicone and polyvinyl chloride (used with flow sensors) tubing is used.
With the *atraumatic design*, the hydraulic actuator is replaced with a proportional pinch valve (13) (HPPV-12, Resolution Air Ltd., Cincinnati, USA) and a second clamp-on flow sensor

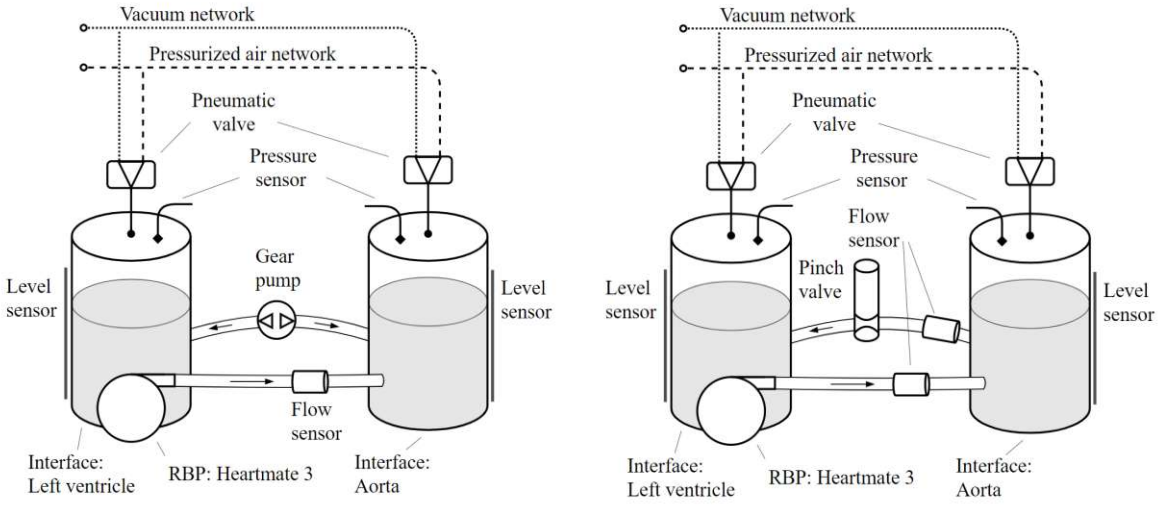

(a) State-of-the-art design.

(b) Atraumatic design.

Figure 2.2: The setup can be divided in a pneumatic part, consisting of the pneumatic supply network, two pneumatic proportional valves and two pressure sensors, and a hydraulic part, incorporating the RBP (Heartmate 3), one/two flow sensors, two level sensors and a gear pump/proportional pinch valve. The two reservoirs act as pressure-generating interfaces.

(Sonoflow CO55, Sonotec GmbH, Halle, Germany) that are attached to the tubing (250 mm), to allow the use of blood. Here the pinch valve represents a novel key component, which allows a defined backflow without blood contact. It consists of a hybrid bi-polar stepper motor, that receives square wave pulses from a driver (DRV-1, Resolution Air Ltd., Cincinnati, USA), and a hall effect sensor to detect a fully opened valve. The piston of the pinch valve is attached to the motor over an integral leadscrew, which converts one step of rotation into 0.012 mm linear movement. This pinch valve allows precise adaptations of blood flow driven by the present pressure difference between the reservoirs. Of note, the flow throughout the pinch valve is strongly dependent of the current pressures in the reservoirs, in the case of equal pressures there is no driving force to generate a flow in the backflow path, in this case the pinch valve has no impact on the system.

Pneumatic system. The pneumatic system is coupled with the hydraulic system via the reservoirs that act as a pressure-generating interface within the setup: Assuming an incompressible fluid, the fluid pressure in the reservoir is equal to the air pressure above its surface area plus the hydrostatic pressure of the fluid column. Therefore, the blood pressure can be precisely adjusted via the air mass flow in or out of the reservoir. To adjust the air mass flow, pneumatic proportional valves (10) (MPYE-5-1/4-010-B, Festo SE & Co. KG, Esslingen am Neckar, Germany) are implemented and connected to the pressurized air and vacuum

supply tanks (3). These polymer tanks (850 mL) act as a capacitance in the system and are filled by the pressurized air and vacuum supply network of the laboratory, limited by a pressure reducer (1) (Linde plc, Dublin, Ireland) (adjusted to 0.65 bar) and suitable relief valves (Zg.-Nr.: 1831 and 91-2508-4, Niezgodka GmbH, Hamburg, Germany) to a relative pressure of approximately +510 mmHg and -380 mmHg, respectively. At the end of the pneumatic network, safety valves in form of 2-way solenoid valves (8) (Typ 3V4-EF-V, Drumag GmbH, Bad Säckingen, Germany) are placed, that enable a leakproof disconnection between the hydraulic and pneumatic system to prevent damage of the components. The pneumatic connections are made by pneumatic quick couplings for pneumatic tubing of Ø 12 mm. The current pressure in the reservoirs is measured by clinical pressure transducers (11) (TruWave, Edwards Lifesciences Corp., Irvine, CA, USA; measurement error ±1 mmHg) suitable for the use with blood.

Heating system. For the use of blood, the system is extended by a heating concept: Therefore the assembly is placed under a transparent air-tight dome (800x800x800 mm) made of polyvinyl chloride, which has a large closable opening to access the hydraulic loop during experiments. The air temperature inside the dome is monitored by a temperature sensor (Pt100, E-4,5x17-Pt-3L-B-2Ts-M6, -90 to +200°C) and kept at 37°C by a temperature controller (A-senco TR-81, Pohltechnik.com GbR, Essingen, Germany) which controls a heat gun (ELEKTRON, Leister Technologies AG, Kaegiswil, Switzerland) that is inflating the dome with warm air. This heating concept is meant to maintain a defined blood temperature and is not well suited to overcome large temperature differences.

Power supply and external connections. The power supply of the system is implemented in two customized connection boxes, which ensure safe and clear wiring. At the same time they contain necessary electrical circuits and controllers, that are placed inside in a well-protected manner. A set of 5-pin DIN plugs for links within the system and BNC sockets for external connection, allow an easy connection of all parts. Connection box A (4) is powered by its own power supply unit (5) ((24V, 20A), S8VK-C48024, OMRON Coorporation, Kyoto, Japan) and connects the 2-way solenoid safety valves and the gear pump used within the state-of-the-art design. These are the critical actuators that are shut off by the emergency stop button of the test bench. Connection box B (2) is connected to a second power supply unit (6) ((24V, 5A), TRIO-PS1AC/24DC/5, Phoenix Contact GmbH, Wien, Austria) that connects all other sensors and actuators, including the pneumatic proportional valves, the level sensors, the flow sensors and the pinch valve. The wiring diagrams of the connection boxes are shown in the appendix by Fig. B.1 and Fig. B.2.
The sensor and actuator signals are processed by a dSpace MicroLabBox (dSpace GmbH, Paderborn, Germany), that is running the control strategy described in section 2.3 and a numerical model of the cardiovascular system (virtual patient) as described in section 2.2.1. This is implemented and compiled in MATLAB Simulink (The MathWorks, Natrick, MA, USA) with a fixed step Backward Euler type solver and a step size of 0.0005 s.

2.2 Modelling

As a basis for control design and simulations prior to experimental application, all components of the hybrid MCL were modelled numerically, including the cardiovascular model, the RBP under investigation (HM3), and the hydraulic-pneumatic interface characterized by the described hardware.

2.2.1 Model of the cardiovascular system

The cardiovascular system is modelled based on a modified elastance model from Colacino et al. [20] for the left heart. This non-linear time-varying elastance model describes the ventricular contraction. Accordingly, the left ventricle is expressed by the nonlinear elastance model $E(t)$ and a non-linear pressure-volume relationship $\phi(V_{LV}(t), t)$, which includes both end-systolic pressure-volume relationship (ESPVR) and end-diastolic pressure-volume relationship (EDPVR) terms ($\phi_S(V_{LV}(t))$ and $\phi_D(V_{LV}(t))$)

$$P_{LV}(t) = P_0 + \phi(V_{LV}(t), t) = P_0 + \phi_D(V_{LV}(t)) + \phi_S(V_{LV}(t))E(t), \tag{2.1}$$

where P_{LV} and V_{LV} are the left ventricular pressure and volume, respectively, with the corresponding time derivatives and the pressure parameter P_0. Analogously, the left atrium is described with a time varying elastance model for the left atrium $E_A(t)$ and the corresponding pressure-volume relationship $\phi_A(V_{LA}(t), t)$. This can be visualized as nonlinear time-varying capacity of each chamber. Further the valves of the left heart are modelled, based on characteristic resistive and inductive terms.
Together with the measured flow rate of a blood pump that unloads the left ventricle and directs the blood directly to the aorta, an open loop circulation is formed that simulates a realistic hemodynamic response of a left heart supported by a RBP. The numerical model is implemented in MATLAB Simulink based on the electric analogy depicted in Fig. 2.3.

In analogy to Boës et al. [9], two parameter sets were chosen to mimic realistic hemodynmic conditions of full support (characterized by a permanently closed aortic valve) and partial support (where blood is ejected to the aorta via the aortic valve). The model parameters were adapted to match data from Gupta et al. [21], which is described by a heart rate of 91 bpm, a left atrial pressure of 13 mmHg, an aortic pressure of 84 mmHg and a right atrial pressure of 10 mmHg. Further partial and full support differ in cardiac contractility, where the peak pressure of the nonlinear ESPVR was changed to 92.5 mmHg and 40 mmHg, respectively. The RBP speed was adapted to achieve a total cardiac output (composed of the displaced volume by the RBP and the ejected volume by the left ventricle) of 4.6 L/min in both conditions, which lead to a pump flow of 2.3 L/min (4450 rpm) in partial support and 4.6 L/min (5450 rpm) in full support condition. The simulated cardiac cycle resulting from partial and full support is shown in Fig. 2.4. To further assess the dynamic performance of the system, a slower and a faster heart rate (60 bpm and 120 bpm) compared to the characteristic heart rate (91 bpm) were investigated.

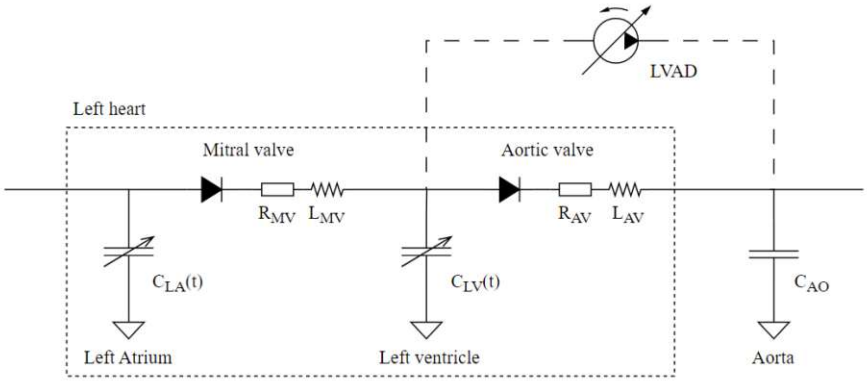

Figure 2.3: Electrical analog of the open loop model of the left heart including the schematic implementation of LVAD support.

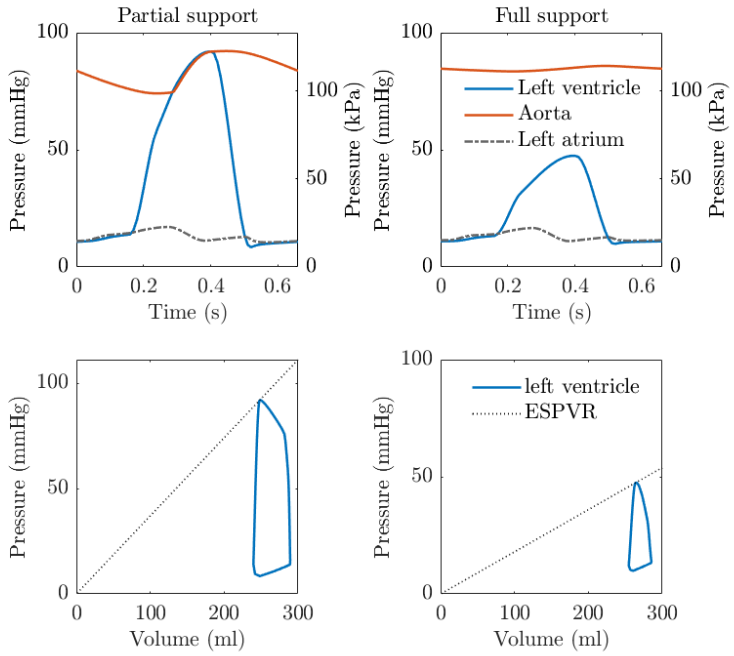

Figure 2.4: One cardiac cycle of partial-support and the full-support condition (simulated). The top row shows left ventricular, aortic and left atrial pressures, the bottom row shows the pressure-volume loop for the corresponding RBP unloading.

2.2.2 Model of the HeartMate 3

As the HM3 is based on a radial rotodynamic pump design, principles from turbomachinery can be used to derive a numerical model. Based on Euler's pump equation, a mathematical relation between the head pressure $H = H_{eul}$, the operating speed n, and the resulting flow rate Q_p can be derived. Boës et al. [9] suggested and validated such model, which further considers friction losses H_{fri}, incidence losses H_{inc} in off-design operating conditions, part-load recirculations H_{rec} blocking the blade channel, and the fluid inertia H_{dyn}. Combining these effects one obtains an expression for the head pressure H of the HM3

$$H = H_{eul} - H_{fri} - H_{inc} - H_{dyn} + H_{rec}, \tag{2.2}$$

which results in

$$H = a\,n^2 - R_1\,n\,Q_p - R_2\,Q_p^2 - L_p\,\frac{d}{dt}Q_p + \begin{cases} 0 & Q_p > q_{inf} \\ R_{rec}\,(Q_p - q_{inf})^2 & Q_p < q_{inf} \end{cases}. \tag{2.3}$$

With this the pump flow Q_p can be expressed as a differential equation by

$$\begin{aligned} \frac{d}{dt}Q_p = \frac{1}{L_p}\Bigg(& a\,n^2 - R_1\,n\,Q_p - R_2\,{Q_p}^2 - H \\ & + \begin{cases} 0 & Q_p > q_{inf} \\ R_{rec}(Q_p - q_{inf})^2 & Q_p < q_{inf} \end{cases}\Bigg), \end{aligned} \tag{2.4}$$

where $a, R_1, R_2, R_{rec}, k_{inf}$ are static parameters of the HM3, $q_{inf} = k_{inf}\,n$ is the inflection flow rate with a linear relationship to the speed n and L_p is the dynamic parameter for the fluid inertia. Furthermore, the pump's periphery describing the pressure loss H_{per} between the pump's outlet and the aortic reservoir was modelled by a resistive term due to fluid friction R_{per} and a frequency-dependent term due to fluid inertia L_{per}

Table 2.2: Model parameters of the HM3 from [9]

Parameters		Clinical		SI
k_{inf}	$2.596{\cdot}10^{-4}$	(L/min)/rpm	$2.596{\cdot}10^{-7}$	$(m^3/s)/(1/s)$
a	$3.458{\cdot}10^{-6}$	mmHg/rpm^2	1.660	Pa s^2
R_1	$-7.295{\cdot}10^{-4}$	mmHg/(rpm L/min)	$-3.501{\cdot}10^{5}$	Pa/(m^3/s^2)
R_2	2.245	mmHg/(L/min)^2	$1.078{\cdot}10^{12}$	Pa/(m^3/s)^2
R_{rec}	3.580	mmHg/(L/min)^2	$1.718{\cdot}10^{12}$	Pa/(m^3/s)^2
L_p	17.00	(mmHg s^2)/L	$2.266{\cdot}10^{6}$	(Pa s^2)/m^3
R_{per}	$1.244{\cdot}10^{-1}$	mmHg/(L/min)^2	$5.971{\cdot}10^{10}$	Pa/(m^3/s)^2
L_{per}	13.38	(mmHg s^2)/L	$1.784{\cdot}1^{6}$	(Pa s^2)/m^3

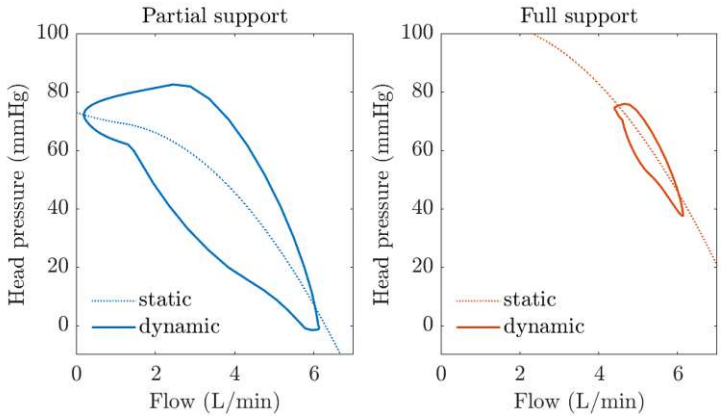

Figure 2.5: Static [9] and dynamic (simulated) HQ curve of the HM3 for partial (4450 rpm) and full (5450 rpm) support, respectively.

$$H_{per} = -L_{per}\,\frac{d}{dt}Q_p + \begin{cases} -R_{per}\,Q_p^2 & Q_p < 0 \\ R_{per}\,Q_p^2 & Q_p > 0 \end{cases} . \tag{2.5}$$

The parameter values are stated in Tab. 2.2, resulting in a RMSE of 2.5 mmHg (static) and 0.43 ±0.15 L/min (dynamic) [9]. Fig. 2.5 depicts the static HQ curves from [9] together with the dynamic HQ curve of the HM3 for the partial and full support condition as described in 2.2.1.

2.2.3 Model of the mock circulatory loop

To model the novel H-MCL the interaction between the pneumatic and hydraulic subsystem was of particular interest. One simplified assumption was made by neglecting temperature-dependent terms given that the whole system is tempered to 37°C.
Fig. 2.6a and Fig. 2.6b introduce important variables describing the system for the state-of-the-art and the atraumatic design, respectively.

Pneumatic system. The pressurized air in reservoir i is described by the ideal gas law

$$p_i\,V_i = R\,T\,m_i\,. \tag{2.6}$$

With the time derivative of the ideal gas law one obtains

$$\frac{d}{dt}p_i\,V_i + p_i\,\frac{d}{dt}V_i = R\,T\,\frac{d}{dt}m_i\,, \tag{2.7}$$

where $\frac{d}{dt}m_i = \dot{m}_i$ is the air mass flow to the reservoir, and $V_i = V_0 - A\,h_i$ is the volume of air in dependency of the fluid level h_i. Further parameters are the specific gas constant R, the air temperature T, the reservoir cross-sectional area A, and the volume of the empty reservoir V_0. With these terms the air pressure inside the reservoir results in

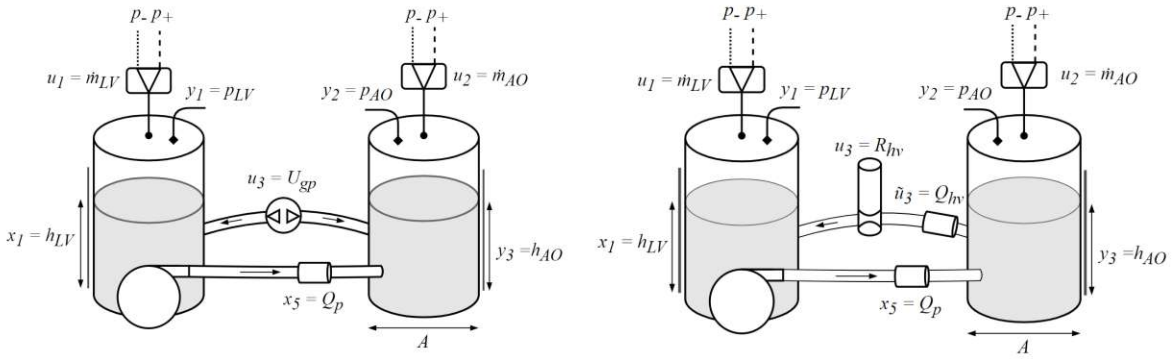

(a) State-of-the-art design.

(b) Atraumatic design.

Figure 2.6: System description with input, state and output variables.

$$\frac{d}{dt}p_i = \frac{RT}{V_0 - A\,h_i}\,\dot{m}_i - p_i\,\frac{-A\,\frac{d}{dt}h_i}{V_0 - A\,h_i}\,. \tag{2.8}$$

The mass flow rate $\dot{m}_i$ through the pneumatic proportional valve was modelled according to ISO 6358 and Beater et al. [22] and can be distinguished according to the normalized valve slide x_{pv} in a negative $\dot{m}_{i-}$ (vacuum supply) and positive $\dot{m}_{i+}$ (pressure supply) flow rate

$$\dot{m}_i = \begin{cases} \dot{m}_{i+} & x_{pv,i} \in [0,1] \\ \dot{m}_{i-} & x_{pv,i} \in [-1,0) \end{cases}. \tag{2.9}$$

The mass flow rate is dependent on the valve slide $x_{pv,i}$ and the pressure ratio downstream and upstream of the valve. With the critical pressure ratio b the flow rate is divided into two cases: The flow rate equals the local speed of sound for $\frac{p_i}{p_+} \leq b$ and $\frac{p_-}{p_i} \leq b$, respectively (choked flow), whereas it has subsonic speed for $\frac{p_i}{p_+} > b$ and $\frac{p_-}{p_i} > b$, respectively (subsonic flow)

$$\dot{m}_{i+} = \begin{cases} C_i(x_{pv,i}, p_i)\, p_+\, \rho_0 \sqrt{\frac{T_0}{T}} & \frac{p_i}{p_+} \leq b \\ C_i(x_{pv,i}, p_i)\, p_+\, \rho_0 \sqrt{\frac{T_0}{T}} \sqrt{1 - \left(\frac{\frac{p_i}{p_+} - b}{1-b}\right)^2} & \frac{p_i}{p_+} > b \end{cases}, \tag{2.10a}$$

$$\dot{m}_{i-} = \begin{cases} C_i(x_{pv,i}, p_i)\, p_i\, \rho_0 \sqrt{\frac{T_0}{T}} & \frac{p_-}{p_i} \leq b \\ C_i(x_{pv,i}, p_i)\, p_i\, \rho_0 \sqrt{\frac{T_0}{T}} \sqrt{1 - \left(\frac{\frac{p_-}{p_i} - b}{1-b}\right)^2} & \frac{p_-}{p_i} > b \end{cases}, \tag{2.10b}$$

where $C_i(x_{pv,i}, p_i)$ is the sonic conductance, ρ_0 is the density of air at reference condition, T_0 is the temperature of air at reference condition and T is the upstream temperature of the air. The critical pressure ratio b of the valve can be treated as constant and was taken from the literature [22]. Further parameters are the supply pressure p_+, the supply vacuum p_-, and the reservoir pressure p_i.

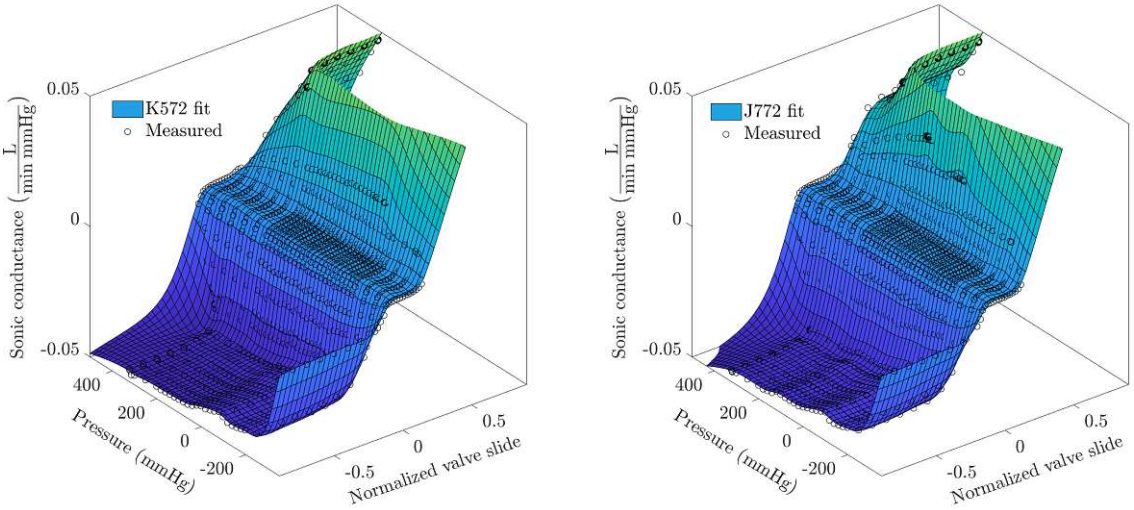

(a) Valve K572.

(b) Valve J772.

Figure 2.7: Sonic conductance of the proportional valves with respect to the normalized valve slide and pressure in the respective reservoir.

The sonic conductance $C_i(x_{pv,i}, p_i)$ was measured in dependence of the normalized valve slide x_{pv} and the pressure in the reservoir p_i, to represent inherent flow properties of the each proportional valve (K572 and J772). Fig. 2.7a and 2.7b show the identified fit of the sonic conductance for each proportional valve of the setup, further information on the identification is attached in appendix B.5. Characteristic pneumatic parameters of the model are stated in Table 2.4.

Hydraulic system. The fluid level in the reservoir i is described by a volume balance equation that includes the upstream Q_{up} and downstream Q_{down} flow of the reservoir

$$\frac{d}{dt}h_i = \frac{1}{A}\left(Q_{up} - Q_{down}\right), \tag{2.11}$$

where Q_{up} and Q_{down} refer to the flow rates through the RBP Q_p and the gear pump Q_{gp} (state-of-the-art design) or the pinch valve Q_{hv} (atraumatic design), respectively.

State-of-the-art design. The gear pump of the state-of-the-art design is a rotational displacement pump that is characterized by pumping a defined volume per revolution

$$Q_{gp} = \omega\, D_\omega\,, \tag{2.12}$$

where Q_{gp} is the fluid volume flow, ω is the rotational velocity of the pumps motor and D_ω is the displacement of the fluid. With an ideal model the torque produced is given as

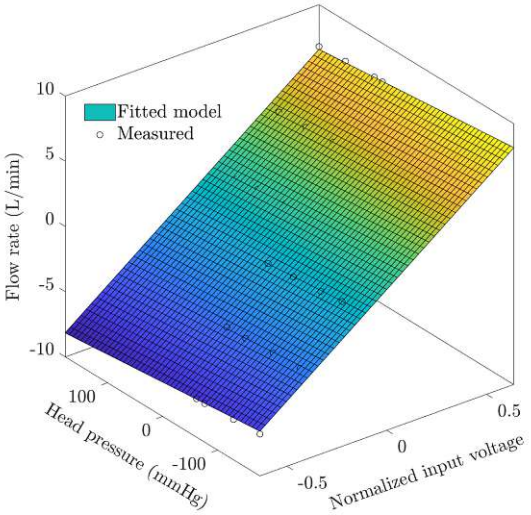

Figure 2.8: Fitted model of the gear pump flow rate with respect to the normalized pump voltage and the head pressure.

$$T_M = \Delta p_M \, D_\omega \,, \tag{2.13}$$

where Δp_M is the pressure difference between in- and outlet of the pump (= head pressure H) and T_M is the motor torque [23]. The rigid design of a gear pump allows high flow rates at high pressure gradients throughout the pump. A non-ideal model of the pump is marginally dependent on the present pressure difference due to a leakage flow through the pump. Leakage flow occurs due to small gaps in the pump design. To account for the leakage a pump model with respect to the current head pressure is chosen. As the datasheet of the pump does not provide information on the efficiency of the pumps motor and there is no information about the current rotational speed, the model is chosen in dependency of the pumps input voltage. The identified model of the gear pump has the form

$$Q_{gp} = p_{00} + p_{10}\, U + p_{01}\, H + p_{11}\, U\, H \,, \tag{2.14}$$

where U is the pumps input voltage and H is the pumps head pressure. The model parameters are stated in table 2.3, which result in a RMSE of 0.1699 L/min, further the static fit is shown in Fig. 2.8.

Atraumatic design. In compliance with Pennati et al. [24] the flow through the piping with attached pinch valve Q_{hv} can be modelled as lumped parameter model with resistive, inductive, capacitive, and geodetic terms. The compliance $C = \delta V / \delta p$ allows to account for a pipe that is not perfectly rigid. The volume of such component changes with the internal pressure leading to a different inlet and outlet flow rate. Here, this effect is neglected due

Table 2.3: Model parameters of the gear pump

Parameters	Clinical		SI	
p_{00}	-0.2625	L/min	$-4.375{\cdot}10^{-6}$	m^3/s
p_{01}	-0.004080	L/(min mmHg)	$-5.100{\cdot}10^{-10}$	$m^3/(s\,Pa)$
p_{10}	11.68	L/(min V)	0.0001947	$m^3/(s\,V)$
p_{11}	0.003047	L/(min V mmHg)	$3.809{\cdot}10^{-10}$	$m^3/(s\,V\,Pa)$

to a small pipe volume and comparatively rigid pipe characteristics. Further the geodetic term is neglected as the components are implemented at the same height. The pressure drop Δp_{hv} across the pinch valve is therefore obtained by resistive R_{hv} and inductive L_{hv} terms according to

$$\Delta p_{hv} = R_{hv}\, Q_{hv} + L_{hv}\, \frac{d}{dt} Q_{hv}\,. \tag{2.15}$$

The resistance parameter R_{hv} is not constant and can be described by the Darcy-Weisbach equation, which allows the calculation of the pressure drop in the tubing considering both pipe friction Δp_λ and additional losses due to the pinch valve Δp_ζ

$$\begin{aligned} \Delta p_R &= \Delta p_\lambda + \Delta p_\zeta \\ &= \lambda \frac{l_p}{d_p} \frac{\rho}{2} \left(\frac{Q_{hv}}{A} \right)^2 + \zeta(x_{hv}, Q_{hv}) \frac{\rho}{2} \left(\frac{Q_{hv}}{A} \right)^2 , \end{aligned} \tag{2.16}$$

where l_p and d_p are the length and the inner diameter of the pipe, ρ is the fluid density, λ is the friction factor, and $\zeta(x_{hv}, Q_{hv})$ is the variable loss coefficient of the pinch valve.
Depending on the present flow regime, the friction factor λ is determined from the Hagen-Poiseuille equation (laminar) or calculated with the Blasius equation (turbulent)

$$\lambda = \begin{cases} \frac{64}{Re} & \mathrm{Re} < 2000 \text{ (laminar)} \\ \frac{0.316}{Re^{0.25}} & \mathrm{Re} \geq 2000 \text{ (turbulent)} \end{cases} , \tag{2.17}$$

where λ is a function of the Reynolds number $\mathrm{Re} = \rho\, v\, d/\eta$, which is calculated by the flow velocity $v = Q_{hv}/A_p$, the dynamic viscosity η, and the characteristic length d of the component.
The varying loss coefficient $\zeta(x_{hv}, Q_{hv})$ of the pinch valve is determined from static experiments to map the characteristic resistance of the pinch valve as a function of the valve slide x_{hv} and the current flow Q_{hv}. With this a static model is fitted for the pressure loss Δp_ζ as depicted in Fig. 2.9.
The frequency dependent pressure difference Δp_L to accelerate and decelerate the fluid due to its inertia $L_{hv} = \rho l/A_p$ is expressed as

$$\Delta p_L = L_{hv}\, \frac{d}{dt}\, Q_{hv}\,. \tag{2.18}$$

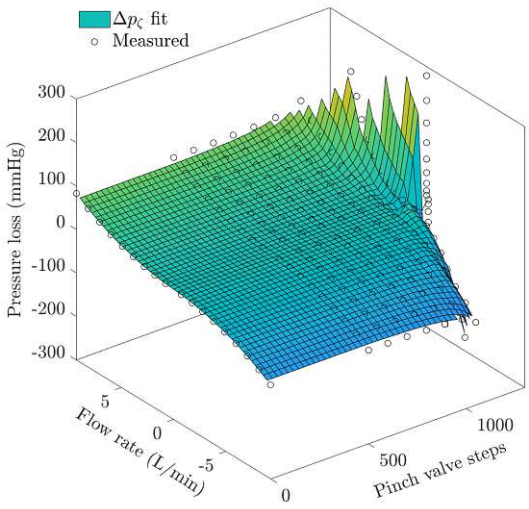

Figure 2.9: Fitted model of the pressure loss Δp_ζ due to the pinch valve with respect to the pinch valve position and the current flow rate.

Accordingly, the sum of (2.16) and (2.18) describes the pressure loss Δp_{hv} in the backflow path of the atraumatic design, and can be used to derive a differential equation for the pinch valve flow

$$\frac{d}{dt} Q_{hv} = \frac{1}{L_{hv}} \left(\Delta p_{hv} - \left(\lambda \frac{l}{d} + \zeta(x_{hv}, Q_{hv}) \right) \frac{\rho}{2} \left(\frac{Q_{hv}}{A} \right)^2 \right), \tag{2.19}$$

where Δp_{hv} equals the head pressure H of the RBP and comprises the air pressures p_i and the hydro-static pressure of the respective fluid column ($= \rho g h_i$) with the fluid density ρ and the acceleration due to gravity g in the reservoir i.
Originally these equations are developed for steady flows, yet according to [24] these are also valid for pulsatile flows when a sufficiently high mean flow is superimposed.

In combination with (2.4), these submodels result in a *set of coupled nonlinear differential equations* for the numerical-hydraulic interface representing the pressure and flow relationships within the left ventricular and aortic reservoir.

State-of-the-art design:

$$\frac{d}{dt}h_{LV} = \frac{1}{A}\left(Q_{gp} - Q_p\right) \tag{2.20a}$$

$$\frac{d}{dt}h_{AO} = \frac{1}{A}\left(Q_p - Q_{gp}\right) \tag{2.20b}$$

$$\frac{d}{dt}p_{LV} = \frac{R\,T}{V_0 - A\,h_{LV}}\,\dot{m}_{LV} + p_{LV}\,\frac{(Q_{gp} - Q_p)}{V_0 - A\,h_{LV}} \tag{2.20c}$$

$$\frac{d}{dt}p_{AO} = \frac{R\,T}{V_0 - A\,h_{AO}}\,\dot{m}_{AO} + p_{AO}\,\frac{(Q_p - Q_{gp})}{V_0 - A\,h_{AO}} \tag{2.20d}$$

$$\frac{d}{dt}Q_p = \frac{1}{L_p}\left(a\,n^2 - R_1\,n\,Q_p - R_2\,{Q_p}^2 - H_p + \begin{cases} 0 & Q_p > q_{inf} \\ R_{rec}(Q_p - q_{inf})^2 & Q_p < q_{inf} \end{cases}\right) \tag{2.20e}$$

.

Atraumatic design:

$$\frac{d}{dt}h_{LV} = \frac{1}{A}\left(Q_{hv} - Q_p\right) \tag{2.21a}$$

$$\frac{d}{dt}h_{AO} = \frac{1}{A}\left(Q_p - Q_{hv}\right) \tag{2.21b}$$

$$\frac{d}{dt}p_{LV} = \frac{R\,T}{V_0 - A\,h_{LV}}\,\dot{m}_{LV} + p_{LV}\,\frac{(Q_{hv} - Q_p)}{V_0 - A\,h_{LV}} \tag{2.21c}$$

$$\frac{d}{dt}p_{AO} = \frac{R\,T}{V_0 - A\,h_{AO}}\,\dot{m}_{AO} + p_{AO}\,\frac{(Q_p - Q_{hv})}{V_0 - A\,h_{AO}} \tag{2.21d}$$

$$\frac{d}{dt}Q_p = \frac{1}{L_p}\left(a\,n^2 - R_1\,n\,Q_p - R_2\,{Q_p}^2 - H_p + \begin{cases} 0 & Q_p > q_{inf} \\ R_{rec}(Q_p - q_{inf})^2 & Q_p < q_{inf} \end{cases}\right) \tag{2.21e}$$

.

Table 2.4: Model parameters of the H-MCL

Parameters	Clinical		SI	
p_+	510.0	mmHg	$1.693{\cdot}10^5$	Pa
p_-	-380.0	mmHg	$5.062{\cdot}10^3$	Pa
V_0			$5.441{\cdot}10^{-4}$	m^3
A			$4.185{\cdot}10^{-3}$	m^2
b			0.5283	-
l_p			0.2	m
d_p			0.0127	m
A_p			$1.267{\cdot}10^{-4}$	m^2

2.3 Control strategy

To control the setup, initially, a SISO control structure was derived in a preceding work [1] and implemented as suggested in conventional H-MCLs [19]. This allowed a stable operation of the novel H-MCL, however strong coupling effects were observed leading to periodical pressure errors that could not be eliminated completely.
To improve the control performance a decoupling control strategy was derived based on the method of feedback linearization and dynamic extension. Given the nonlinear model of the H-MCLs from (2.20) and (2.21) this MIMO control approach accounts for the nonlinearities of the system and ensures precise trajectory tracking of the hemodynamic pressures.
Further, considering the atraumatic design (2.21) atraumatic control behavior was demanded, which is defined by precise trajectory tracking of the hemodynamic pressures in combination with minimal effort of the pinch valve, which corresponds to marginal motion of the valve. To address this, the minimal possible valve motion was assessed in an optimization task, which indicated that a realistic cardiac cycle can be controlled by a constant valve opening. Considering these findings a suitable atraumatic and decoupling feedback control structure was derived.

2.3.1 Coupling effects

The coupling effects observed with a SISO control approach can be assessed by a simplified control loop with two inputs and outputs as shown in Fig. 2.10.

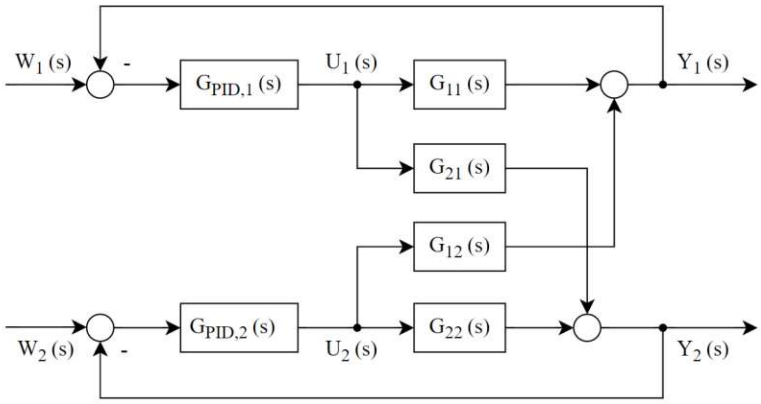

Figure 2.10: Block diagram of a control loop with two inputs, two outputs, and coupling effects. Based on [25]

In order to derive the corresponding transfer functions for the multivariate systems, the system equations (2.20) and (2.21) are used, where all inputs except for the pneumatic valve inputs and all outputs except for the two reservoir pressures are omitted. This results in two equal system descriptions for both design variants: The resulting model is linearized at a steady-state setpoint with equally filled and pressurized reservoirs, zero RBP speed and zero flow in

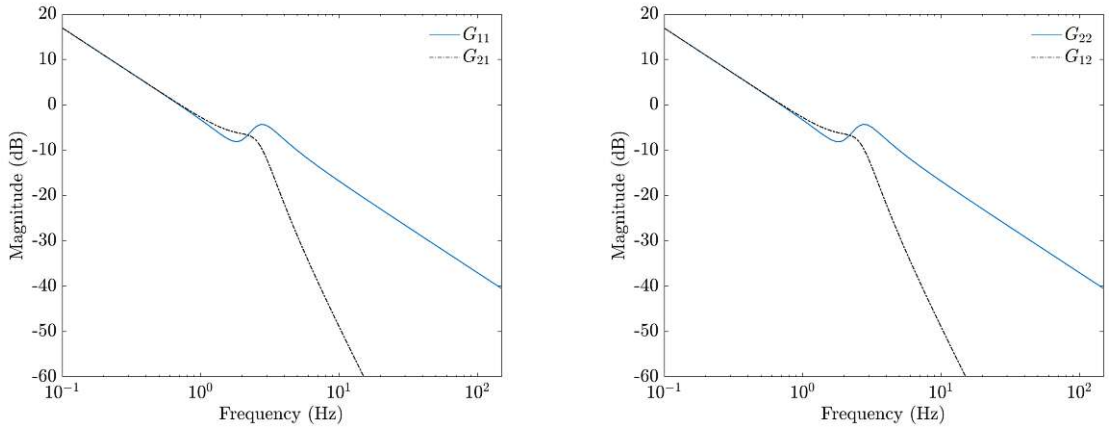

(a) Effect of input 1.

(b) Effect of input 2.

Figure 2.11: Magnitude plots of the transfer functions of the multivariate system.

the backflow path. The resulting transfer functions allow the investigation of the coupling effects between the two reservoirs, which are only connected by a blood pump (HM3) in standstill. The coupling is assessed by comparing the magnitude plots of diagonal (G_{12}, G_{21}) and off-diagonal (G_{11}, G_{22}) transfer functions (Fig. 2.11a and 2.11b). Exemplary, the effect of the first input is assessed and shown in Fig 2.12a and 2.12b.

a) Under the assumption of an ideal control performance of control loop 2, the effect on the first control loop can be expressed by the dynamic coupling factor K, which is defined as

$$Y_1(s) = G_{11}(s)\left[1 - \underbrace{\frac{G_{12}(s)G_{21}(s)}{G_{11}(s)G_{22}(s)}}_{K(s)}\right] U_1(s). \tag{2.22}$$

b) If $W_2 = 0$ is assumed the behavior of the second control loop can be described as

$$Y_2(s) = \underbrace{\left[\frac{G_{21}(s)}{1 + G_{PID,2}(s)G_{22}(s)}\right]}_{G_2(s)} U_1(s). \tag{2.23}$$

It becomes apparent that the cross-coupling effects are relevant up to a frequency of about 2.5 Hz, where the effect of the first input on the first output is damped and therefore has less impact on the output compared to higher frequencies. Further the second output is strongly affected by the first input in lower frequencies with a peak at approximately 2 Hz, this means that a pressure change in one reservoirs has strong influence on the pressure in the other reservoir due to the flow rate that can pass through the fluid gaps of the RBP. With higher frequency this effect diminishes due to the inertia of the fluid and the pressures can be assumed independent.

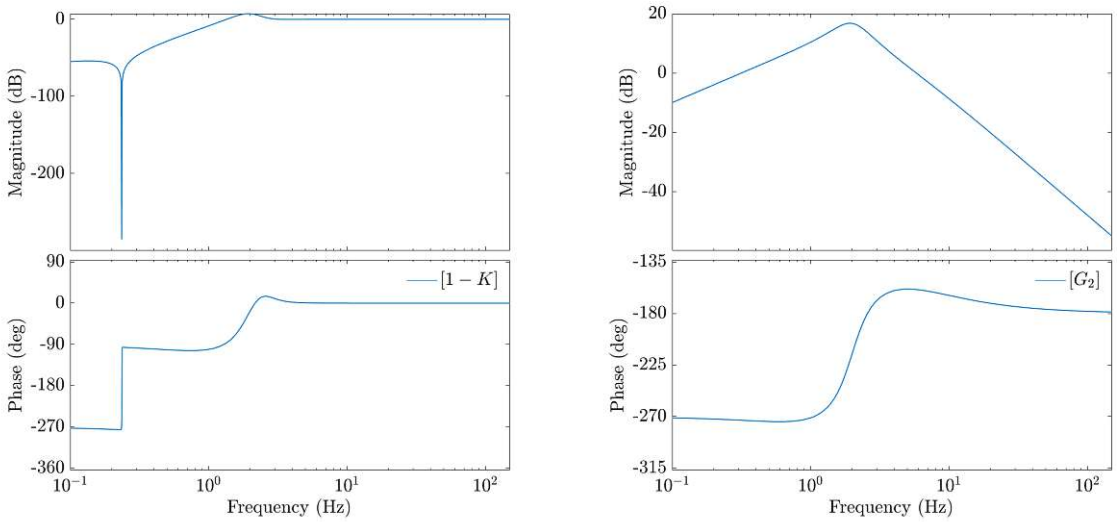

(a) Bode plot for first control loop.

(b) Bode plot for second control loop.

Figure 2.12: Frequency response of first and second output in dependency of the first input.

With a SISO control approach as proposed for conventional H-MCL designs [19], the frequency dependent coupling effects have clearly affected experimental studies with the novel low volume H-MCLs and the HM3. Therefore a decoupling control approach based on the method of feedback linearization was chosen.

2.3.2 Feedback Linearization

Feedback linearization describes a method in which a nonlinear state feedback controller is designed to compensate for all nonlinearities of the multivariate system, leading to an overall linear control loop [26, 27].
This is achieved by merging a state transformation of the nonlinear system with an input transformation, such that a linear and fully decoupled multivariate system is obtained. Consequently, each output is only affected by one input and linear methods can be used for controller design. The inverse transformation of this linear system and its linear control structure yields a decoupling nonlinear control law that compensates for the nonlinearities of the initial system.

To do so, a nonlinear multivariate system of the form

$$\begin{aligned} \dot{\mathbf{x}} &= \mathbf{f}(\mathbf{x}) + \mathbf{g}(\mathbf{x})\,\mathbf{u}, \\ \mathbf{y} &= \mathbf{h}(\mathbf{x}) \end{aligned} \tag{2.24}$$

is considered, with m-dimensional input vector $\mathbf{u}$ and output vector $\mathbf{y}$, and n-dimensional state vector $\mathbf{x}$.
The system is reformulated by applying the time derivative to each system output y_k

$$\begin{aligned}\dot{y}_k &= \frac{\delta h_k(\mathbf{x})}{\delta \mathbf{x}}\mathbf{f}(\mathbf{x}) + \sum_{j=1}^{m}\frac{\delta h_k(\mathbf{x})}{\delta \mathbf{x}}\mathbf{g}_j(\mathbf{x})u_j \\ &= L_{\mathbf{f}}h_k(\mathbf{x}) + \sum_{j=1}^{m} L_{\mathbf{g}_j}h_k(\mathbf{x})u_j,\end{aligned} \tag{2.25}$$

where $L_{\mathbf{f}}$ and $L_{\mathbf{g}}$ represent Lie derivatives, with respect to the scalar function $h(\mathbf{x})$ and the vector fields $\mathbf{f}(\mathbf{x})$ and $\mathbf{g}(\mathbf{x})$, respectively. In general, Lie derivatives are defined as the product of the gradient of a vector function $\mathbf{a}(\mathbf{x})$ and a scalar function $c(\mathbf{x})$ as

$$\begin{aligned}L_a c(\mathbf{x}) &= \frac{\partial c(\mathbf{x})}{\partial \mathbf{x}}\,\mathbf{a}(\mathbf{x}) = grad^T c(\mathbf{x})\,\mathbf{a}(\mathbf{x}), \\ L_a^k c(\mathbf{x}) &= \frac{\partial L_a^{k-1} c(\mathbf{x})}{\partial \mathbf{x}}\,\mathbf{a}(\mathbf{x}).\end{aligned} \tag{2.26}$$

In case of $L_{\mathbf{g}_j}h_k(\mathbf{x}) = 0$ (for all inputs $j = 1, 2, \ldots, m$), the first time derivative of the output y_k is not affected by the control inputs. Thus, the next time derivatives are computed until $L_{\mathbf{g}_j}h_k(\mathbf{x}) \neq 0$ is valid for at least one input u_j. Then the corresponding time derivative has the form

$$y_k^{(\delta_k)} = L_{\mathbf{f}}^{\delta_k}h_k(\mathbf{x}) + \sum_{j=1}^{m} L_{\mathbf{g}_j}L_{\mathbf{f}}^{\delta_k - 1}h_k(\mathbf{x})u_j, \tag{2.27}$$

where the time derivative δ_k is called the *relative degree* of the corresponding k^{th} output. The relative degree corresponds to the number of differentiations of the output y_k until one input u_j appears explicitly. By applying this to all outputs ($k = 1, 2, \ldots, m$) an *input-output relation* for the nonlinear multi-variable system is obtained

$$\begin{bmatrix} {y_1}^{(\delta_1)} \\ \vdots \\ {y_m}^{(\delta_m)} \end{bmatrix} = \underbrace{\begin{bmatrix} L_{\mathbf{f}}^{\delta_1}h_1(\mathbf{x}) \\ \vdots \\ L_{\mathbf{f}}^{\delta_m}h_m(\mathbf{x}) \end{bmatrix}}_{\mathbf{l}(\mathbf{x})} + \underbrace{\begin{bmatrix} L_{\mathbf{g}_1}L_{\mathbf{f}}^{\delta_1-1}h_1(\mathbf{x}) & \cdots & L_{\mathbf{g}_m}L_{\mathbf{f}}^{\delta_1-1}h_1(\mathbf{x}) \\ \vdots & \ddots & \vdots \\ L_{\mathbf{g}_1}L_{\mathbf{f}}^{\delta_m-1}h_m(\mathbf{x}) & \cdots & L_{\mathbf{g}_m}L_{\mathbf{f}}^{\delta_m-1}h_m(\mathbf{x}) \end{bmatrix}}_{\mathbf{J}(\mathbf{x})} \begin{bmatrix} u_1 \\ \vdots \\ u_m \end{bmatrix}. \tag{2.28}$$

It can be seen that the time derivative of each output of a multivariate system is linked to multiple inputs via the coupling matrix $\mathbf{J}(\mathbf{x})$. Therefore, the rank of the coupling matrix determines if the system outputs can be decoupled.

State-of-the-art design.
The nonlinear multivariate system of the state-of-the-art design (2.20) can be described by a suitable choice of input, state and output vectors (cf. Fig. 2.6a)

$$\mathbf{x} = \begin{bmatrix} h_{LV} \\ h_{AO} \\ p_{LV} \\ p_{AO} \\ Q_p \end{bmatrix}, \mathbf{u} = \begin{bmatrix} \dot{m}_{LV} \\ \dot{m}_{AO} \\ U_{gp} \end{bmatrix}, \mathbf{y} = \begin{bmatrix} p_{LV} \\ p_{AO} \\ h_{AO} \end{bmatrix}, \tag{2.29}$$

and the corresponding vector fields $\mathbf{f}(\mathbf{x})$, $\mathbf{g}(\mathbf{x})$, and $\mathbf{h}(\mathbf{x})$

$$\mathbf{f}(\mathbf{x}) = \begin{bmatrix} -\frac{x_5 - p_{00} + H(\mathbf{x})\, p_{01}}{A} \\ \frac{x_5 - p_{00} + H(\mathbf{x})\, p_{01}}{A} \\ -\frac{x_3\,(x_5 - p_{00} + H(\mathbf{x})\, p_{01})}{V - A\, x_1} \\ \frac{x_4\,(x_5 - p_{00} + H(\mathbf{x})\, p_{01})}{V - A\, x_2} \\ \frac{a\, n^2 - R_1\, n\, x_5 - R_2\, {x_5}^2 - H(\mathbf{x})}{L} \end{bmatrix}, \tag{2.30a}$$

$$\mathbf{g}(\mathbf{x}) = \begin{bmatrix} 0 & 0 & \frac{p_{10} - H(\mathbf{x})\, p_{11}}{A} \\ 0 & 0 & -\frac{p_{10} - H(\mathbf{x})\, p_{11}}{A} \\ \frac{R\,T}{V - A\, x_1} & 0 & \frac{x_3\,(p_{10} - H(\mathbf{x})\, p_{11})}{V - A\, x_1} \\ 0 & \frac{R\,T}{V - A\, x_2} & -\frac{x_4\,(p_{10} - H(\mathbf{x})\, p_{11})}{V - A\, x_2} \\ 0 & 0 & 0 \end{bmatrix}, \tag{2.30b}$$

$$\mathbf{h}(\mathbf{x}) = \begin{bmatrix} x_3 \\ x_4 \\ x_2 \end{bmatrix}, \tag{2.30c}$$

where $H(\mathbf{x}) = (x_4 - x_3 + \rho\, g\, x_2 - \rho\, g\, x_1)$ is the head pressure and $x_5 > q_{inf}$ is assumed. Subsequently, the input-output relation of the state-of-the-art design results in

$$\begin{bmatrix} \dot{y}_1 \\ \dot{y}_2 \\ \dot{y}_3 \end{bmatrix} = \underbrace{\begin{bmatrix} -\frac{x_3\,(x_5 - p_{00} + H(\mathbf{x})\, p_{01})}{V - A\, x_1} \\ \frac{x_4\,(x_5 - p_{00} + H(\mathbf{x})\, p_{01})}{V - A\, x_2} \\ \frac{x_5 - p_{00} + H(\mathbf{x})\, p_{01}}{A} \end{bmatrix}}_{\mathbf{l}(\mathbf{x})} + \underbrace{\begin{bmatrix} \frac{R\,T}{V - A\, x_1} & 0 & \frac{x_3\,(p_{10} - H(\mathbf{x})\, p_{11})}{V - A\, x_1} \\ 0 & \frac{R\,T}{V - A\, x_2} & -\frac{x_4\,(p_{10} - H(\mathbf{x})\, p_{11})}{V - A\, x_2} \\ 0 & 0 & -\frac{p_{10} - H(\mathbf{x})\, p_{11}}{A} \end{bmatrix}}_{\mathbf{J}(\mathbf{x})} \begin{bmatrix} u_1 \\ u_2 \\ u_3 \end{bmatrix}. \tag{2.31}$$

Atraumatic design.
Analogously, the nonlinear multivariate system of the atraumatic design (2.21) is described by a suitable choice of input, state and output vectors (cf. Fig. 2.6b)

$$\mathbf{x} = \begin{bmatrix} h_{LV} \\ h_{AO} \\ p_{LV} \\ p_{AO} \\ Q_p \end{bmatrix}, \mathbf{u} = \begin{bmatrix} \dot{m}_{LV} \\ \dot{m}_{AO} \\ 1/R_{hv} \end{bmatrix}, \mathbf{y} = \begin{bmatrix} p_{LV} \\ p_{AO} \\ h_{AO} \end{bmatrix}, \tag{2.32}$$

and the corresponding vector fields $\mathbf{f}(\mathbf{x})$, $\mathbf{g}(\mathbf{x})$, and $\mathbf{h}(\mathbf{x})$

$$\mathbf{f}(\mathbf{x}) = \begin{bmatrix} \frac{-x_5}{A} \\ \frac{x_5}{A} \\ \frac{-x_3\,x_5}{V-A\,x_1} \\ \frac{x_4\,x_5}{V-A\,x_2} \\ \frac{a\,n^2-R_1\,n\,x_5-R_2\,{x_5}^2-H(\mathbf{x})}{L} \end{bmatrix}, \tag{2.33a}$$

$$\mathbf{g}(\mathbf{x}) = \begin{bmatrix} 0 & 0 & \frac{H(\mathbf{x})}{A} \\ 0 & 0 & -\frac{H(\mathbf{x})}{A} \\ \frac{RT}{V-A\,x_1} & 0 & \frac{x_3\,H(\mathbf{x})}{V-A\,x_1} \\ 0 & \frac{RT}{V-A\,x_2} & \frac{-x_4\,H(\mathbf{x})}{V-A\,x_2} \\ 0 & 0 & 0 \end{bmatrix}, \tag{2.33b}$$

$$\mathbf{h}(\mathbf{x}) = \begin{bmatrix} x_3 \\ x_4 \\ x_2 \end{bmatrix}, \tag{2.33c}$$

where $H(\mathbf{x}) = (x_4 - x_3 + \rho\,g\,x_2 - \rho\,g\,x_1)$ is the head pressure and $x_5 > q_{inf}$ is assumed. By applying (2.27) to all outputs, the input-output relation of the atraumatic design is obtained

$$\begin{bmatrix} \dot{y}_1 \\ \dot{y}_2 \\ \dot{y}_3 \end{bmatrix} = \underbrace{\begin{bmatrix} \frac{-x_3\,x_5}{V-A\,x_1} \\ \frac{x_4\,x_5}{V-A\,x_2} \\ \frac{x_5}{A} \end{bmatrix}}_{\mathbf{l}(\mathbf{x})} + \underbrace{\begin{bmatrix} \frac{RT}{V-A\,x_1} & 0 & \frac{x_3\,H(\mathbf{x})}{V-A\,x_1} \\ 0 & \frac{RT}{V-A\,x_2} & -\frac{x_4\,H(\mathbf{x})}{V-A\,x_2} \\ 0 & 0 & -\frac{H(\mathbf{x})}{A} \end{bmatrix}}_{\mathbf{J}(\mathbf{x})} \begin{bmatrix} u_1 \\ u_2 \\ u_3 \end{bmatrix}. \tag{2.34}$$

The resulting relative degree of the k-th output of both multivariate systems (2.31), (2.34) yields

$$\delta_1 = 1, \quad \delta_2 = 1, \quad \delta_3 = 1\,. \tag{2.35}$$

The *vector relative degree* of a system is defined as

$$\delta = (\delta_1, \ldots, \delta_m)\,. \tag{2.36}$$

A multivariate system has *full vector relative degree* if

$$\Delta = \sum_{k=1}^{m} \delta_k = n \tag{2.37}$$

holds. Here the vector relative degree amounts to $\Delta = 3 < n = 5$ for both designs, which results in *non full vector relative degree*. Such system is not fully linearizable and has to be split into external and internal dynamics. The internal dynamics are not observable from the system output. However, the stability of the internal dynamics must be considered, as it affects the stability of the overall system [26, 28]. The stability of the internal dynamics is discussed in section 2.3.4.

Dynamic Extension Algorithm is a method that aims to raise the relative degree of a system with initial *non full vector relative degree* $\Delta < n$ by introducing a feedback structure that incorporates an additional set of dynamic state variables. This algorithm allows to raise the vector relative degree to the system order $\Delta = n$. [26]
The method is illustrated by applying it to the multivariate systems. In this context the relative degree of the third output y_3 should be increased twofold within both designs. The algorithm is applied to the third output to avoid additional dynamics in the first two outputs and therefore in the pressure dynamics of the system.
To increase the relative degree by one, the corresponding time derivative ${y_3}^{(\delta_3+1)}$ is expressed by introducing an additional state variable as $\xi_{3,1}$ [26]. To express ${y_3}^{(\delta_3+2)}$ this method is repeated by introducing a second new state variable $\xi_{3,2}$, which yields

$${y_3}^{(\delta_3)} = \xi_{3,1}, \tag{2.38a}$$
$${y_3}^{(\delta_3+1)} = \dot{\xi}_{3,1} = \xi_{3,2}, \tag{2.38b}$$
$${y_3}^{(\delta_3+2)} = \dot{\xi}_{3,2}\,. \tag{2.38c}$$

Hence the relative degree $(\delta_3 + 2) = 3$ is increased twofold, the multivariate system has *full vector relative degree* $\Delta = 5$ and can be linearized with the aid of an input and state transformation.

Within an *input transformation*, a synthetic input vector $\mathbf{v} = (v_1, \ldots, v_m)$ is chosen according to

$$v_k = y_k^{(\delta_k)}. \tag{2.39}$$

Given the multivariate system with raised relative degree (2.38) one obtains for both designs

$$\mathbf{v} = \begin{bmatrix} v_1 \\ v_2 \\ v_3 \end{bmatrix} = \begin{bmatrix} \dot{y}_1 \\ \dot{y}_2 \\ \dddot{y}_3 \end{bmatrix}. \tag{2.40}$$

By rearranging the input-output relation (2.28) with the new state variables and the synthetic input, a decoupling control law for the input $\mathbf{u}$ is obtained that incorporates the inherent nonlinearities of the system

$$\mathbf{u} = \mathbf{J}^{-1}(\mathbf{x}) \left(\begin{bmatrix} v_1 \\ v_2 \\ \xi_{3,1} \end{bmatrix} - \mathbf{l}(\mathbf{x}) \right), \tag{2.41}$$

where the coupling matrix $\mathbf{J}(\mathbf{x})$ is assumed to be regular. This nonlinear control law applies to both designs, and can be specified by inserting the matrices from (2.31) for the state-of-the-art design and the matrices from (2.34) for the atraumatic design, respectively.

Within a *state transformation* a new state vector $\mathbf{z}$ is chosen according to

$$\mathbf{z} = \mathbf{t}(\mathbf{x}) = \begin{bmatrix} z_1 \\ \vdots \\ z_{\delta_1} \\ z_{\delta_1+1} \\ \vdots \\ z_n = z_{\delta_m} \end{bmatrix} = \begin{bmatrix} y_1 \\ \vdots \\ y_1^{\delta_1-1} \\ y_1^{\delta_1} \\ \vdots \\ y_m^{\delta_m-1} \end{bmatrix} = \begin{bmatrix} h_1(\mathbf{x}) \\ \vdots \\ L_{\mathbf{f}}^{\delta_1-1} h_1(\mathbf{x}) \\ \xi_1 \\ \vdots \\ L_{\mathbf{f}}^{\delta_m-1} h_m(\mathbf{x}) \end{bmatrix}. \tag{2.42}$$

Given the multivariate systems one obtains

$$\mathbf{z} = \mathbf{t}(\mathbf{x}) = \begin{bmatrix} z_1 \\ z_2 \\ z_3 \\ z_4 \\ z_5 \end{bmatrix} = \begin{bmatrix} y_1 \\ y_2 \\ y_3 \\ \dot{y}_3 \\ \ddot{y}_3 \end{bmatrix} = \begin{bmatrix} h_1(\mathbf{x}) \\ h_2(\mathbf{x}) \\ h_3(\mathbf{x}) \\ \xi_{3,1} \\ \xi_{3,2} \end{bmatrix} \tag{2.43}$$

for both designs. Combining the state (2.43) and the input transformation (2.40) a linear and fully decoupled state space representation is obtained

$$\dot{\mathbf{z}} = \begin{bmatrix} \mathbf{A}_{11} & 0 & \cdots & 0 \\ 0 & \mathbf{A}_{22} & \cdots & 0 \\ \vdots & \vdots & \ddots & \vdots \\ 0 & 0 & \cdots & \mathbf{A}_{mm} \end{bmatrix} \mathbf{z} + \begin{bmatrix} \mathbf{b}_{11} & 0 & \cdots & 0 \\ 0 & \mathbf{b}_{22} & \cdots & 0 \\ \vdots & \vdots & \ddots & \vdots \\ 0 & 0 & \cdots & \mathbf{b}_{mm} \end{bmatrix} \mathbf{v}. \tag{2.44}$$

Equally for both multivariate systems this results in

$$\dot{\mathbf{z}} = \begin{bmatrix} 0 & 0 & 0 & 0 & 0 \\ 0 & 0 & 0 & 0 & 0 \\ 0 & 0 & 0 & 1 & 0 \\ 0 & 0 & 0 & 0 & 1 \\ 0 & 0 & 0 & 0 & 0 \end{bmatrix} \begin{bmatrix} h_1(\mathbf{x}) \\ h_2(\mathbf{x}) \\ h_3(\mathbf{x}) \\ \xi_{3,1} \\ \xi_{3,2} \end{bmatrix} + \begin{bmatrix} 1 & 0 & 0 \\ 0 & 1 & 0 \\ 0 & 0 & 0 \\ 0 & 0 & 0 \\ 0 & 0 & 1 \end{bmatrix} \begin{bmatrix} v_1 \\ v_2 \\ v_3 \end{bmatrix}, \tag{2.45}$$

which describes $m = 3$ decoupled linear SISO systems composed of δ_k integrators (cf. Fig. 2.13). Of note, each of the outputs y_k is only affected by one synthetic input v_j. As a result arbitrary linear methods can be used for controller design.

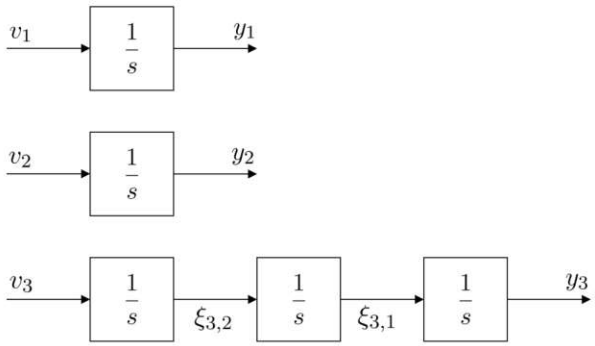

Figure 2.13: Decoupled linear systems comprising δ_k integrators.

2.3.3 Feedback control

Considering (2.28) it becomes clear that the structure of the coupling matrix $\mathbf{J}(\mathbf{x})$ determines if the system is controllable: The multivariate system is controllable as long as the coupling matrix is regular and therefore has full rank. Under the assumption of a controllable multivariate system, a linearizing and decoupling control law (2.41) can be derived by the methods described above.

State-of-the-art design.
The coupling matrix of the state-of-the-art design stated in (2.31) is regular as long as

$$J_{33} = -\frac{p_{10} - H(\mathbf{x})\, p_{11}}{A} \neq 0. \tag{2.46}$$

Of note, in case of $J_{33} = 0$, the numerator expresses the critical pressure difference between the reservoirs of the H-MCL, which can not be overcome by the gear pump. Consequently no flow is generated, which results in a loss of controllability. Here the critical pressure difference results in

$$H(\mathbf{x}) = \frac{p10}{p11} = 3833\,\text{mmHg}\,(= 5.111 \cdot 10^5\,\text{Pa}), \tag{2.47}$$

which is significantly higher than the available supply pressure of the system. Consequently the state-of-the-art design is fully controllable and can be decoupled according to (2.41). Considering the linear system (2.45), linear methods such as full state feedback (FSF) can be used for controller design. FSF describes a method in feedback control, which places the closed-loop poles of a system at a desired location. As the poles correspond to the eigenvalues of a linear system, FSF determines the system response.

The closed loop behavior of a linear system is described as

$$Y_i(s) = \frac{a_{i,0}}{s^{\delta_i} + a_{i,\delta_i-1}s^{\delta_i-1} + \ldots + a_{i,1}s + a_{i,0}} W_i(s), \tag{2.48}$$

which leads to a differential equation of the form

$$y_i^{(\delta_i)} + a_{i,\delta_i-1}y_i^{\delta_i-1} + \ldots + a_{i,1}y_i + a_{i,0} = a_{i,0}w_i \tag{2.49}$$

for the desired linear reference behavior. The coefficients $a_{i,j}$ are determined by the desired characteristic polynomial of the closed loop for y_i. Applying this to (2.45) three differential equations are obtained

$$\dot{y}_1 + a_{1,0}y_1 = a_{1,0}w_1, \tag{2.50a}$$
$$\dot{y}_2 + a_{2,0}y_2 = a_{2,0}w_2, \tag{2.50b}$$
$$\dddot{y}_3 + a_{3,2}\ddot{y}_3 + a_{3,1}\dot{y}_3 + a_{3,0}y_3 = a_{3,0}w_3, \tag{2.50c}$$

which results in a control law for the synthetic input vector $\mathbf{v}$

$$\begin{bmatrix} v_1 \\ v_2 \\ v_3 \end{bmatrix} = -\underbrace{\begin{bmatrix} a_{1,0} & 0 & 0 & 0 & 0 \\ 0 & a_{2,0} & 0 & 0 & 0 \\ 0 & 0 & a_{3,0} & a_{3,1} & a_{3,2} \end{bmatrix}}_{\mathbf{K}} \begin{bmatrix} h_1(\mathbf{x}) \\ h_2(\mathbf{x}) \\ h_3(\mathbf{x}) \\ \xi_{3,1} \\ \xi_{3,2} \end{bmatrix} + \underbrace{\begin{bmatrix} a_{1,0} & 0 & 0 \\ 0 & a_{2,0} & 0 \\ 0 & 0 & a_{3,0} \end{bmatrix}}_{\mathbf{K}_w} \begin{bmatrix} w_1 \\ w_2 \\ w_3 \end{bmatrix}, \tag{2.51}$$

where $\mathbf{K}$ is the feedback gain and $\mathbf{K}_w$ is the prefilter gain matrix. The nonlinear control law (2.41) for the state-of-the-art design (2.31) is given by

$$\mathbf{u} = \mathbf{J}^{-1}(\mathbf{x}) \left(\begin{bmatrix} v_1 \\ v_2 \\ \xi_{3,1} \end{bmatrix} - \mathbf{l}(\mathbf{x}) \right), \tag{2.52}$$

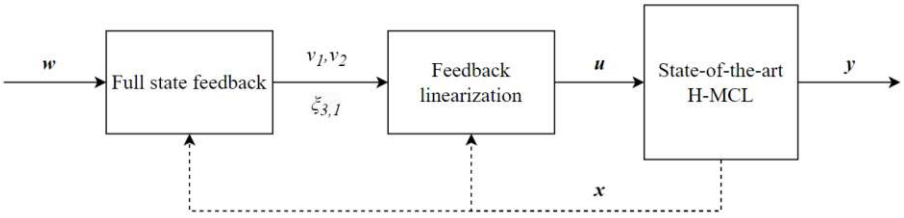

Figure 2.14: Block diagram of the control strategy derived for the state-of-the-art design: based on full state feedback and feedback linearization with dynamic extension.

where the virtual inputs v_1, v_2 can be determined by the dedicated control law (2.51) and the state variable $\xi_{3,1}$ is determined from the second order differential equation for v_3, which has to be solved online.
The final control structure for the state-of-the-art design is depicted in Fig. 2.14 as block diagram.

Atraumatic design.
The coupling matrix of the atraumatic design stated in (2.34) is regular as long as

$$J_{33} = -\frac{H(\mathbf{x})}{A} \neq 0, \tag{2.53}$$

Here the numerator expresses the pressure difference between the reservoirs of the H-MCL. In the case of $\mathbf{J}_{33} = 0$, the critical pressure difference becomes

$$H(\mathbf{x}) = 0, \tag{2.54}$$

then there is no driving force to generate a flow through the pinch valve and consequently the pinch valve has no effect on the system, which results in a loss of controllability. With realistic hemodynamic pressures as with the partial support condition (cf. Fig. 2.4) a periodic loss of controllability must be considered as left ventricular and aortic pressures are approximately equal during systole of the cardiac cycle.
As the multivariate system is associated with a periodical loss of controllability, a control structure has to be chosen that drives the system along a defined trajectory during both controllable and uncontrollable periods of the cardiac cycle. To do so the system is split in a controllable and periodically uncontrollable subsystem, where different feedback control strategies are applied.

Controllable subsystem. The nonlinear control law from (2.41) can be reduced to the first two inputs

$$\begin{bmatrix} u_1 \\ u_2 \end{bmatrix} = \underbrace{\begin{bmatrix} J_{11}(\mathbf{x}) & J_{12}(\mathbf{x}) \\ J_{21}(\mathbf{x}) & J_{22}(\mathbf{x}) \end{bmatrix}^{-1}}_{\mathbf{J}^*} \left(\begin{bmatrix} v_1 \\ v_2 \end{bmatrix} - \begin{bmatrix} l_1(\mathbf{x}) \\ l_2(\mathbf{x}) \end{bmatrix} - \begin{bmatrix} J_{13}(\mathbf{x}) \\ J_{23}(\mathbf{x}) \end{bmatrix} u_3 \right), \tag{2.55}$$

where J_{mn} are the entries of the decoupling matrix from (2.34). This results in a fully controllable subsystem, as $\mathbf{J}^*$ is regular and thus invertible.
To control this subsystem, FSF is applied and a desired linear reference behavior is chosen for each output according to (2.49), which results in

$$\dot{y}_1 + a_{1,0} y_1 = a_{1,0} w_1, \tag{2.56a}$$
$$\dot{y}_2 + a_{2,0} y_1 = a_{2,0} w_2, \tag{2.56b}$$

where $a_{i,\delta}$ are the coefficients of the desired closed loop characteristic polynomial and $w_{1,2}$ are the left ventricular and aortic pressures from the cardiovascular model to be emulated. This results in a linear control law for the synthetic input

$$\begin{bmatrix} v_1 \\ v_2 \end{bmatrix} = -\underbrace{\begin{bmatrix} a_{1,0} & 0 \\ 0 & a_{2,0} \end{bmatrix}}_{\mathbf{K}} \begin{bmatrix} h_1(\mathbf{x}) \\ h_2(\mathbf{x}) \end{bmatrix} + \underbrace{\begin{bmatrix} a_{1,0} & 0 \\ 0 & a_{2,0} \end{bmatrix}}_{\mathbf{K}_w} \begin{bmatrix} w_1 \\ w_2 \end{bmatrix}, \tag{2.57}$$

with the feedback gain $\mathbf{K}$ and the prefilter gain $\mathbf{K}_w$ matrix. By inserting (2.57) in (2.55) the nonlinear control law for the controllable subsystem, which decouples the pressures in both reservoirs, is obtained.
Of note, the current pinch valve flow $Q_{hv} = H(\mathbf{x})u_3$ is measured and considered within the nonlinear control law (2.55), which can be expressed as

$$\begin{bmatrix} u_1 \\ u_2 \end{bmatrix} = \begin{bmatrix} J_{11}(\mathbf{x}) & J_{12}(\mathbf{x}) \\ J_{21}(\mathbf{x}) & J_{22}(\mathbf{x}) \end{bmatrix}^{-1} \left(\begin{bmatrix} v_1 \\ v_2 \end{bmatrix} - \begin{bmatrix} l_1(\mathbf{x}) \\ l_2(\mathbf{x}) \end{bmatrix} - \begin{bmatrix} \frac{x_3}{V - A\,x_1} \\ -\frac{x_4}{V - A\,x_2} \end{bmatrix} Q_{hv} \right). \tag{2.58}$$

Periodically uncontrollable subsystem. Due to the periodic loss of controllability of the third output y_3, linear reference behavior of the subsystem in analogy to (2.56) can not be implemented. Here, a control approach has to be chosen that determines a control trajectory for u_3, which accounts for both controllable and uncontrollable periods of y_3 within each cardiac cycle. Two control objectives have to be ensured: First, the level fluctuation of y_3 is not allowed to exceed a defined range. Second, atraumatic pinch valve characteristics have to be ensured which is characterized by minimal pinch valve movement x_{hv}. To achieve both control objectives, an optimization problem is formulated where a cost function J is minimized over the period of one cardiac cycle (i.e. $t_s \leq \tau \leq t_e$)

$$
\begin{aligned}
J\left[x_{hv}(\tau)\right] = & \int_{\tau=t_s}^{t_e} \alpha \dot{x}_{hv}^2 + (h_{dmd} - y_3)^2 d\tau \\
\text{s.t.} \quad & 0.025\text{m} \leq y_3 \leq 0.045\text{m} \\
& 600 \leq x_{hv} \leq 1200 \\
& \dddot{y}_3 = \ddot{\xi}_{3,1} = \dot{\xi}_{3,2} = v_3.
\end{aligned} \tag{2.59}
$$

Here, α is a weighting factor that penalizes the valve motion x_{hv}, and $h_{dmd} = 0.035$ m is the constant target height which corresponds to the optimal fluid distribution during operation. The dynamics of the reservoir level y_3 can be expressed in terms of the control input u_3 as

$$
\begin{aligned}
\dot{y}_3 &= l_3(\mathbf{x}) + J_{33}(\mathbf{x}) u_3 \\
&= \frac{x_5}{A} - \frac{H(\mathbf{x})}{A} u_3.
\end{aligned} \tag{2.60}
$$

The system dynamics show the connection between the reservoir level y_3, the pump flow rate x_5 as well as the pinch valve flow rate $H(x)u_3 = \tilde{u}_3$. The level is a function of the pressure difference $H(\mathbf{x}) = x_4 - x_3 + \rho g x_2 - \rho g x_1$ between the reservoirs, which is described by the current hemodynamic pressures and the hydrostatic pressures of the fluid columns. Within the low volume design the hydrostatic pressure can be neglected as $x_4 - x_3 >> \rho g x_2 - \rho g x_1$ is assumed. Further the level is dependent on the valve resistance $u_3 = 1/R_{hv}(x_{hv})$, which is determined from (2.41)

$$
u_3 = J_{33}(\mathbf{x})^{-1} \left(\xi_{3,1} - l_3(\mathbf{x})\right). \tag{2.61}
$$

Considering a decoupled pressure control (2.58), the hemodynamic characteristics determine if a stable level control can be achieved and a trajectory for $\xi_{3,1}$ in compliance with the boundary conditions is obtained from (2.59): Exemplary, the reference pressures of the partial support condition are considered in combination with a large α, which penalizes the valve motion. Here, the optimization problem provides a control trajectory for $\xi_{3,1}$, that results in marginal valve motion within each cardiac cycle, without violating the boundary conditions of the fluid level.

The result of the optimization problem with the partial support condition is shown in Fig. 2.15. This depicts that the valve resistance u_3 is approximately constant except for the uncontrollable period of the cardiac cycle (highlighted in grey). The resulting peak can be traced back to numerical effects, when the pressure difference H approaches zero. With such constant resistance (constant valve slide x_{hv}), the uncontrollable timespan shows an increasing aortic level y_3, due to a increasing pump flow rate and a declining pinch valve flow rate. This level deviation is compensated by an increased flow rate through the pinch valve within the controllable timespan of the cardiac cycle. As a result the aortic level decreases leading to a stable fluctuation around the target level height. This describes a solution for the control of the fluid level, which accounts for both requirements stated above, a stable level control

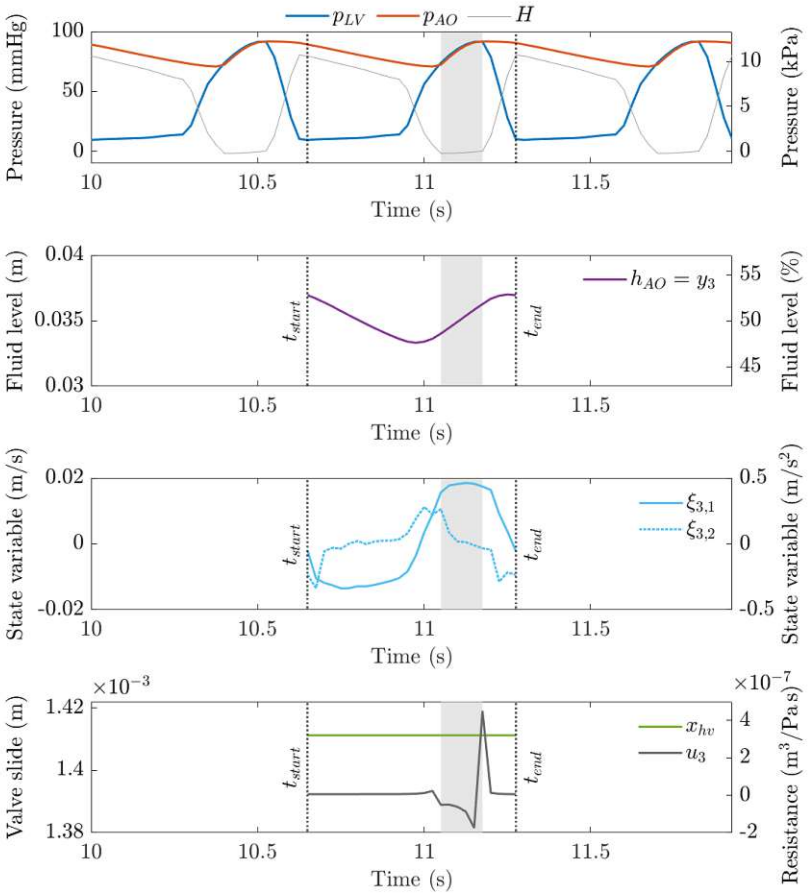

Figure 2.15: Optimization results for one cardiac cycle (partial support condition). The four panels depict the time course of (a) the hemodynamic pressures of the left ventricle and aorta, and the head pressure (b) the fluid level in the aortic reservoir, (c) the optimized control trajectory of the additional state variables, and (d) the resulting valve resistance and pinch valve slide. The grey area marks the uncontrollable timespan during systole.

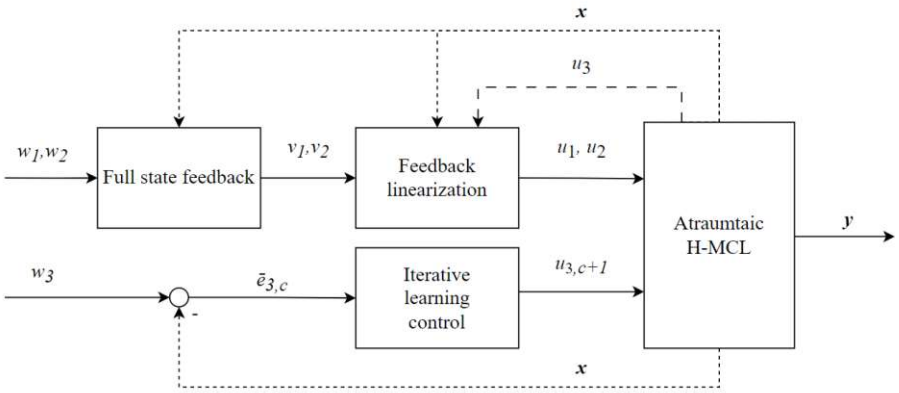

Figure 2.16: Block diagram of the control strategy: iterative learning control in combination with full state feedback and feedback linearization. The iterative learning control considers data of the last cardiac cycle to overcome periods of no controllability, while the nonlinear decoupling control law ensures precise trajectory tracking.

despite periodic loss of controllability combined with atraumtic pinch valve characteristics. These findings are equally valid for the full support condition with lower pulsatility in the left ventricular pressure, which leads to a different optimal pinch valve resistance (and a corresponding valve slide x_{hv}).

As, the optimization problem can not be solved in real-time and the underlying model is not perfect, a control structure in the style of an iterative learning control (ILC) is implemented to compensate for model errors and disturbances within each cardiac cycle. The ILC control law is based on the findings of the optimization and can be formulated as

$$u_{3,c+1} = u_{3,c}^{est} + \Delta\overline{u}_{3,c+1}\,, \tag{2.62}$$

where $u_{3,c}^{est}$ is an estimated input based on the preceding c-th cardiac cycle, while $\Delta\overline{u}_{3,c+1}$ is an offset based on the mean level error according to

$$\Delta\overline{u}_{3,c+1} = \Delta\overline{u}_{3,c} + K(h_{dmd} - \overline{y}_{3,c})\,, \tag{2.63}$$

where $\Delta\overline{u}_{3,c}$ is the offset of the previous c-th cardiac cycle, which is corrected by a constant design parameter K and the mean level tracking error $\overline{e}_{3,c} = (h_{dmd} - \overline{y}_{3,c})$ of the preceding c-th cycle, which consists of the constant target value h_{dmd} and the mean aortic level $\overline{y}_{3,c}$.

Note, the main idea of this control strategy is to control the mean values resulting from the last cardiac cycle: This allows to calculate the average of each state within the last heart cycle, which is desirable as the mean pressure difference between the reservoirs of one cardiac cycle

is non-zero (considering realistic hemodynamic conditions - the mean aortic pressure is larger than the mean left ventricular pressure). With the non-zero mean pressure difference between the reservoirs a mean valve resistance u_3 can be calculated, which allows to control the mean level of the system. This is sufficient as the target level height is constant. Considering the ILC strategy, a running mean comprising the last cardiac cycle is calculated, which provides the data for the control of the mean level height. Therefore the ILC control law (2.62) is a special presentation of a two-degrees-of-freedom PI-control

$$u_{3,c} = u_{3,c}^{est} + K_P \left(h_{dmd} - \overline{y}_{3,c}\right) + K_I \int \left(h_{dmd} - \overline{y}_{3,c}\right) dt, \tag{2.64}$$

where the $\overline{y}_{3,c}$ describes the mean level height of the last cardiac cycle.

The final control design is depicted in Fig. 2.16 as block diagram. Combining the decoupling control law from feedback linearization with the ILC, both a decoupled control of the left ventricular and aortic pressures within the system as well as atraumatic pinch valve movement is achieved, despite a periodic loss of controllability within each cardiac cycle.
The optimization task was modelled in MATLAB with the aid of YALMIP [29] a toolbox for modelling and optimization and the nonlinear solver *fmincon*, which is part of Mathworks Optimization Toolbox.

2.3.4 Stability consideration

Initially both H-MCL designs resulted in systems with *non full vector relative degree*, that are characterized by external (observable) and internal dynamics. The internal dynamics are not observable from the system output. However, the stability of the internal dynamics must be considered, as it affects the stability of the overall system [26, 28].

State-of-the-art design.
The external and internal dynamics of the system can be assessed by inserting the decoupling nonlinear control law (2.52) into the state differential equations of the multivariate system (2.20) considering (2.29), which leads to

$$\dot{\mathbf{x}} = \begin{bmatrix} -\xi_{3,1} \\ \xi_{3,1} \\ v_1 \\ v_2 \\ \dot{Q}_p \end{bmatrix}, \tag{2.65}$$

where v_1, v_2 and $\xi_{3,1}$ are determined from the desired closed loop polynomials (2.50)

$$v_1 = a_{1,0} w_1 - a_{1,0} x_3, \tag{2.66a}$$
$$v_2 = a_{2,0} w_2 - a_{2,0} x_4, \tag{2.66b}$$
$$\underbrace{\ddot{\xi}_{3,1}}_{\dot{\xi}_{3,2}} = a_{3,0} w_3 - a_{3,2} \underbrace{\dot{\xi}_{3,1}}_{\xi_{3,2}} - a_{3,1} \xi_{3,1} - a_{3,0} x_2. \tag{2.66c}$$

This results in the following state differential equations for the closed loop dynamics

$$\dot{x}_1 = -\xi_{3,1}, \tag{2.67a}$$
$$\dot{x}_2 = \xi_{3,1}, \tag{2.67b}$$
$$\dot{x}_3 = a_{1,0} w_1 - a_{1,0} x_3, \tag{2.67c}$$
$$\dot{x}_4 = a_{2,0} w_2 - a_{2,0} x_4, \tag{2.67d}$$
$$\dot{x}_5 = \frac{1}{L_p} \Bigg(a\, n^2 - R_1\, n\, x_5 - R_2\, {x_5}^2 - (x_4 - x_3 + \rho g x_2 - \rho g x_1) + \begin{cases} 0 & Q_p > q_{inf} \\ R_{rec}(Q_p - q_{inf})^2 & Q_p < q_{inf} \end{cases} \Bigg), \tag{2.67e}$$
$$\dot{\xi}_{3,1} = \xi_{3,2}, \tag{2.67f}$$
$$\dot{\xi}_{3,2} = a_{3,0} w_3 - a_{3,2} \dot{\xi}_{3,1} - a_{3,1} \xi_{3,1} - a_{3,0} x_2, \tag{2.67g}$$

from this one can conclude that the dynamics of the reservoir pressures x_3 and x_4 are decoupled and stable following the closed loop behavior chosen in (2.50). The fluid levels x_1 and x_2 form a linear dynamic subsystem with the new state variables ξ that follows the desired characteristic polynomial from (2.50c). The last state x_5 describes the RBP flow rate, which can not be observed from the system output, therefore forming the internal dynamics of the system.
The stability of the internal dynamics are investigated using Lyapunov stability theory [28]. To do so, an equilibrium point of the system is chosen for the external dynamics, expressed as x_{10}, x_{20}, x_{30}, and x_{40}. Then, the equilibrium of the pump flow rate x_{50} is obtained by

$$\dot{x}_5 = 0 = \frac{1}{L_p} \left(a\, n^2 - R_1\, n\, x_{50} - R_2\, {x_{50}}^2 - H_0 \right), \tag{2.68}$$

where $(x_{50} > q_{inf})$ is assumed and $H_0 = (x_{40} - x_{30} + \rho g x_{20} - \rho g x_{10})$ is the head pressure which is resulting from the external dynamics in the equilibrium point.
By defining a Lyapunov function candidate as

$$V(x_5) = \frac{1}{2} (x_5 - x_{50})^2, \tag{2.69}$$

a sufficient criterion for stability is given, if $\dot{V}(x_5) < 0$ holds along all trajectories of x_5. From this one obtains

$$\dot{V}(x_5) = (x_5 - x_{50})\,(\frac{1}{L_p}\,(a\,n^2 - R_1\,n\,x_5 - R_2\,x_5^2 - H_0)), \tag{2.70}$$

where two cases have to be distinguished:

- *CASE 1* $x_5 > x_{50}$:
  Then $(x_5 - x_{50}) > 0$ and $(a\,n^2 - R_1\,n\,x_5 - R_2\,x_5^2 - H_0) < 0$ holds, and therefore $\dot{V}(x_5) < 0$.

- *CASE 2* $x_5 < x_{50}$:
  Then $(x_5 - x_{50}) < 0$ and $(a\,n^2 - R_1\,n\,x_5 - R_2\,x_5^2 - H_0) > 0$ holds, and therefore $\dot{V}(x_5) < 0$.

This can be analogously shown for $(x_{50} < q_{inf})$ with the Lyapunov function

$$\dot{V}(x_5) = (x_5 - x_{50})\,(\frac{1}{L_p}\,(a\,n^2 - R_1\,n\,x_5 - R_2\,x_5^2 - H_0) + R_{rec}(x_5 - q_{inf})^2). \tag{2.71}$$

Consequently, the internal dynamics of the state-of-the-art design are stable.

Atraumatic design.
Lyapunov stability theory cannot be applied for the atraumatic design as a periodic loss of controllability is observed during systole. With this design, stability can be assessed by the optimization task formulated in (2.59), which shows that a stable operation of the system is possible with marginal actuator effort of the pinch valve. Characteristic reference curves that deviate from the proposed partial and full support condition can be checked for stability using this optimization task.

2.4 Simulative and experimental verification

To evaluate the performance of the novel H-MCL designs, first controller bandwidth and decoupling properties were assessed within simulative investigations. For comparison, a SISO control structure was demonstrated and as examined within a RGA analysis in section 2.3.1 and as proposed in conventional H-MCLs [19]. Second, the reference tracking and disturbance rejection properties of the system were examined within realistic hemodynamic experiments.

2.4.1 Simulative assessment

The models described in section 2.2 allowed to derive a complete simulation model of the novel H-MCLs. This enabled preliminary studies previous to its experimental verification.

The decoupling properties of the control structures was first assessed within a simulation of consecutive step responses. This was exemplary shown for the state-of-the-art design, where consecutive steps were applied to a constant reference value of each output. This allowed to investigate the decoupling properties of the derived nonlinear control law as described in section 2.3.
Within an assessment of different hemodynamic reference curves (partial and full support condition, cf. section 2.2.1, 91 bpm) a set of closed loop poles was identified, which meet the actuator limits while ensuring high performance (exemplary shown for the atraumatic design). Furthermore, the derived controller transfer functions and the corresponding controller bandwidth was described.

2.4.2 Experimental assessment

To assess the performance of the novel decoupling control strategies different hemodynamic reference conditions were investigated, which comprise the partial and full support condition as described in section 2.2.1, considering three different heart rates (60 bpm, 91 bpm, and 120 bpm). The hemodynamic assessment of the novel H-MCLs was conducted with a water-glycerol mixture, which was adapted to the viscosity of blood (3.5 cP) at 23°C.

The quality of reference tracking of the hemodynamic pressures was quantified by the characteristic reference tracking error $e^* = y_{ref} - y$ and the corresponding root mean square error (RMSE), which considers the present reference behavior based on the underlying control transfer function (cf. section 3.1.3). In addition the absolute reference tracking error $e = w - y$ and the corresponding RMSE are provided, which directly considers the reference pressures calculated by the cardiovascular model.

Upfront results from a dismissed SISO control structure [1, 19] without decoupling properties were provided for comparison. These were received from experiments with identical hemodynamic reference conditions (partial and full support) at a heart rate of 91 bpm.

To evaluate the control performance of the novel decoupling control strategies, a step from partial support to full support condition was examined (91 bpm). Although this is no realistic clinical case, it represented a challenging control task and a highly dynamic example, where multiple parameter adaptions were made at the same time: Adapted parameters are the pump speed, which was set to 4450 rpm in partial support condition, while increasing to 5450 rpm in full support condition. The peak pressure changes from 92.5 mmHg to 40 mmHg, which is a parameter of the nonlinear ESPVR of the left ventricle affecting the contractility of the left heart. In consequence pressure pulsatility and pump flow are affected concurrently. This leads to a steep transient in the average flow rate of the blood pump and therefore of the entire H-MCL. The results are presented within an excerpt of 15 s of the experiment, where the stepwise change is shown at $t = 5s$.

Further, a detailed assessment of the trajectory tracking properties of the novel decoupling control strategies is shown for stable operating conditions. Accordingly, a timespan of 1.5 s is depicted for each hemodynamic condition (partial and full support condition, 91 bpm), which shows the reference tracking of the hemodynamic pressures and the fluid height together with the corresponding reference tracking errors. This allows a comparison to the results of the previous SISO control structure. Within this scope different dynamics, which are described by a change in the heart rate are investigated for both partial and full support condition, respectively.

Finally, the measured results form partial and full support condition and a heart rate of 91 bpm were contrasted with simulative results with identical reference input to assess the accuracy of the numerical models described in section 2.2.

3 Results

This section provides results from preliminary simulations and experimental tests, which were achieved with the novel control strategy. Additionally, these results are compared to a dismissed SISO control structure.

3.1 Preliminary simulations

This section provides findings from preliminary tests conducted prior to the experimental assessment of the novel H-MCL designs. This includes the investigation of decoupling characteristics, actuator limits and resulting controller transfer functions.

3.1.1 Decoupling characteristics

To assess the decoupling properties of the novel control strategy, reference steps were applied to each input of the system, while the effect on the systems output was observed. This is exemplary shown for the state-of-the-art design, which is decoupled by the nonlinear control law (2.52). Fig. 3.1a shows three consecutive reference steps $\mathbf{w}$ at 2.5 s, 5 s, and 7.5 s with different amplitudes. Further, the resulting control reference behavior $\mathbf{v}$ based on the chosen controller transfer functions (cf. section 3.1.3) is shown and the resulting system output $\mathbf{y}$ is simulated.
It can be seen that the control law reliably decouples the system, despite large reference step amplitudes. This is achieved by a systematic interaction of the input variables $\mathbf{u}$ as shown in Fig. 3.1b, where each step input results in a combined change of all input variables to ensure precise trajectory tracking and decoupling of the output. This can be attributed to the underlying control law which accounts for the inherent nonlinearities of the system and ensures a decoupled system response.

3.1.2 Actuator limitations

An important preliminary test before experimental application was the choice of controller parameters in compliance with the actuator limits of the system. Large steps as simulated in 3.1.1 lead to large peak values in the demanded actuator effort (cf. Fig. 3.1b), which may exceed the physical limits. Considering experimental application, the resulting control reference behavior must be feasible without violating the actuator limits of the system. The physical actuator limits are defined by the chosen components and the supply pressures within

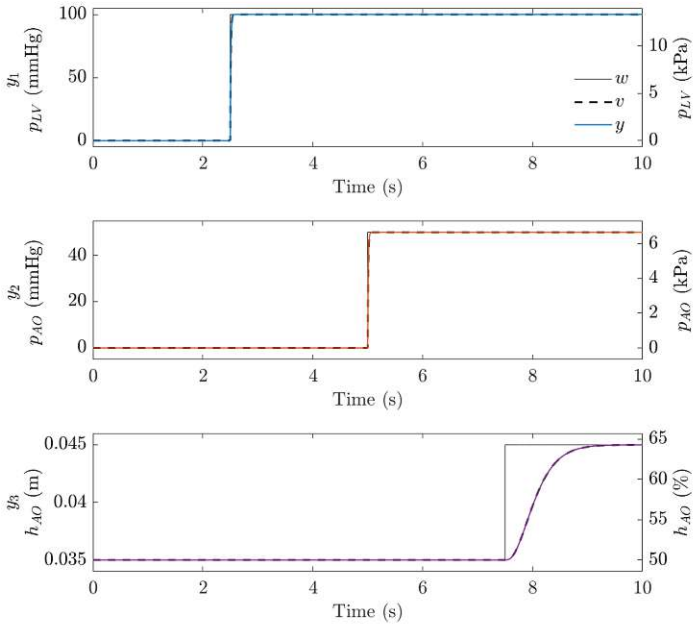

(a) Reference step **w** with characteristic reference behavior **v** and the simulated output **y**. The outputs are completely decoupled.

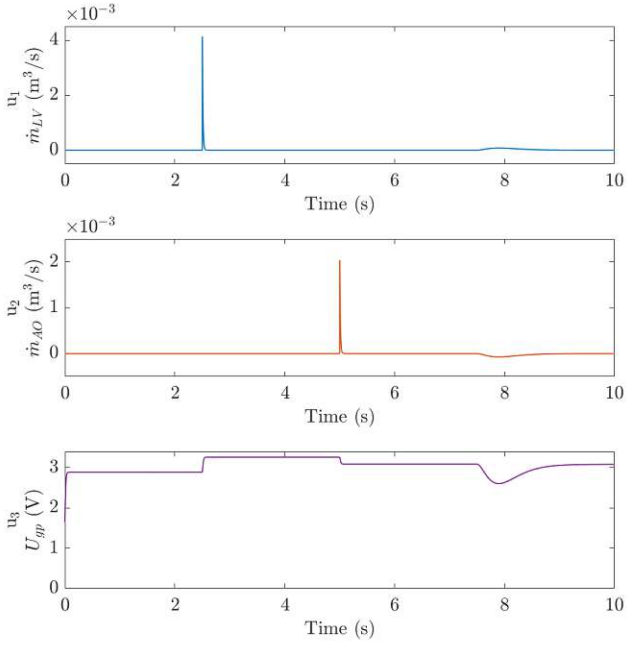

(b) Control input **u** resulting from reference step **w**. All inputs interact to decouple the system.

Figure 3.1: Simulated reference step response of the state-of-the-art design, which indicates that the nonlinear control law fully decouples the system.

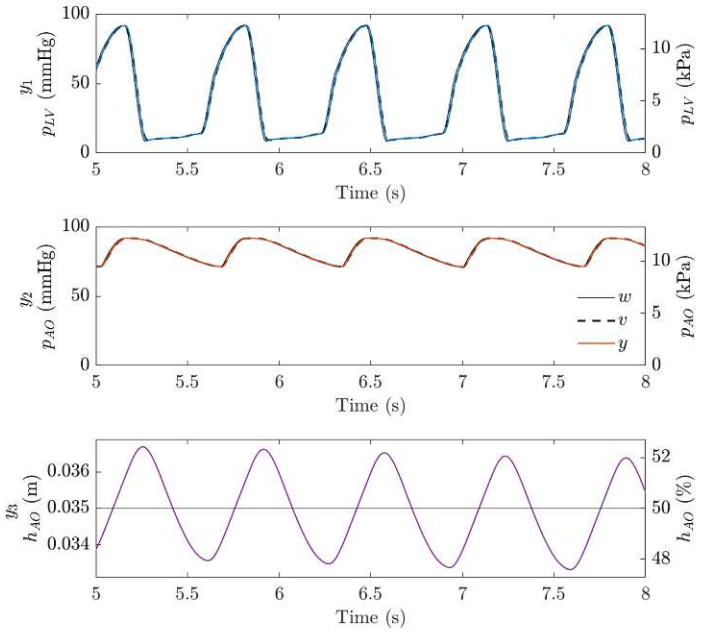

(a) Simulation of the system output of the atraumatic design for the partial support condition.

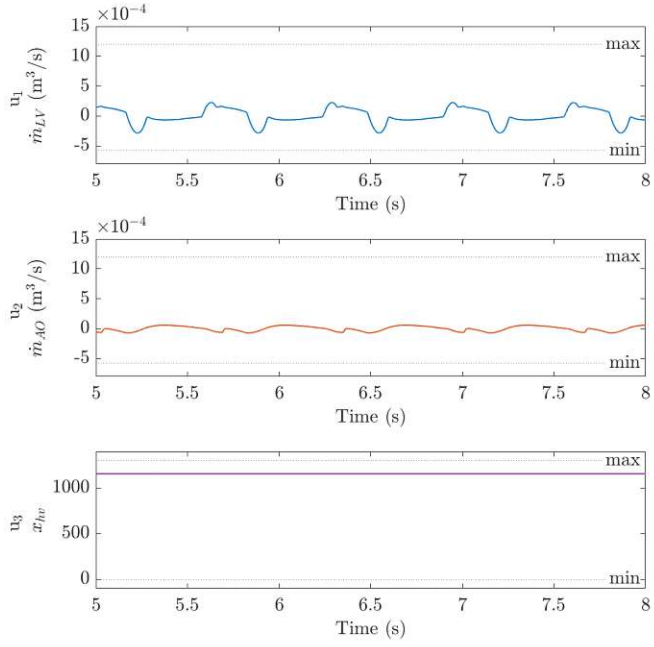

(b) Simulation of the actuator effort of the atraumatic design for the partial support condition

Figure 3.2: Assessment of actuator effort of the atraumatic design within partial support condition and with respect to the chosen controller parameters.

Table 3.1: Actuator limits

Parameters		Clinical		SI	
$\dot{m}$	min	-34.8	L/min	$-5.8{\cdot}10^{-4}$	m^3/s
	max	72.0	L/min	$12.0{\cdot}10^{-4}$	m^3/s
U_{gp}	min			0	V
	max			3.3	V
x_{hv}	min			0	(steps)
	max			1300	(steps)

the system, as stated in Table 3.1 for both state-of-the-art and atraumatic design of the H-MCL.
Considering the chosen control transfer function, which is described in more detail in the next section, the actuator effort and the system output is exemplary simulated for the partial support condition and the atraumatic design as depicted in Fig. 3.2a and 3.2b. It can be seen that the demanded actuator effort safely remains inside the boundaries of systems actuator limits, which indicates a feasible choice of controller parameters for experimental application. This was analogously assessed for the full support condition, as well as for the state-of-the-art design, before taking experimental studies.

3.1.3 Control transfer functions

The final control transfer functions were derived from preliminary simulation in combination with preceding experimental testing, which led to an optimized choice of closed loop poles (clp), representing a stable but fast controller design. The resulting poles are presented in Table 3.2 together with the corresponding coefficients of the controller transfer functions. With the chosen poles, the transfer functions result in

$$G_{c,1} = G_{c,2} = \frac{120}{s + 120}, \tag{3.1a}$$

$$G_{c,3} = \frac{132.6}{s^3 + 15.3s^2 + 78.02s + 132.6}, \tag{3.1b}$$

where $G_{c,1} = G_{c,2}$ are the reference pressure transfer functions and valid for both state-of-the-art and atraumatic design. Of note, $G_{c,3}$ is the transfer function of the level controller of the gear pump within the state-of-the-art design only. The bode plot of these transfer functions is shown in Fig. 3.3a, which shows a bandwidth of 19.05 Hz for $G_{c,1} = G_{c,2}$ and 0.4129 Hz for $G_{c,3}$. Further the step responses are depicted in Fig. 3.3b, which show a rise time of 0.0183 s for the reference pressures and 0.8279 s for the fluid level. The step response characteristics from *stepinfo* [30] indicate zero overshoot and a settling time of 0.0326 s vs. 1.4744 s for the pressure control and the level control, respectively.
The control transfer functions from (3.1a) provide the characteristic reference behavior, which forms the reference input to the nonlinear control law of both state-of-the-art and atraumatic design, respectively.

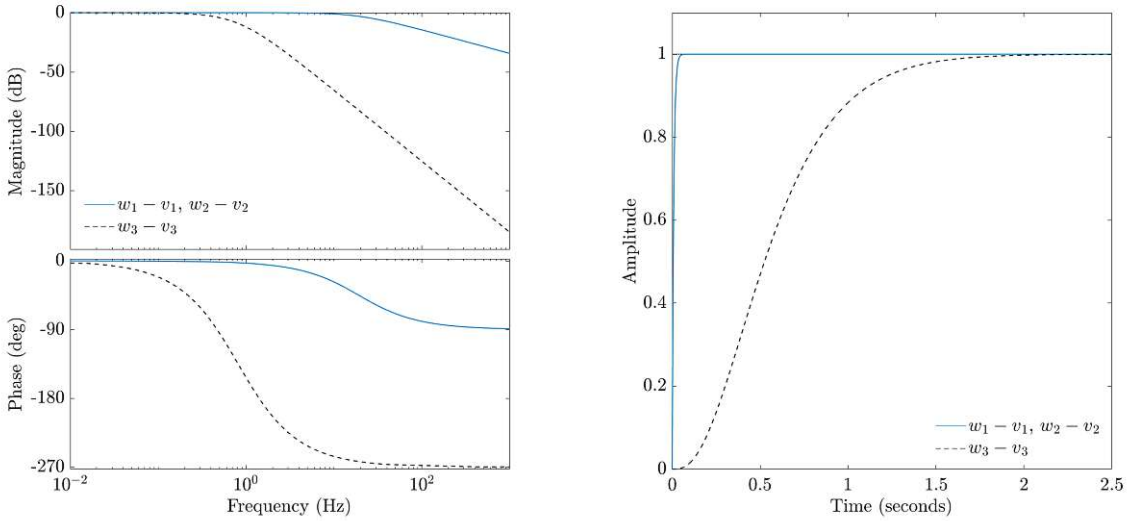

(a) Bode plot.

(b) Step response.

Figure 3.3: Frequency response and time response of the controller transfer functions.

Table 3.2: Closed loop poles and transfer function coefficients

	$G_{c,1}, G_{c,2}$		$G_{c,3}$	
Poles	[clp1]	[-120]	[clp1, clp2, clp3]	[-5, -5.1, -5,2]
Coefficients	$a_{i,0}$	120	$a_{i,2}, a_{i,1}, a_{i,0}$	15.3, 78.02, 132.6

3.2 Experimental outcome

3.2.1 Dismissed SISO control structure

This section provides the results of a conventional SISO control approach as initially implemented for the novel H-MCL designs:
Fig. 3.4a and Fig. 3.4b depict the pressure reference tracking results and the corresponding absolute error for the *state-of-the-art* design, which indicate nonphysiologic deviations and coupling effects within the system, despite a fast PI control ($P = 0.06, I = 1.00$), which is described in more detail in a previous work [1]. This leads to a maximal error of 15.9 mmHg and 6.0 mmHg in the left ventricular and aortic pressure within partial support condition, and a corresponding RMSE of 3.8 mmHg and 2.2 mmHg. Considering the full support condition the error is smaller, arising to a maximal error of 10.4 mmHg and 2.6 mmHg, and a RMSE of 2.8 mmHg and 1.0 mmHg, respectively.
In analogy Fig. 3.5a and Fig. 3.5b show the results for the *atraumatic* design with the SISO control structure. Similarly the maximal error in the left ventricle is larger compared to the aortic pressure, which results in 15.1 mmHg and 9.6 mmHg for the partial support condition, with a RMSE of 4.2 mmHg and 2.9 mmHg, respectively. The errors during full support condition yield 10.6 mmHg and 6.8 mmHg for the left ventricle and the aorta, which results in an RMSE of 2.3 mmHg and 2.1 mmHg, respectively. These errors are summarized in Table 3.3.

Table 3.3: RMSE and maximal error of SISO control approach for the state-of-the-art design (MCL) and the atraumatic design (A-MCL) at partial and full support, respectively

	SISO			**Partial support**		**Full support**	
	(mmHg)			Left ventricle	Aorta	Left ventricle	Aorta
MCL	91 bpm	**e**	RMSE	3.7955	2.1550	2.8061	1.0173
			Error max.	15.9433	5.9737	10.4007	2.6196
A-MCL	91 bpm	**e**	RMSE	4.1462	2.8537	2.3005	2.0674
			Error max.	15.0668	9.6307	10.6074	6.7906

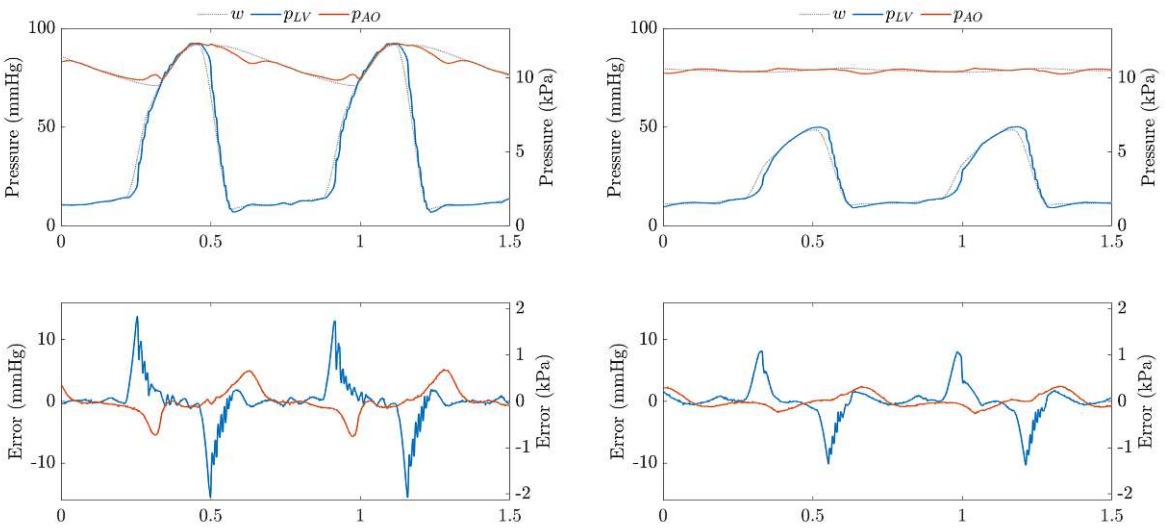

(a) Partial support. (b) Full support.

Figure 3.4: Reference tracking with dismissed SISO control structure and the *state-of-the-art* design.

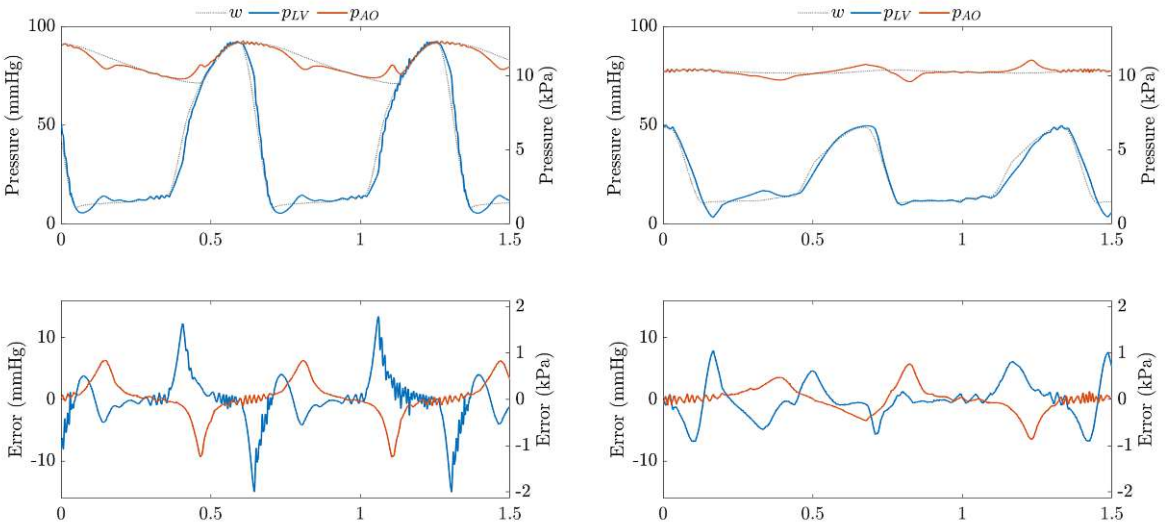

(a) Partial support. (b) Full support.

Figure 3.5: Reference tracking with previous SISO control structure and the *atraumatic* design.

3.2.2 Decoupling MIMO control structure

This section shows the reference tracking results of the novel decoupling MIMO control approach for both design variations.

Fig. 3.6a and Fig. 3.6b depict an excerpt of the characteristic reference tracking of the pressures and the fluid level with the *state-of-the-art* design, together with resulting errors. The absolute pressure error is maximal for the left ventricle with a RMSE of 3.0 mmHg and 1.4 mmHg in partial and full support, respectively. With the depicted characteristic reference behavior (based on the transfer functions of the controllers from section 3.1.3) the RMSE is reducing to 0.9 mmHg and 0.4 mmHg, respectively. The characteristic RMSE of the aortic pressure yields 0.7 mmHg in partial support and 0.3 mmHg in full support condition. Table 3.4 summarizes the pressure errors including both RMSE and maximal errors for the absolute and characteristic reference curves.
Additionally, the reference tracking of the level is shown, which should maintain a demanded height of 35.0 mm. The characteristic RMSE of the level results in 0.3 mm and 0.2 mm for the partial and full support, which corresponds to a percentual error of 0.4% and 0.3%. With a maximal level deviation of 0.6 mm (partial support) and 0.5 mm (full support), the level can be assumed constant.
Analogously Fig. 3.7a and Fig. 3.7b show the reference tracking with the decoupled pressure control and the optimized pinch valve control structure - the *atraumatic* design. With this control structure, the pressure errors yield a similar size as the errors of the state-of-the-art design: The characteristic RMSE arises to 0.8 mmHg and 0.6 mmHg for the left ventricle and aorta in partial support condition, and 0.4 mmHg and 0.3 mmHg in full support condition. The maximal error within partial support results in 4.3 mmHg and 1.5 mmHg for the left ventricle and the aorta, respectively, which decreases in full support to 2.4 mmHg and 0.9 mmHg. Further results are summarized in Table 3.4.
With the separate and optimized level control structure, the characteristic RMSE results in 1.4 mm and 0.5 mm considering the partial and full support condition. Here the level fluctuates around its target value with a maximal error of 2.6 mm (3.3%) and 1.0 mm (1.4%) within partial and full support condition.

Further, an experimental step from partial support to full support condition at t = 5 s is shown in Fig. 3.8a for the *state-of-the-art* design and in Fig. 3.8b for the *atraumatic* design. The four panels depict the time course of the hemodynamic pressures of the left ventricle, aorta, and the resulting head pressure, the resulting flow rate through the HM3 and pinch valve, the fluid level in the left ventricular and aortic reservoir, and the pinch valve slide (from top to bottom).
The panels of Fig. 3.8a show the measurement results of the hemodynamic experiment conducted with the decoupling MIMO control strategy and the *state-of-the-art* design, characterized by a step from partial to full support condition at $t = 5\,s$. The upper panel depicts the resulting left ventricular and aortic pressure curve, together with the resulting pressure differ-

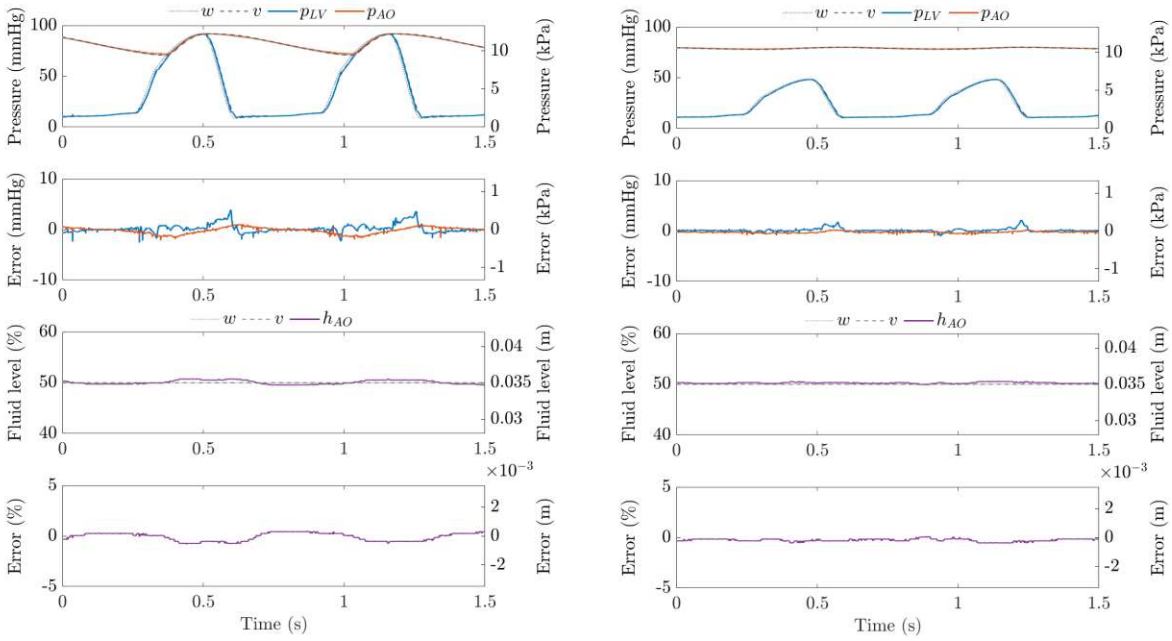

(a) Partial support.

(b) Full support.

Figure 3.6: Reference tracking with decoupling MIMO control structure and the *state-of-the-art* design.

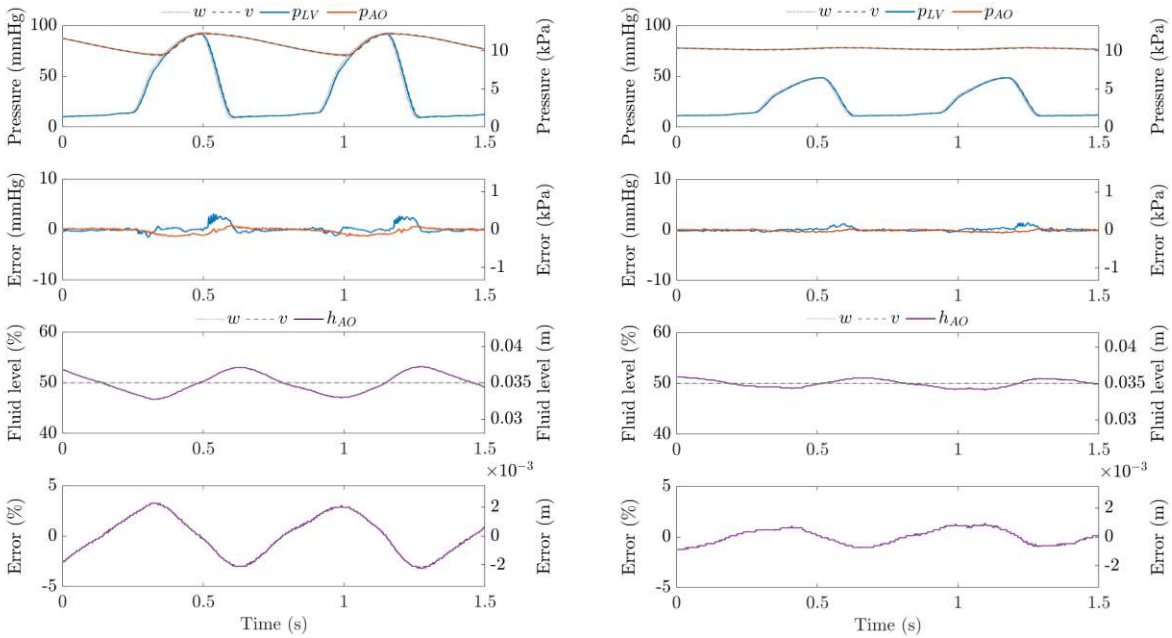

(a) Partial support.

(b) Full support.

Figure 3.7: Reference tracking with decoupling MIMO control structure and the *atraumatic* design.

Table 3.4: RMSE and maximal error of atraumatic MIMO control approach for the state-of-the-art design (MCL) and atraumatic design (A-MCL) at partial and full support, respectively

	MIMO			**Partial support**		**Full support**	
	(mmHg)			Left ventricle	Aorta	Left ventricle	Aorta
MCL	91 bpm	**e**	RMSE	3.0234	0.6792	1.3767	0.2873
			Error max.	7.9162	3.4142	4.3398	1.0724
		e*	RMSE	0.8916	0.6894	0.4088	0.2918
			Error max.	3.8984	3.0276	2.4360	1.1151
A-MCL	91 bpm	**e**	RMSE	2.9575	0.5633	1.3559	0.2322
			Error max.	8.3104	1.4237	4.0895	0.8523
		e*	RMSE	0.8378	0.6307	0.3706	0.2579
			Error max.	4.3240	1.5027	2.3505	0.9148

ence (head pressure) between the reservoirs. The pressures are changing periodically with the heart rate (91 bpm): The left ventricular pressure p_{LV} fluctuates between 91.2±0.1 mmHg and 8.5±0.1 mmHg in partial support, and between 48.3±0.2 mmHg and 10.7±0.3 mmHg in full support condition. Analogously, the aortic pressure p_{AO} alternates between 91.9±0.1 mmHg and 71.5±0.2 mmHg in partial support, and between 78.2±0.1 mmHg and 76.3±0.1 mmHg in full support condition. Due to the lower peak pressure of the ESPVR during full support, a decrease in pulsatility can be observed. With lower pulsatility, the mean head pressure H affecting the RBP increases from 44.0±30.5 mmHg to 53.7±14.2 mmHg. Therefore, the VAD flow rate Q_p fluctuates around its mean value, with a stepwise increase from 2.1±2.1 L/min to 4.5±0.6 L/min. Due to the high pulsatility in the VAD flow rate within partial support, periodical backflow of -0.3±0.0 L/min is observed during diastole. The resulting fluid levels for the left ventricular and aortic reservoir show inverse characteristics as the compliance of the pipes can be neglected: The left ventricular h_{LV} and aortic h_{AO} level fluctuate around the target level of 35.0 mm, which corresponds to 50.0% of filling, with a mean value of 35.0±0.3 mm (50.0±0.4%) in partial support, and 35.1±0.1 mm (50.1±0.2%) in full support, respectively. The level deviation does not exceed ±1% despite a stepwise change of the operating conditions.

The same step from partial to full support condition at $t = 5\,s$ is depicted in Fig. 3.8b for the *atraumatic* design with decoupled pressure control and optimized pinch valve control. Analogously the upper panel shows the resulting left ventricular p_{LV} and aortic p_{AO} pressure curve, together with the resulting pressure difference H (head pressure) between the reservoirs. The pressures follow characteristic pressure trajectories resulting from the underlying cardiac cycle with a heart rate of 91 bpm: Here, the left ventricular pressure fluctuates between 92.0±0.1 mmHg and 8.8±0.2 mmHg in partial support, and between 48.7±0.0 mmHg and 11.1±0.1 mmHg in full support condition, while the aortic pressure alternates between 92.6±0.1 mmHg and 71.4±0.1 mmHg in partial support, and between 78.4±0.1 mmHg and

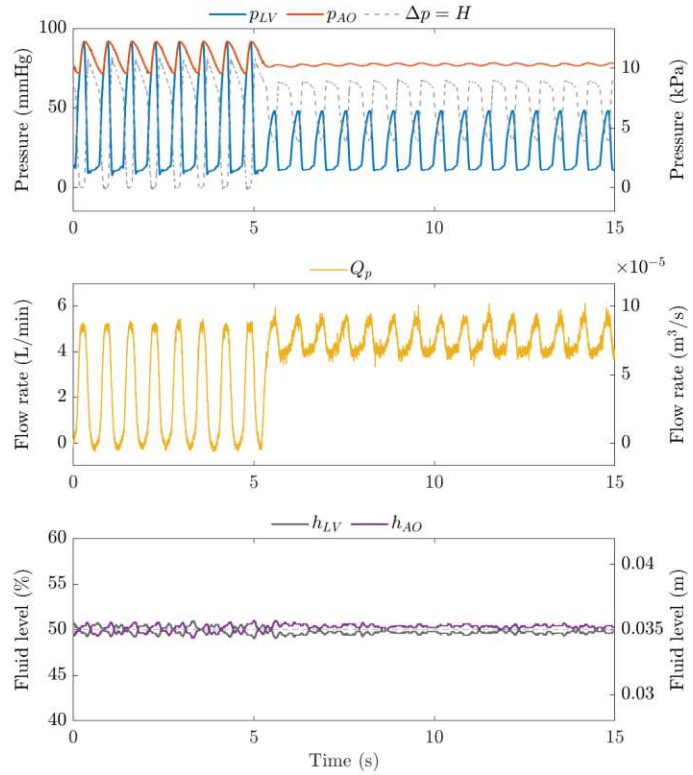

(a) *State-of-the-art* design.

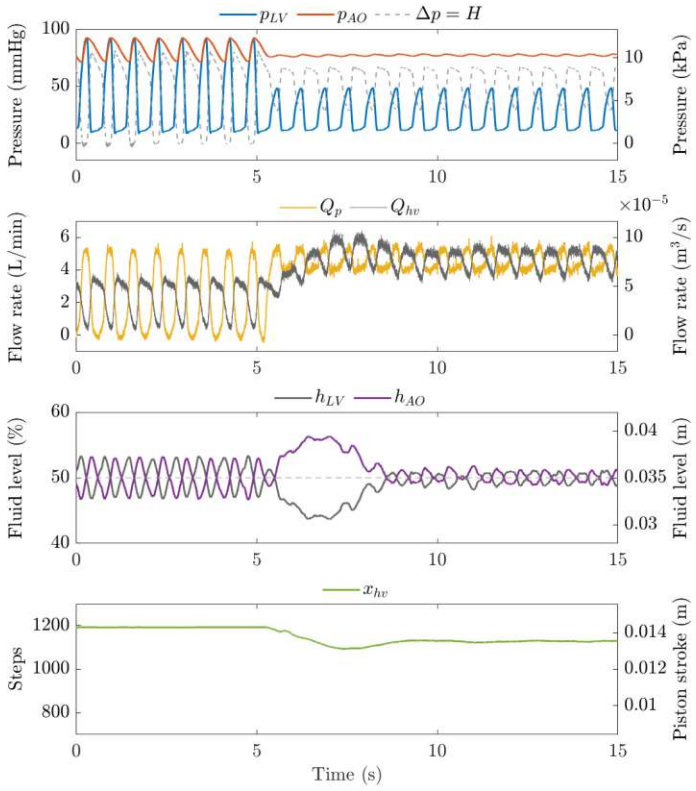

(b) *Atraumatic* design.

Figure 3.8: Measured results of a step from partial support to full support condition at t = 5 s. The four panels depict the time course of the hemodynamic pressures of the left ventricle and aorta, the resulting flow rate through the VAD, the fluid level in the reservoirs, and the pinch valve slide.

Table 3.5: RMSE and maximal error of decoupling MIMO control approach for both MCL designs at partial and full support with different dynamics

MIMO (mmHg)				Partial support		Full support	
				Left ventricle	Aorta	Left ventricle	Aorta
MCL	60 bpm	**e**	RMSE	2.2261	0.5744	1.0936	0.2469
			Error max.	7.7320	2.5953	4.3511	0.9997
		e*	RMSE	0.7130	0.4999	0.3114	0.2527
			Error max.	3.3898	2.2194	2.2773	1.0723
	120 bpm	**e**	RMSE	3.6601	0.7453	1.6763	0.2749
			Error max.	9.1234	3.2823	5.2969	1.2682
		e*	RMSE	1.1035	0.8122	0.4823	0.2792
			Error max.	4.5555	2.8337	3.1301	1.3159
A-MCL	60 bpm	**e**	RMSE	2.2228	0.5288	0.9696	0.2498
			Error max.	6.8182	1.7084	3.4411	0.8060
		e*	RMSE	0.6063	0.6194	0.2370	0.2711
			Error max.	2.7200	1.6976	1.1421	0.8909
	120 bpm	**e**	RMSE	3.4220	0.5828	1.5281	0.2450
			Error max.	9.2322	1.5147	4.4303	0.5859
		e*	RMSE	1.2285	0.6535	0.5759	0.2660
			Error max.	5.6427	1.5059	3.6648	0.6673

76.2±0.1 mmHg in full support condition. With lower pulsatility in full support condition, the mean head pressure increases from 42.7±31.3 mmHg to 54.0±14.0 mmHg. Despite, an increasing head pressure impeding the VAD flow rate Q_p, the flow through the VAD increases due to its higher speed setting. Both VAD flow rate and the corresponding backflow through the pinch valve Q_{hv}, show a stepwise increase from 2.3±2.1 L/min to 4.6±0.5 L/min. The VAD and pinch valve flow rates pulsate inversely, which is induced by the hemodynamic pressure curves. Due to a high pulsatility in the VAD flow rate within partial support, periodical backflow of -0.2±0.1 L/min is observed during diastole. In contrast, the flow rate in the pinch valve shows less pulsatility with an all positive flow rate. The resulting fluid levels for the left ventricular h_{LV} and aortic h_{AO} reservoir show inverse characteristics. The left ventricular and aortic level fluctuate around the target level of 35.0 mm, with a mean value of 35.0±1.5 mm (50.0±2.1%) in partial support, and 35.1±0.6 mm (50.1±0.8%) in full support, respectively. The level deviation does not exceed ±6% despite a stepwise change of the operating conditions. The pinch valve slide x_{hv} can be assumed constant with 1193±1 step and 1127±2 steps, which corresponds to 0.012 mm and 0.024 mm valve movement in partial and full support condition. Only in case of a stepwise change of the operating condition, a temporary valve action (100 steps, 1.2 mm) is apparent.

Different dynamics within the experiments were assessed by changing the heart rate to 60 bpm and 120 bpm, respectively.
Fig. 3.9a and Fig. 3.9b show the reference tracking for different dynamics at partial and

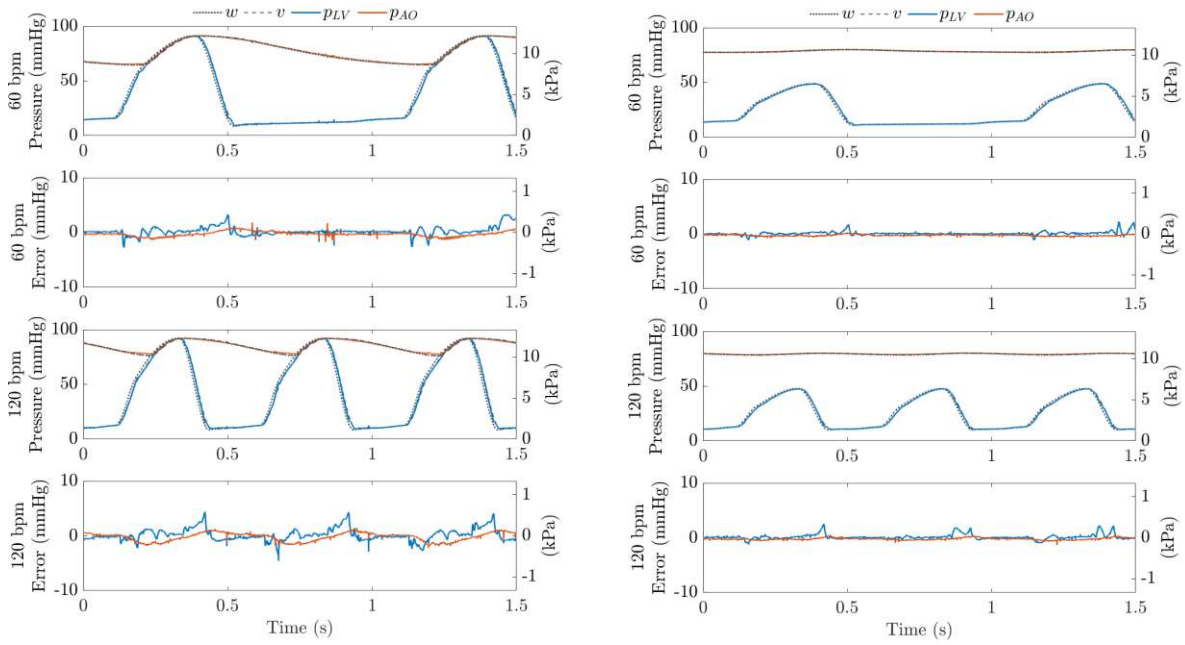

(a) Partial support.

(b) Full support.

Figure 3.9: Reference tracking with decoupling control strategy and *state-of-the-art* design for partial and full support with different heart rates (dynamics).

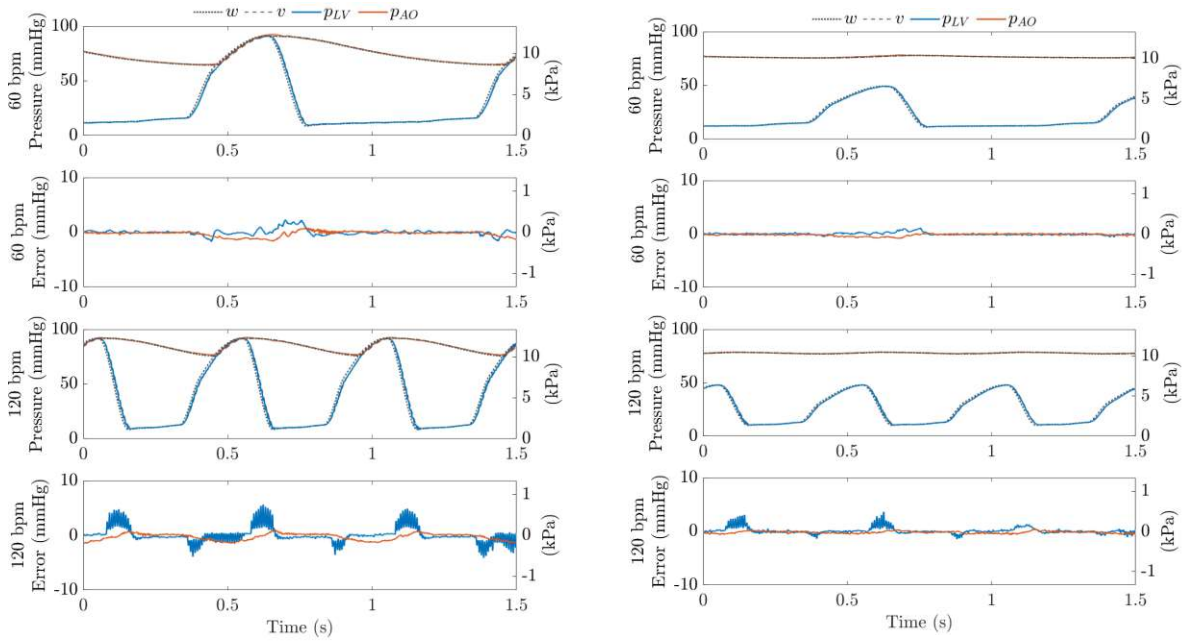

(a) Partial support.

(b) Full support.

Figure 3.10: Reference tracking with decoupling control strategy and *atraumatic* design for partial and full support with different heart rates (dynamics).

full support condition with the *state-of-the-art* design: At 60 bpm the characteristic left ventricular RMSE results in 0.7 mmHg in partial support, and 0.3 mmHg in full support condition. It increases at 120 bpm to 1.1 mmHg and 0.5 mmHg in partial and full support, respectively. This corresponds to an error growth of 0.01 mmHg/bpm. The aortic pressure is less affected by changing dynamics, with an left ventricular increase in the characteristic RMSE from 0.5 mmHg to 0.8 mmHg in partial support condition, which corresponds to an error growth of 0.005 mmHg/bpm.
Similarly, the effect of changing dynamics on the reference tracking results is shown in Fig. 3.10a and Fig. 3.10b for the *atraumatic* design: At 60 bpm the characteristic RMSE of the left ventricle is 0.6 mmHg in partial support and 0.2 mmHg in full support condition. It doubles at 120 bpm to 1.2 mmHg and 0.6 mmHg, respectively, which corresponds to an increase of of 0.01 mmHg/bpm. Here, the dynamics show no effect on the reference tracking of the aortic pressure. Further results are stated in Table 3.5.

3.2.3 Model accuracy

To evaluate the model described in section 2.2, simulation results were compared to the measured data, as shown in Fig. 3.11a and Fig. 3.11b for the state-of-the-art design in partial and full support condition, respectively. This shows good congruence of the measured and simulated data with a maximal RMSE of 0.8 mmHg, which results for the left ventricular pressure at partial support. The level error is also maximal in partial support condition and yields 0.3 mm, which corresponds to 0.4% of the fluid level.
Further, the results of the *atraumatic* design are shown in Fig. 3.12a and Fig. 3.12b, analogously for partial and full support. Here, the RMSE of the left ventricular pressure in partial support condition is slightly higher, it results in 1.0 mmHg. The other pressure errors are smaller, which indicates a good fit. The lower panel of Fig. 3.12a shows a phase shift of the simulated fluid level compared to the measured data. This results in a RMSE of 1.1 mm or 1.6% of the fluid height. The phase shift is also present in full support, resulting in a RMSE of 0.3 mm (0.4%). Further errors are stated in Table 3.6.

Table 3.6: RMSE of measured and simulated MIMO control approach for both MCL designs at partial and full support

MIMO			**Partial support**	**Full support**
			RMSE	
MCL	Left ventricular pressure	(mmHg)	0.7705	0.3562
	Aortic pressure	(mmHg)	0.6111	0.2452
	Aortic fluid height	(m)	$2.6077 \cdot 10^{-4}$	$2.0506 \cdot 10^{-4}$
A-MCL	Left ventricular pressure	(mmHg)	0.9647	0.5179
	Aortic pressure	(mmHg)	0.6813	0.2568
	Aortic fluid height	(m)	$11.042 \cdot 10^{-4}$	$3.3766 \cdot 10^{-4}$

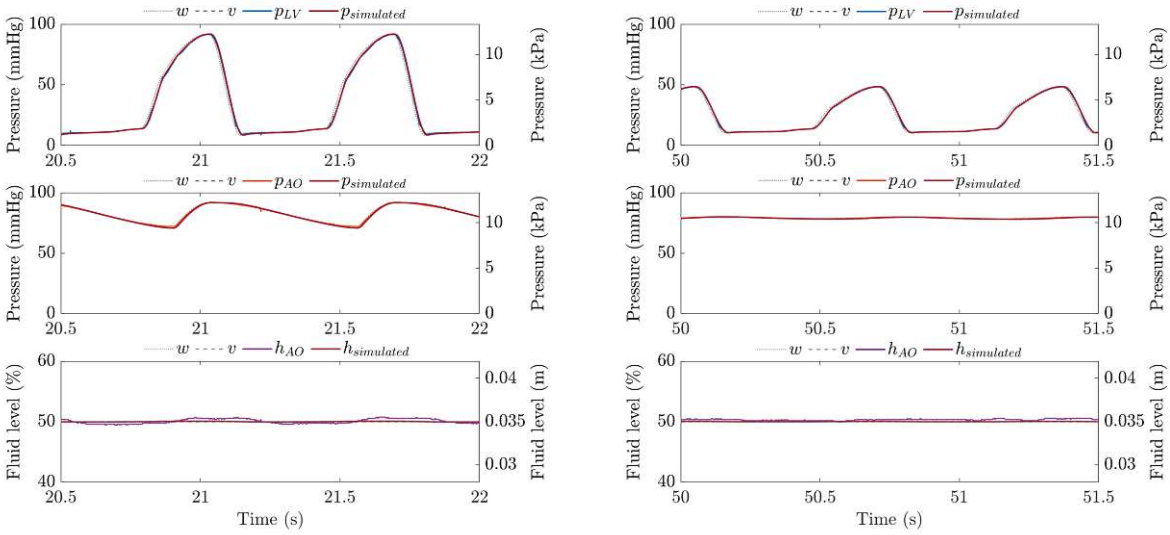

(a) Partial support.

(b) Full support.

Figure 3.11: Measured and simulated results for the *state-of-the-art* design at partial and full support condition.

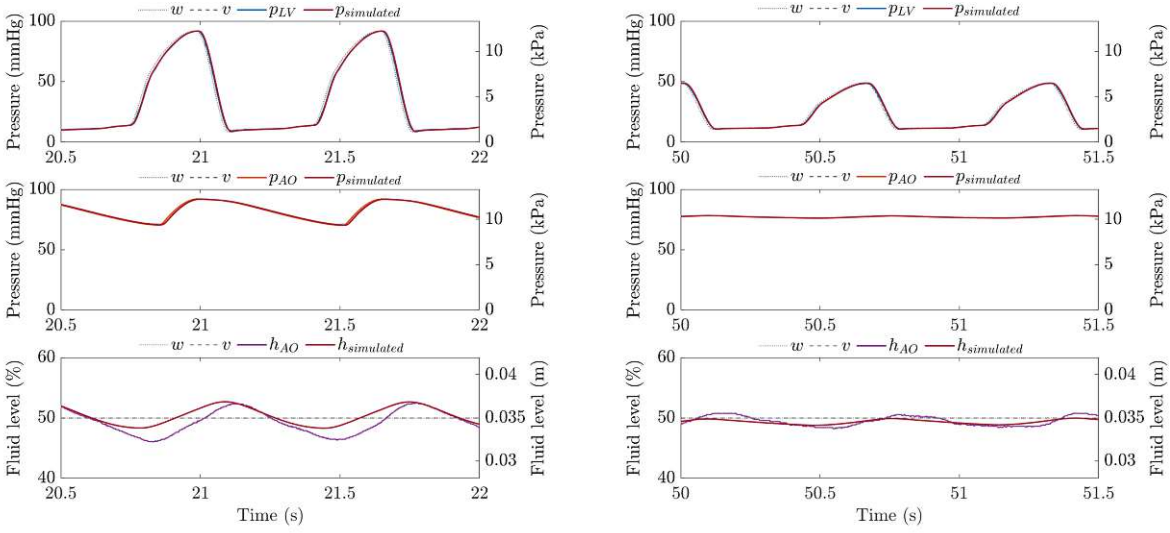

(a) Partial support.

(b) Full support.

Figure 3.12: Measured and simulated results for the *atraumatic* design at partial and full support condition.

4 Discussion

This thesis presented a novel, atraumatic H-MCL design, which forms a realistic hemodynamic environment for a RBP and allows the enhancement conventional blood trauma assessment. Further, an additional H-MCL design was described, which analogously generates realistic hemodynamic pressures and flows, while it retains the advantages of state-of-the-art H-MCLs with additional pumps.

Within this scope, a previously described H-MCL concept [19] was advanced for the use with blood. Novel design features comprise a low volume design (550±50 ml), diluted from one standard blood bag. The hydraulic circuit contains two sealed reservoirs acting as pressure generating interfaces, a RBP under investigation and hemocompatible tubing to close the loop, which are the only blood contacting components. All sensors and actuators were chosen with the feature to operate without direct blood contact: A novelty was the implementation of a proportional pinch valve, which allows an adaptation of the hydraulic resistance by pinching the tubing and therefore a control of the blood flow rate without blood contact. Further a heating concept was developed to maintain a consistent blood temperature of 37°C. All design choices were made in accordance with the ASTM standards [15, 16], resulting in similar blood contacting components with the exception of one additional reservoir. These design choices were adopted for the described state-of-the-art design, with the exception that a gear pump was implemented in place of the proportional pinch valve and heating was not necessary due to the use of a water-glycerol mixture, which was adapted to the viscosity of blood (3.5 cP) at room temperature.

These hardware setups required capable control strategies for both design choices: It was shown that the reference pressures of the multivariate system were precisely tracked by the novel decoupling control strategies without apparent coupling effects. Based on the method of feedback linearization, the novel control strategies are decoupling the multivariate systems, while inherent nonlinearities are compensated. This led to significantly improved trajectory tracking results compared to conventional SISO control structures.

With a conventional H-MCL a SISO control structure was successfully implemented [19], applying such strategy [1] to the novel H-MCL designs indicated strong inherent coupling effects, despite careful tuning of the parameters. This manifests itself in coherent deviations from a characteristic reference signals interrupted by recurring periods of precise trajectory tracking.

This becomes visible for both designs in partial support condition (cf. Fig. 3.4a and Fig. 3.5a), where pronounced pressure changes within a reservoir induce errors in the other reservoir, and vice versa. Although, the resulting RMSE is in an acceptable range with 3.8 mmHg (state-of-the-art- design) vs. 4.1 mmHg (atraumatic design), such deviations could affect the RBP flow rate, especially in flat regions of the pumps HQ-curve, where small pressure deviations are connected to large changes of the resulting flow rate [9]. Therefore, a conventional SISO control approach does not meet the requirements for adequate reference tracking with the described hardware choices of the novel H-MCL designs. With a different hardware setup a SISO approach might be sufficient, especially if the resistance between the reservoirs is higher due to longer tubing, additional pumps or a different RBP under investigation. Such higher resistance would reduce coupling effects. Of note, the pump design of the HM3 is characterized by large fluid gaps, which reduces the flow resistance through the pump and therefore fosters coupling effects within the system.

Atraumatic design.
The novel control strategy of the atraumatic design is characterized by two complementary parts, a decoupling pressure control paired with an atraumatic level control structure. The decoupling pressure control addresses both pneumatic proportional valves, which inflate or deflate the reservoirs to meet a defined target pressure. This forms a controllable subsystem, which allowed the formulation of a decoupling control law based on the method of feedback linearization: The decoupling control approach (MIMO) of the atraumatic H-MCL leads to significantly improved trajectory tracking of the hemodynamic pressures with a twofold decreased mean RMSE of 1.3±1.2 mmHg compared to 2.8±0.9 mmHg for the SISO control. The mean RMSE reduces even further to 0.5±0.3 mmHg, which corresponds to the magnitude of the measurement error of the pressure sensors used, when the reference behavior of the implemented decoupling pressure control is considered. A change in the reference dynamics has only minor impact on the RMSE of the novel H-MCL; it increases with +0.01 mmHg/bpm. Accordingly, the novel decoupling pressure control was able to consistently meet the requirements of accurate reference tracking for the novel H-MCL design.
With the atraumatic design the decoupling control law was supplemented by an atraumatic level control structure addressing the pinch valve slide. As atraumatic actuator the pinch valve allows a defined flow control without direct blood contact by continuously adapting the flow resistance. Controlling the pinch valve was complicated by two limitations: First, loss of controllability was observed (e.g. in case of partial support during systole), with zero pressure difference across the pinch valve. In this case the pinch valve flow rate approaches zero, which can not be addressed by a change of the resistance (consequently the pinch valve condition does not affect the system). Second, atraumatic pinch valve performance has to be ensured (to comply with the ASTM standards), which permits only marginal motion of the pinch valve. This context was assessed in an optimization task, with defined boundary conditions, to determine a suitable control trajectory for the pinch valve for one complete cardiac cycle. As this optimization task was not solved in real time, only the findings could be used to derive a control strategy:

The optimization task showed that both partial and full support condition can be controlled by a constant valve position without violating the boundary conditions of the fluid level. This led to a control approach, which required averaging of the system states over the last cardiac cycle to determine the non-zero mean head pressure across the pinch valve. Considering the running mean of the last heart cycle, loss of controllability is circumvented (as the mean pressure difference across the pinch valve is non-zero with hemodynamic reference pressures) and therefore a control of the mean flow through the pinch valve is enabled. This control method is suitable for a cardiovascular model characterized by a constant heart rate (cf. section 2.2.1), as the length of one cardiac cycle has to be known (and set as buffer size in underlying model).
The derived level control structure addresses both limitations successfully: The fluid volumes of the reservoirs were balanced ($< 5\%$) with marginal motion of the pinch valve (< 0.03 mm). Accordingly, blood trauma experiments with the novel atraumatic H-MCL and the standardized constant hemolysis assessment of RBP are comparable, as similar hardware and an approximately static resistance is used. Although this strategy limits the time constant of the fluid level control, the experiments indicated a sufficiently fast response with less than $\pm 6\%$ level deviation with the non-physiologic step from partial to full support condition. Of note, changes in the reservoir's fluid volume cannot be eliminated completely due to the periodic lack of controllability during systole, which leads to a temporary level increase in the aortic reservoir.

Within pilot experiments with blood, the hardware choices and this novel atraumatic control structure have proven to be suitable to perform hemocompatibility assessments of blood pumps. In the scope of blood experiments, the normalized index of hemolysis (NIH) was measured in accordance with the ASTM standards [15, 16], and as described in [11, 12], for a static (state-of-the-art) and pulsatile operation (light pulsatility: full support condition) of the novel atraumatic H-MCL. Where the operating conditions were characterized by the same mean pump flow (about 4.5 L/min). The resulting NIH is described qualitatively within this scope: Its values are consistent with previously reported numbers in the literature for both bovine blood [31] and human blood [32]. Consequently, conducted preliminary in-vitro investigations using bovine and human blood do not indicate significant traumatic effects of the novel H-MCL compared to static mock loops that are considered state-of-the-art.

Of note, within experiments with blood, the capacitive level sensors have shown to be sensitive to foam formation and adhesion of blood particles to the reservoir surface, affecting the level measurement. One attempt to improve level measurement was to use an ultrasonic level sensor applied to the reservoir lid, however the ultrasonic method was affected by condensed water droplets on the sensor surface within the reservoir, leading to temporary failure of the measuring signal, which was therefore dismissed.
The decoupling control law is based on the inherent dynamics of the system, and therefore affected concurrently by an inaccurate level measurement. With these limitations in mind, a different set of poles was chosen by FSF (clp = -70), which led to a stable operation of

the system and good trajectory tracking with the presented capacitive level sensors (cf. section 2.1). This reference behavior is ranked in Fig. 4.1, which is still a distinct improvement without apparent non-physiologic deviations compared to a SISO control approach.

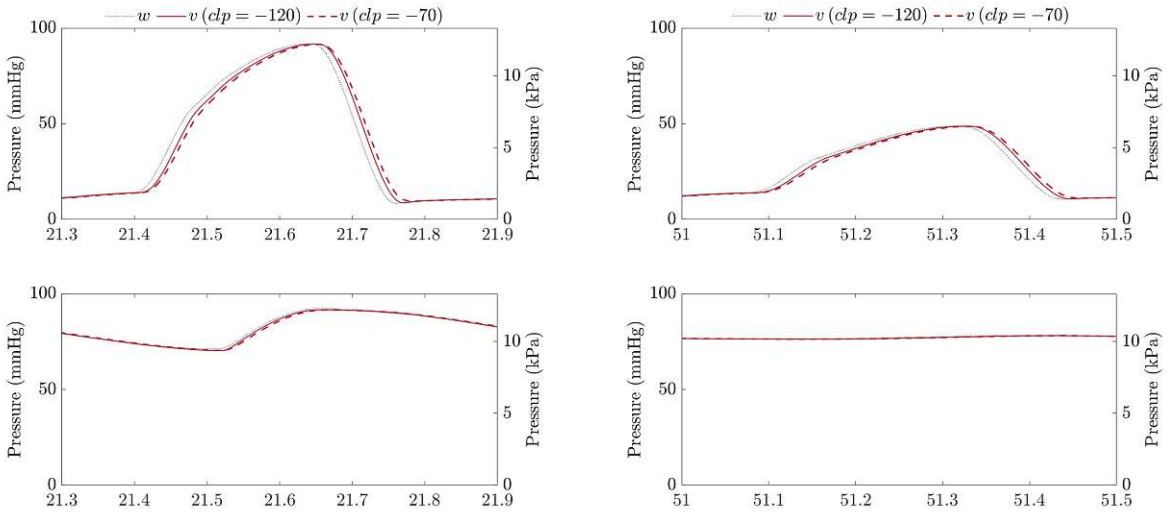

(a) Partial support.

(b) Full support.

Figure 4.1: Simulated reference behavior with chosen closed loop poles (clp) with the *atraumatic* design at partial and full support condition.

State-of-the-art design.
The state-of-the-art design is based on similar components as previously suggested by Ochsner et al. [19]. Despite a similar conception, a SISO control approach as proposed within this paper, was not sufficient in terms of adequate reference tracking: The novel state-of-the-art design is characterized by a low volume design, short tubing and an actual RBP (the HM3), which leads to an overall low flow resistance within the system and therefore increased coupling effects. Therefore, the novel control strategy of the state-of-the art design comprises a decoupling control structure addressing both pressures and levels within the system. This was possible as no loss of controllability occurs with the additional gear pump, which replaces the pinch valve of the atraumatic H-MCL design. This unfolds the full potential of feedback linearization and dynamic extension, and allows to choose a defined reference behavior for both pressure and level control. This decoupling control strategy leads to a significantly improved trajectory tracking of the hemodynamic pressures, analogously to the atraumatic design with a twofold decreased mean RMSE of 1.3±1.2 mmHg compared to 2.4±1.2 mmHg for the SISO control. The mean RMSE referring to the characteristic reference behavior reduces to 0.6±0.3 mmHg. Here, the level control shows no loss of controllability, and is therefore also addressed by the nonlinear decoupling control law. This leads to an improved trajectory tracking compared to atraumatic design, where the level fluctuates around the target value

up to ±5%. With the decoupling level control the level fluctuation is only marginal resulting in ±0.5% and does not exceed ±1% despite a challenging step from partial to full support condition. Considering different reference dynamics, the RMSE of hemodynamic pressures the novel H-MCL increases only slightly with the heart rate (+0.01 mmHg/bpm).
Accordingly, the decoupling control strategy consistently met the requirements of accurate reference tracking for the state-of-the-art H-MCL design.

The simulation of the novel H-MCL designs is based on the numerical models of the implemented components as described in section 2.2. This allowed preceding assessments of controller parameters, and transfer behavior based on chosen hemodynamic references. The simulation was modelled in Simulink which allows simple adaptions in case of hardware changes due to its block representation. As representative a simulation model is described in appendix B.3 for the atraumatic design.
The simulation was used in early stages to determine the decoupling characteristics of the derived control structure and to ensure that the actuator limits are avoided within all considered hemodynamic conditions. Later the quality of this simulation was assessed by comparing simulated and measured values from experimental studies. This showed good agreement, indicating a good fit of the numerical representation and the physical hardware:
With the atraumatic design the simulated and measured pressures show good agreement for both partial and full support condition with a maximal mean RMSE of 0.8±0.2 mmHg. Given this design, the measured and simulated levels fluctuate with similar frequency and amplitude around its target value, while in partial support condition a phase shift is visible. The measured signal is slightly delayed compared to the simulated data, which may be attributable to non-optimal modeling of the inertias in the piping of the system. Within full support this phase shift is also present but hardly visible due to a small signal amplitude. Therefore, the RMSE of the levels results in 1.1 mm (1.6%) and 0.3 mm (0.4%).
Moreover, the simulation results of the state-of-the-art design are in good accordance with the experimental measurements, which leads to an overall small mean RMSE of 0.5±0.2 mmHg for both partial and full support condition and a small level error resulting in a mean RMSE of 0.2±0.04 mm.
These errors are all in an order of magnitude of the measurement accuracy of the sensors used. Accordingly, the simulation models provide a precise tool for preceding evaluations prior to experimental studies, and could reveal critical operating conditions.

5 Conclusion

Within this thesis a novel atraumatic H-MCL was successfully implemented, which is characterized by an atraumatic low volume design and an advanced control strategy. Hemodynamic experiments showed that the implemented control strategy is able to decouple the pressures of the system, which reflects in precise reference tracking of the hemodynamic conditions. This control strategy further comprises an atraumatic level control approach, which was assessed within an optimization task to ensure marginal actuator effort while periodical loss of controllability was observed. Atraumatic properties were assessed by pilot blood trauma experiments which indicated atraumatic behavior of the setup in both static and pulsatile operation. Hence, the novel atraumatic H-MCL enables in-vitro hemocompatibility assessment of physical RBPs within realistic hemodynamic conditions.

Besides the presented application, several possibilities for studies with the novel H-MCL are conceivable. The setup allows simple connection of other RBPs and pump prototypes due to its modular design. Appropriate connectors can be provided in a timely manner by additive manufacturing allowing plug and play connection. Moreover, the numerical model of the cardiovascular model can be flexibly adapted, and assigned to the interface of the H-MCLs, or even exchanged to meet other patient data. Accordingly, various clinical questions can be assessed: Including experiments without any pumps, as shown in appendix B.4, which allows an identification of the hemolytic effect of different resistances (nozzles or edges within a flow profile), to gain a better understanding of blood trauma effects of the chosen hardware in future in-vitro hemocompatibility studies. Alternatively, in-vitro implantation of a RBP at the left atrium or the right ventricle are conceivable. The described setup therefore extends the application scenario of state-of-the-art H-MCLs and allows the investigation of dynamic blood trauma effects of RBPs, e.g. the impeller displacement in LVADs with magnetic bearings or a periodic negative flow rate during diastole in LVADs operating at low speed or high arterial pressure.

Concurrently, this atrauamatic H-MCL was compared to a state-of-the-art design, with similar hardware choices and an advanced decoupling control structure. Such setup allows a wide range of hemodynamic assessments preserving the advantages of the conventional conception with additional pumps. The state-of-the-art design is able to map a wide flow range, which allows the assessment of further implants as heart valves or intra-aortic balloon pumps and enables a systematic identification of prototypes, e.g. characteristic pump HQ-curves.

These H-MCL designs are favorably complementing each other, which leads to an outstanding research platform to address cardiovascular diseases.

Appendix A

Background to the research field

A.1 Cardiovascular System

The cardiovascular system is composed of the heart, the blood vessels and the blood. Its main task is to keep the body within well-defined limits, balancing external stimuli: This state of equilibrium is called homeostasis.
The blood circulation can be modelled, anatomically and functionally correct, as a closed loop with two pumps in series, the left and the right side of the heart (Fig. A.1).
The human heart is a hollow muscle that generates a blood flow by contracting chambers and associated valves, which direct the flow. Each half of the heart consists of two chambers, the atrium (antechamber) and ventricle (main chamber), which contract periodically with the cardiac cycle.
Generally, the blood flows from the ventricle in increasingly refined arteries into the vessels of an organ. There, oxygen and other products are exchanged. From the vessels, the blood collects in constricting veins that lead to the atrium of the other ventricle. In this way, the left side of the heart supplies the systemic circulation, which provides all body tissues with oxygen-rich blood. Whereas, within the pulmonary circulation, the right side of the heart propels oxygen-depleted blood to the lungs, where it is reoxygenated.
In Fig. A.2 the pressure-volume (PV) loop of the cardiac cycle is shown for the left half of the heart: Beginning with filling of the ventricle (*diastolic filling*), the blood flows from the main vein in the left atria and trough the open mitral valve in the left ventricle. *Systole:* Reaching the end diastolic volume the mitral valve closes and the musculature surrounding the ventricle compresses (*isovolumetric contraction*), which increases the internal pressure. When the internal pressure equals the aortic pressure, the aortic valve opens so that the pressurized blood can be expelled to the aorta (*systolic ejection*). *Diastole:* With decreasing pressure the aortic valve closes and the heart relaxes to be refilled. Since the pressure in the left ventricle is initially higher than the pressure in the left atrium, the pressure decreases without an increase in volume (*isovolumetric relaxation*). With opening of the mitral valve the next cycle starts.
The heart pumps intermittently with each cardiac cycle: since the blood cannot flow through the aorta as quickly as it is expelled through the ventricle, part of the volume is stored in

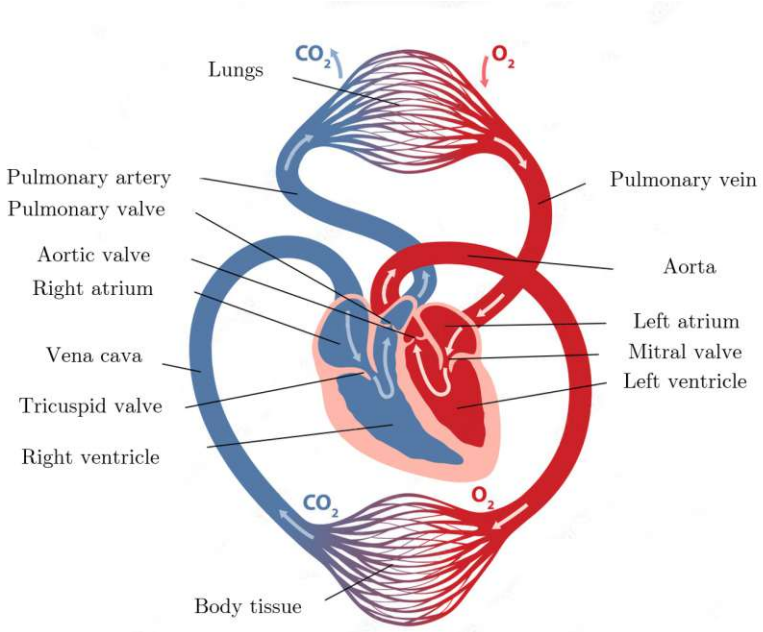

Figure A.1: Coronal section diagram of the human heart with normal morphology. Based on [33]

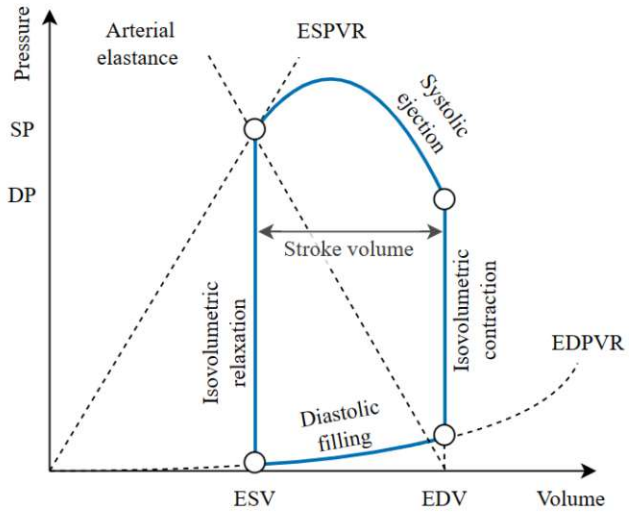

Figure A.2: Pressure-volume loop of a healthy left ventricle, with phases of the cardiac cycle and relevant performance indices: end-diastolic-pressure-volume-relationship EDPVR, end-systolic-pressure-volume-relationship ESPVR, diastolic pressure DP, systolic pressure SP, end-diastolic-volume EDV, and end-systolic-volume ESV. Based on [34]

the aorta and its elastic branches, which act as a pressure vessel. This effect is known as the *windkessel* effect. After systole, this permits blood to be continuously pushed into the branched arterial system, where the pressure waves decay, leading to a steady blood supply. Therefore the pulsatility of the left ventricle is affecting the aortic pressure only near the heart, resulting in a higher less pulsatile pressure curve, compared to the left ventricle. The dynamics of these characteristic pressure and flow conditions of the heart are described as hemodynamics. [35]
The PV loop can be used to display and determine further important performance indices of the heart, e.g. the stroke work (external work) per beat that is represented by the enclosed area of the PV loop. In addition, the ejection fraction (proportion of blood that leaves the heart per beat), can be determined from the relationship between stroke volume and end-diastolic volume. The end-diastolic pressure-volume relationship (EDPVR) allows conclusions on the relaxation of the heart, while the end-systolic pressure-volume relationship (ESPVR) permits statements on the contractility. Additionally, the cardiac output (CO) can be calculated (product of stroke volume and heart rate), to name a few.
Typically HF can be divided in patients with a reduced contractility of the heart which results in a lower slope of the ESPVR curve and patients with a stiffer structure inhibiting a proper filling of the heart, which is resulting in a higher EDPVR curve. Both types of HF patients are characterized by a shifted PV loop with the common feature that the stroke volume decreases. The CO is the product of heart rate and stroke volume: By increasing the heart rate, the system can partially compensate for the deficient volume, nevertheless with progressive stage, the body tissues are undersupplied, which is detrimental to health and quality of life. Often this leads to a downward cycle at which end, in the case of severe heart failure, a heart transplantation or the implantation of an MCS device is the last therapy option that remains. [34, 35]

A.2 Mechanical Circulatory Support

MCS has evolved significantly in recent decades from the use of pulsatile volume displacement pumps to continuous flow RBPs. These offer several advantages, e.g. a smaller pump size, fewer moving parts, limited blood contacting surfaces, and lower noise, which has translated into improved clinical outcomes. Therefore continuous flow RBPs in the form of LVADs have now replaced heart transplantation as the most common surgical treatment for end-stage heart failure. [36]
History and development (more information can be found in [37, 38]) of MCS has translated in a state-of-the-art LVAD design, based on a radial-flow rotodynamic pump structure: Such continuous flow pump consists of a single internal rotating element, the impeller, that propels blood from the inlet to the outlet port by spinning at high speeds. The impeller is fully magnetically levitated, to create wide flow paths for the blood. Today the only commercially available durable MCS with this characteristics is the Heartmate 3 ((HM3), Abbott Inc, Chicago, USA). The application of the HM3 in a clinical environment is schematically shown

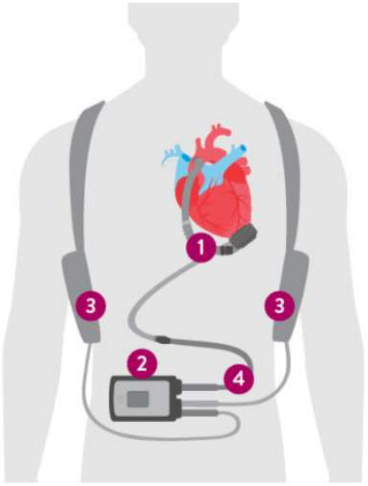

Figure A.3: Schematic application and essential components of the HeartMate 3 system: 1) HM3 LVAD, 2) system controller, 3) batteries, and 4) modular driveline. Based on [39]

in Fig. A.3: The HM3 (1) is implanted with its inlet cannula at the left ventricle, pumping the blood via the outflow graft directly to the aorta. This parallel implantation allows the failing heart to be supported (partial support, e.g. the aortic valve is still opening) or completely bypassed (full support, e.g. the aortic valve is not opening). Such unloading of the left ventricle reliefs the heart, while it increases the cardiac output and therefore enables a better supply of the body tissue. The pump is controlled, monitored and powered by a modular driveline (4), which is connected to a system controller (2) and thus batteries (3). [39, 36]
Continuous flow pumps, such as the HM3 do not generate pulsation if they are operated in with a constant operating speed. However, as they operate in conjunction with the native heart they are affected by the hemodynamics of the left ventricle and consequently by its pulsatile characteristics. The generated flow is therefore continuous with superimposed pulsatile flow changes caused by the hemodynamic pressure differences within each cardiac cycle. Since the pulsatility depends on the hemodynamic condition and the pump speed, it varies between small and large amplitudes.[36] This can lead to critical operating modes in which disturbed flow profiles occur, e.g. brief negative flow rates within the pump, despite high impeller speeds. This raises questions about the hemocompatibility of RBPs in operating modes outside the targeted operating point.
An important factor of hemocompatibility is the investigation of shear stresses applied to the blood. In a native cardiovascular system, shear stresses affecting the blood are in a defined range never exceeding certain limits. This cannot be guaranteed with MCS devices as the impeller may produce nonphysiologic flow profiles and therefore an uneven washout of pump. Consequently, this may lead to reverse advents, such as hemolysis, thrombosis or excessive bleeding. [40, 11] Further information on the hemocompatibility of MCS devices can be found in [40].

A.3 Mock Circulatory Loops

In the research and development of MCSs, various preclinical tests are performed to assess the interaction of the MCS with its physiologic environment, which can be divided in *in-silico*, *in-vitro*, and *in-vivo* methods. The platform of these methods is referred to as mock circulatory loop (MCL): Today, in-silico methods are often used as a starting point, where all physiologic components of the cardiovascular system are modelled virtually to simulate the interaction with the MCS under development. Next to these, in-vitro models that simulate the cardiovascular system with physical components are developed, which allow the investigation of physical prototypes, prior to in-vivo experiments. Finally in-vivo tests based on animal studies are conducted, where the inherent physiology allows tests close to the clinical application. Important advantages and disadvantages of preclinical tests, are summarized in Table A.1.

Table A.1: Advantages and disadvantages of preclinical test methods. Based on [19, 1]

	In-silico	*In-vitro*	*In-vivo*
⊕	Absolute repeatability and controllability High flexibility and modularity	High repeatability and controllability Features can be modelled without complete understanding	Inherent physiological behavior Close to the clinical setting
⊖	Often physiological aspects are neglected Certain features are difficult to model Prototypes cannot be tested	Complex and expensive Certain features are difficult to model Undesired effects are present	Time consuming and expensive Mammal specific results Low repeatability and controllability

Mock circulatory loops (MCL) have become a capable platform for the development and assessment of VADs, by mimicking a realistic hemodynamic environment. Cappon et al. [17] reviewed 128 MCLs published until September 2020, despite a varying complexity of the recent MCLs no setup is described that is designed to replicate realistic hemodynamic conditions without inducing blood trauma. Since such experimental setups that allow hemocompatibility assessment under realistic hemodynamic conditions are still an unmet development, in-vitro analysis of blood trauma mechanisms is restricted to static experiments with constant flow and pressure. [15, 16]

Appendix B

Supplementary material

B.1 Electrical diagrams

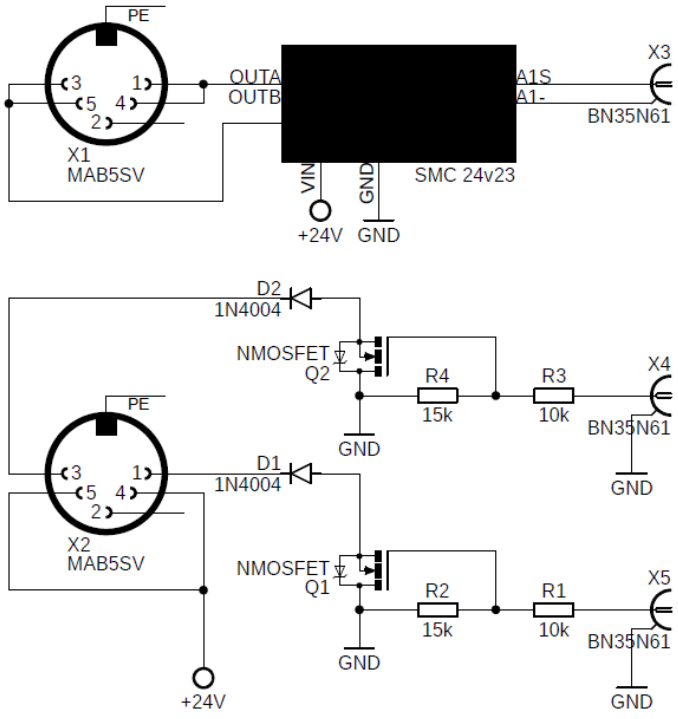

Figure B.1: Wiring diagram of connection box A, connecting the gear pump via X1 and X3 with a motor driver SMC 24v23, while switching the safety valves via X2, X4 (valve 1) and X5 (valve 2).

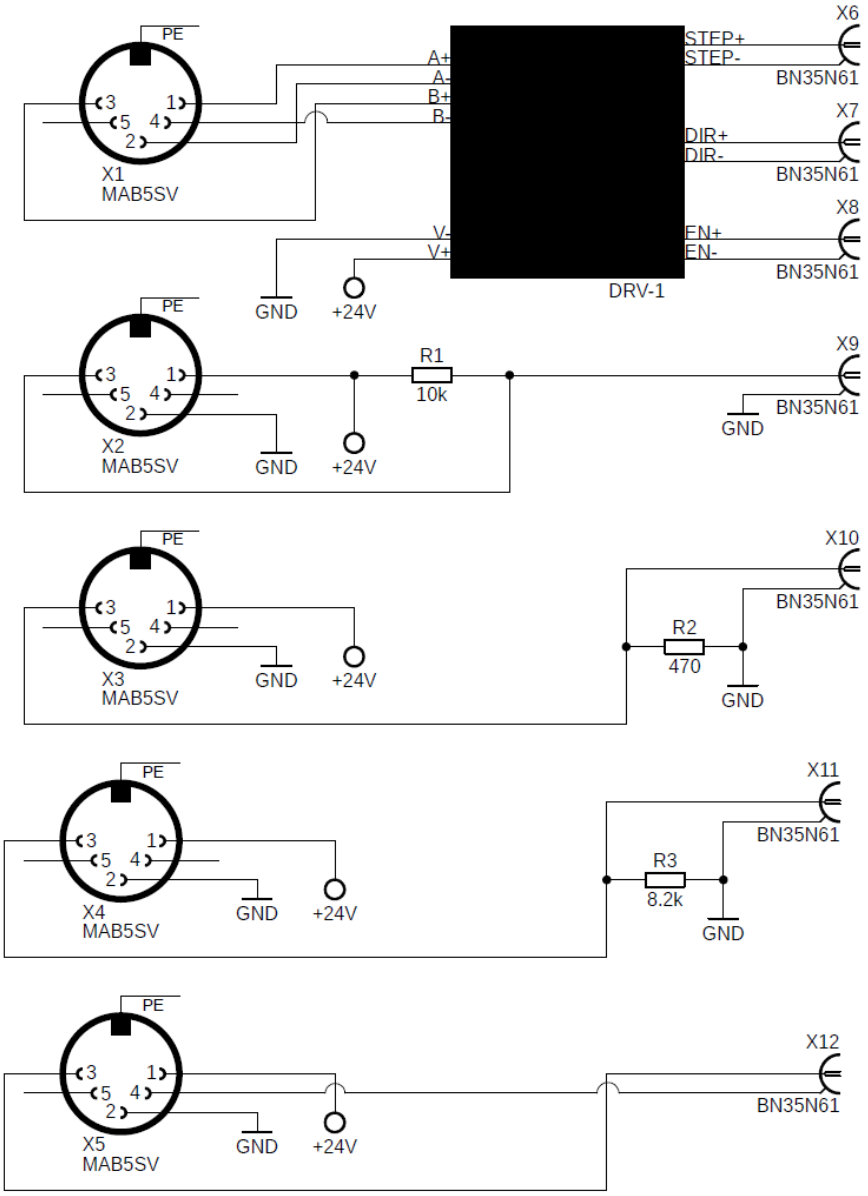

Figure B.2: Wiring diagram of connection box B, connecting the pinch valve via X1, X6 (STEP), X7 (DIR) and X8 (EN) with the motor driver DRV-1. The inherent hall sensor of the pinch valve is connected by X2 and X9. The flow sensors are addressed by X3 and X10. The level sensors are conncted by X4 and X11. And the pneumatic proportional valves are connected according to X5 and X12.

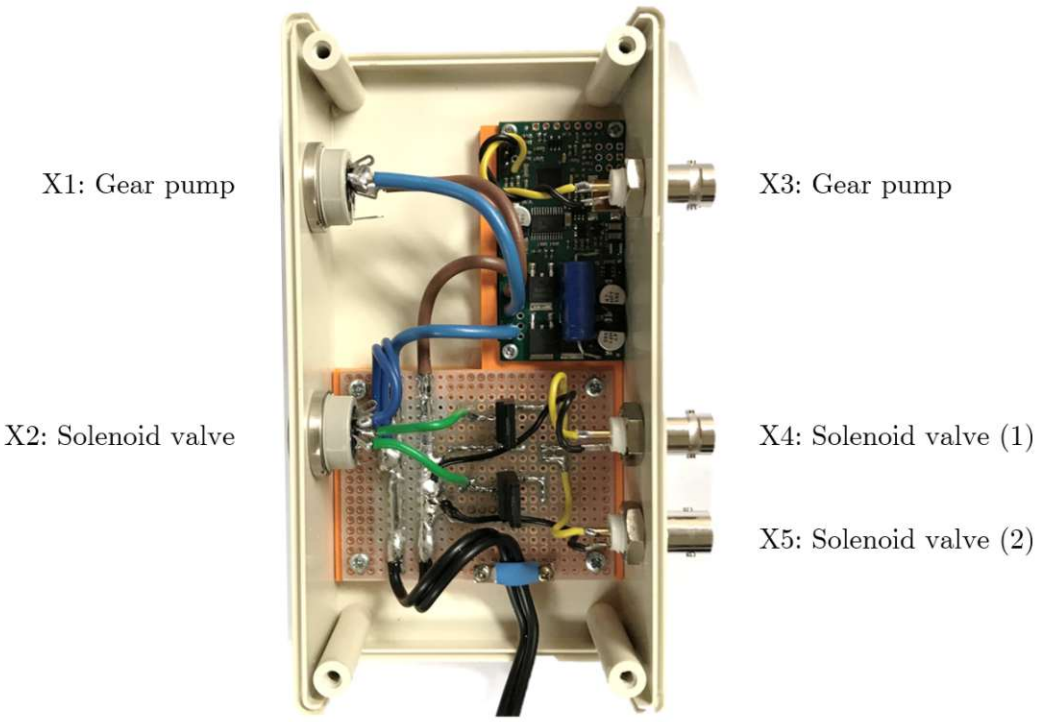

Figure B.3: Connection box A, connecting the gear pump via X1 and X3 with a motor driver SMC 24v23, while switching the safety valves via X2, X4 (valve 1) and X5 (valve 2).

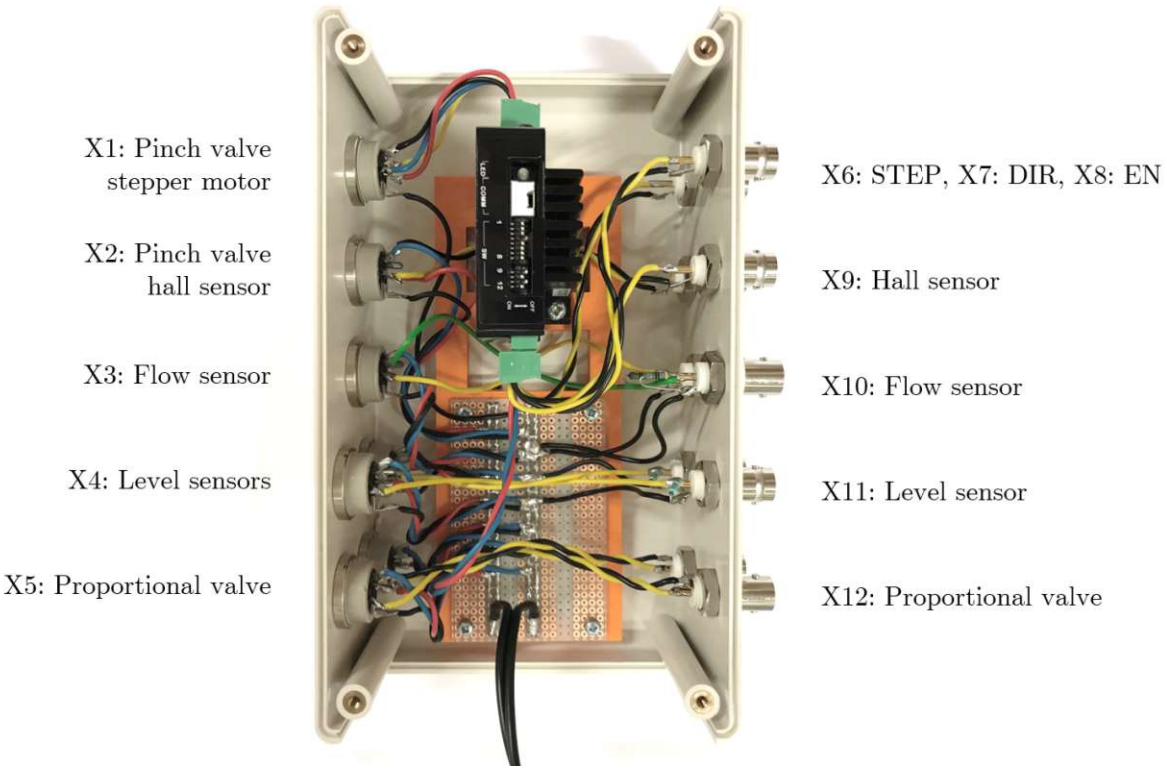

Figure B.4: Connection box B, connecting the pinch valve via X1, X6 (STEP), X7 (DIR) and X8 (EN) with the motor driver DRV-1. The inherent hall sensor of the pinch valve is connected by X2 and X9. The flow sensors are addressed by X3 and X10. The level sensors are conncted by X4 and X11. And the pneumatic proportional valves are connected according to X5 and X12.

B.2 Identification of components

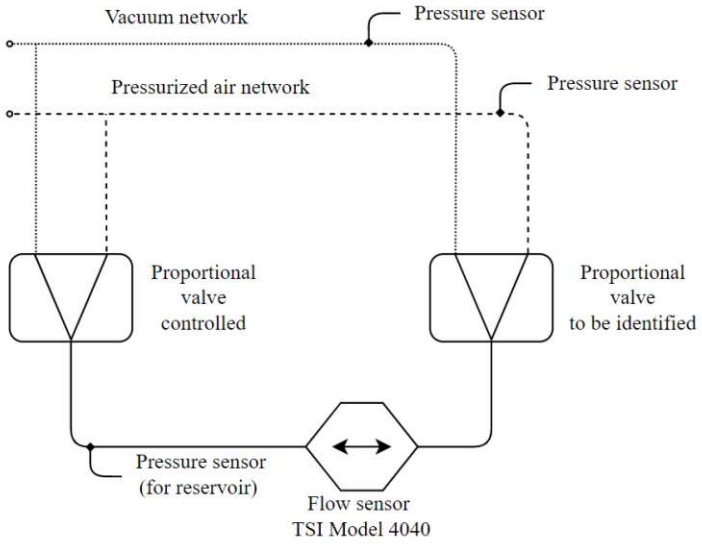

Figure B.5: Schematic diagram of the identification of the sonic conductance of one proportional valve, with corresponding supply and reservoir pressures.

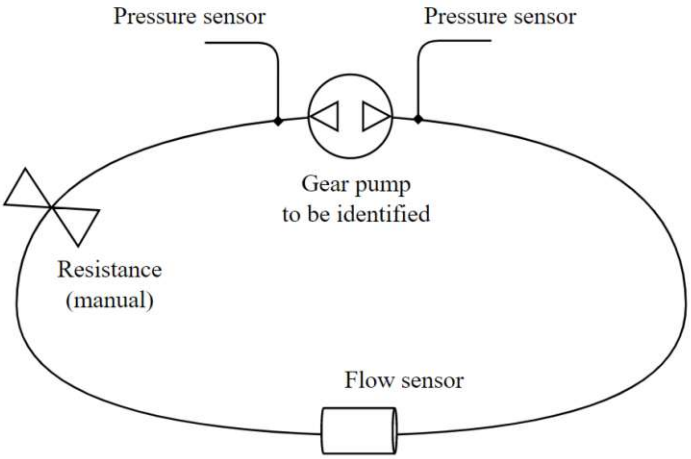

Figure B.6: Schematic diagram of the identification of the gear pump with a manual flow resistance, two pressure sensors measuring the resulting pressure difference across the pump and a flow sensor for the resulting flow.

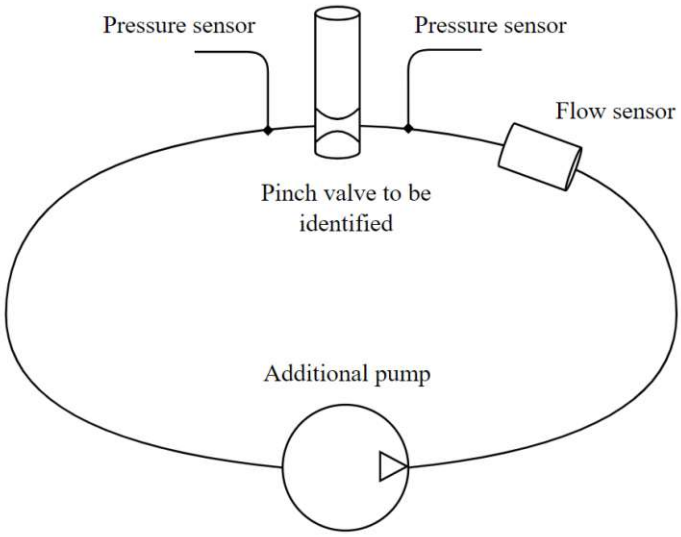

Figure B.7: Schematic diagram of the identification of the pinch of the pinch valve with an additional pump, two pressure sensors measuring the pressure loss across the pinch valve and a flow sensor.

B.3 Simulink implementation

Within this scope, the numerical simulation is described as representative for the atraumatic design. The simulation comprises a RUN file (.mat), which loads a data file (.mat) which has to be located in the same directory and initializes important variables needed to run the Simulink model (.sim), where the numerical model of the atraumatic design and the control strategy, as well as a defined reference input is implemented. The *reference* block comprises the cardiovascular model or equivalent reference curves, which are connected to the implemented control structure. The decoupling control law based on feedback linearisation is implemented Matlab function in *ctrl law v1,v2* and calculates the necessary mass flow rates inflating or deflating the reservoirs. As described this is based on the current states of the system and the pinch valve flow rate. Within the *input calculation* these mass flow rates are converted to the corresponding control voltages for the actuators based on ISO 6358 and the characteristic sonic conductance of each pneumatic proportional valve. Similarly the level control is implemented within *control one pulse* where the period of one cardiac cycle is stored within a buffer to calculate the running mean of all states. Subsequently the mean pinch valve position is controlled based on the mean level error and the resulting flow rate is calculated based on the current pressure difference and pinch valve position.
The mass flow rates and the resulting pinch valve flow rate form an input to the system, which is modelled according to (2.21) as a Level-2-MATLAB S-Function, which provides the new state values based on the system dynamics.

Implementation of the nonlinear decoupling control law (Matlab function in *ctrl law v1,v2*):

```
function [ctrl, xi31_dot, xi32_dot] = fcn(w, xi31, xi32, x, K,
    Kw, u3)

% x           [x1, x2, x3, x4, x5]
% xi          [xi1, xi2]
% w           [w1, w2]

% parameter values
A = 4185*1e-6;                                  % m^2
RV = 3.0536e-04;                                % m^3
PV = 2.3562e-05;                                % m^3
V = RV+PV;                                      % m^3
g = 9.81;                                       % m/s^2
R = 287.058;                                    % J/kg*K
T = 297.15;                                     % K
```

```
% output matrix
C = [ 0 0 1 0 0 ;          % y1 = pressure at pump inlet
      0 0 0 1 0 ;          % y2 = pressure at pump outlet
      0 1 0 0 0 ];         % y3 = level tank 2

% feedback linearisation with dynamic extension of output 1 and
   2
h1 = C(1,:)*x;
h2 = C(2,:)*x;
h3 = C(3,:)*x;

% l = [ Lfh1 ; Lfh2 ; Lfh3 ]
l = [-(x(3)*x(5))/(V - A*x(1));
    (x(4)*x(5))/(V - A*x(2));
    x(5)/A];

% J = [ Lg1h1 Lg2h1 Lg3h1;
%       Lg1h2 Lg2h2 Lg3h2;
%       Lg1h3 Lg2h3 Lg3h3;]
J = zeros(3);
J(1,1) = (R*T)/(V - A*x(1));
J(1,3) = x(3)/(V - A*x(1));
J(2,2) = (R*T)/(V - A*x(2));
J(2,3) =  -x(4)/(V - A*x(2));
J(3,3) =  -1/A;

% the state transformation
z = [h1;h2;h3;xi31;xi32];

% determination of input vector
v1 = -K(1,:)*z + Kw(1,1)*w(1);
v2 = -K(2,:)*z + Kw(2,2)*w(2);

u = J(1:2,1:2) \ ( [v1;v2]-l(1:2)-J(1:2,3)*u3 );
ctrl = u;

% time derivative of extended state xi
xi31_dot = xi32;
xi32_dot = u3;

end
```

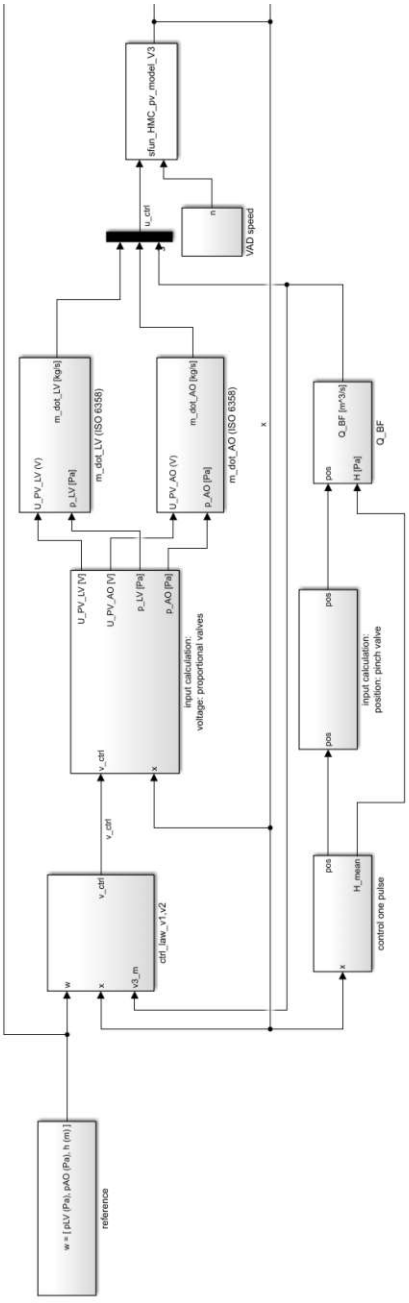

Figure B.8: Excerpt of the numerical simulation model of the atraumatic design implemented in Simulink.

B.4 Different application scenario

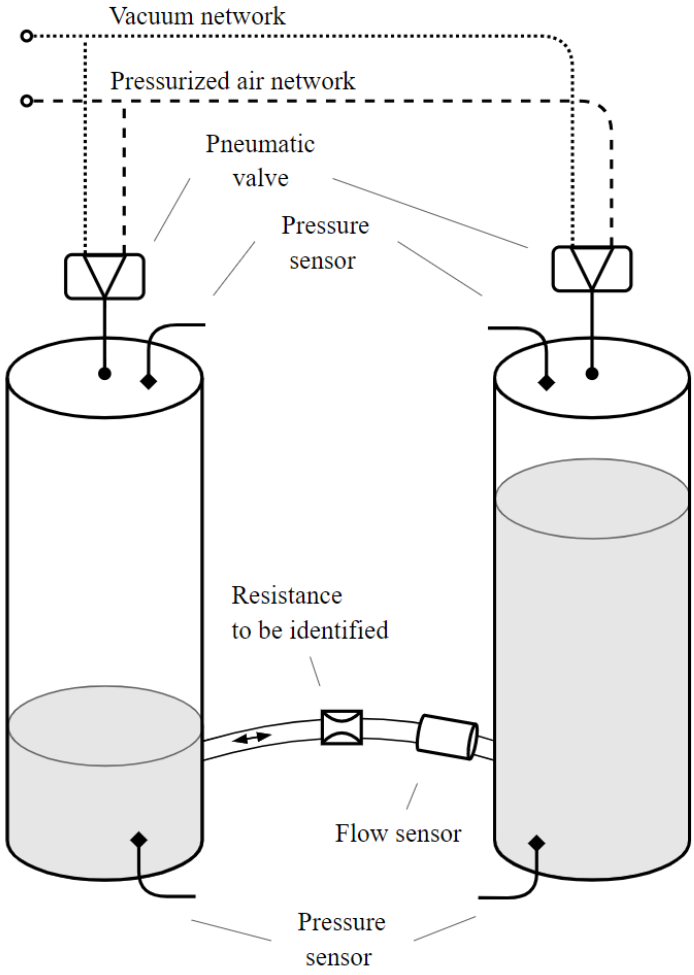

Figure B.9: Schematic representation of a setup without pumps for hemolytic assessments of hardware components disturbing the blood flow.

Within this application the reservoirs are alternately pressurized to generate a pressure gradient between the reservoirs which creates a steady flow. Accordingly blood is flowing from one reservoir to the other until a defined maximum level is met, then the pressurized reservoir switches automatically, which leads to the same pressure gradient with different sign and consequently a steady flow in the opposite direction. Therefore a chosen component e.g. a defined resistance is passed alternately with constant flow rate.
Of note, fluid height is calculated by the hydrostatic pressure of the fluid column, this is possible due to an additional pressure sensor at the bottom of each reservoir.

Bibliography

[1] Moritz Bender. *Development of a Hardware In the Loop (HIL) system to test implantable blood pumps*. Tech. rep. Vienna: Technical University of Vienna, 2022.

[2] European Heart Network. *Heart Failure and Cardiovascular Diseases – A European Heart Network Paper*. 2019. URL: https://ehnheart.org/publications-and-papers/publications/1202:heart-failure-and-cardiovascular-diseases.html.

[3] The Joint Commission. *New York Heart Association (NYHA) Classification*. URL: https://manual.jointcommission.org/releases/TJC2018A/DataElem0439.html.

[4] Eurotransplant. *Eurotransplant - Annual Report 2021*. 2022. URL: https://www.eurotransplant.org/wp-content/uploads/2022/06/Annual-Report-2021_LR.pdf.

[5] James K. Kirklin et al. "Eighth annual INTERMACS report: Special focus on framing the impact of adverse events". In: *The Journal of Heart and Lung Transplantation* 36.10 (Oct. 2017), pp. 1080–1086. DOI: 10.1016/j.healun.2017.07.005.

[6] Ezequiel J Molina et al. "The Society of Thoracic Surgeons Intermacs 2020 Annual Report." In: *The Annals of thoracic surgery* 111.3 (Mar. 2021), pp. 778–792. DOI: 10.1016/j.athoracsur.2020.12.038.

[7] Nir Uriel et al. "Hemocompatibility-Related Outcomes in the MOMENTUM 3 Trial at 6 Months". In: *Circulation* 135.21 (May 2017), pp. 2003–2012. DOI: 10.1161/CIRCULATIONAHA.117.028303.

[8] Johann Friedrich Gülich. "Partload operation, impact of 3-D flow phenomena performance". In: *Centrifugal Pumps*. Berlin, Heidelberg: Springer Berlin Heidelberg, 2008, pp. 187–256. DOI: 10.1007/978-3-540-73695-0{_}5.

[9] Stefan Boes et al. "Hydraulic Characterization of Implantable Rotary Blood Pumps". In: *IEEE Transactions on Biomedical Engineering* 66.6 (June 2019), pp. 1618–1627. DOI: 10.1109/TBME.2018.2876840.

[10] Malte Schöps et al. "Hemolysis at low blood flow rates: in-vitro and in-silico evaluation of a centrifugal blood pump". In: *Journal of Translational Medicine* 19.1 (Dec. 2021), p. 2. DOI: 10.1186/s12967-020-02599-z.

[11] Marcus Granegger et al. "Blood trauma potential of the HeartWare Ventricular Assist Device in pediatric patients". In: *The Journal of Thoracic and Cardiovascular Surgery* 159.4 (Apr. 2020), pp. 1519–1527. DOI: 10.1016/j.jtcvs.2019.06.084.

[12] Andreas Escher et al. “Hemolytic Footprint of Rotodynamic Blood Pumps”. In: *IEEE Transactions on Biomedical Engineering* 69.8 (Aug. 2022), pp. 2423–2432. DOI: 10.1109/TBME.2022.3146135.

[13] Samer S. Najjar et al. “An analysis of pump thrombus events in patients in the HeartWare ADVANCE bridge to transplant and continued access protocol trial”. In: *The Journal of Heart and Lung Transplantation* 33.1 (Jan. 2014), pp. 23–34. DOI: 10.1016/j.healun.2013.12.001.

[14] Randall C. Starling et al. “Unexpected Abrupt Increase in Left Ventricular Assist Device Thrombosis”. In: *New England Journal of Medicine* 370.1 (Jan. 2014), pp. 33–40. DOI: 10.1056/NEJMoa1313385.

[15] ASTM. *Standard Practice for Collection and Preparation of Blood for Dynamic in vitro Evaluation of Hemolysis in Blood Pumps*. 2019. DOI: 10.1520/F1830-19.

[16] ASTM. *Standard Practice for Assessment of Hemolysis in Continuous Flow Blood Pumps*. 2021. DOI: 10.1520/F1841-19E01.

[17] Femke Cappon et al. “Mock circulatory loops used for testing cardiac assist devices: A review of computational and experimental models”. In: *International Journal of Artificial Organs* 44.11 (Nov. 2021), pp. 793–806. DOI: 10.1177/03913988211045405.

[18] Shaun D. Gregory et al. “An advanced mock circulation loop for in vitro cardiovascular device evaluation”. In: *Artificial Organs* 44.6 (June 2020). DOI: 10.1111/aor.13636.

[19] Gregor Ochsner et al. “A Novel Interface for Hybrid Mock Circulations to Evaluate Ventricular Assist Devices”. In: *IEEE Transactions on Biomedical Engineering* 60.2 (Feb. 2013), pp. 507–516. DOI: 10.1109/TBME.2012.2230000.

[20] Francesco Maria Colacino et al. “A Modified Elastance Model to Control Mock Ventricles in Real-Time: Numerical and Experimental Validation”. In: *ASAIO Journal* 54.6 (Nov. 2008), pp. 563–573. DOI: 10.1097/MAT.0b013e31818a5c93.

[21] Sunil Gupta et al. “Normalisation of Haemodynamics in Patients with End-stage Heart Failure with Continuous-flow Left Ventricular Assist Device Therapy”. In: *Heart, Lung and Circulation* 23.10 (Oct. 2014), pp. 963–969. DOI: 10.1016/j.hlc.2014.04.259.

[22] Peter Beater. *Pneumatic Drives*. Berlin, Heidelberg: Springer Berlin Heidelberg, 2007. DOI: 10.1007/978-3-540-69471-7.

[23] Anders Hedegaard Hansen. *Fluid Power Systems*. Vol. 129. Cham: Springer International Publishing, 2023. DOI: 10.1007/978-3-031-15089-0.

[24] Giancarlo Pennati et al. “Mathematical Modeling of Fluid Dynamics in Pulsatile Cardiopulmonary Bypass”. In: *Artificial Organs* 28.2 (Feb. 2004), pp. 196–209. DOI: 10.1111/j.1525-1594.2003.47197.x.

[25] Stefan Jakubek and Christoph Hametner. *Prozessregelung*. Vienna University of Technology, 2022.

[26] Alberto Isidori. “Nonlinear Control Systems”. In: Communications and Control Engineering (1995). DOI: 10.1007/978-1-84628-615-5.

[27] Christoph Hametner, Stefan Jakubek, and Sebastian Thormann. *Zustandsregelung von Mehrgrößensystemen*. Vienna University of Technology, 2020.

[28] Hassan K Khalil. *Nonlinear Systems*. London: Prentice Hall, 2002.

[29] J. Lofberg. “YALMIP : a toolbox for modeling and optimization in MATLAB”. In: *2004 IEEE International Conference on Robotics and Automation (IEEE Cat. No.04CH37508)*. IEEE, pp. 284–289. DOI: 10.1109/CACSD.2004.1393890.

[30] The MathWorks. *Rise time, settling time, and other step-response characteristics - MATLAB stepinfo - MathWorks Deutschland*. URL: https://de.mathworks.com/help/ident/ref/dynamicsystem.stepinfo.html.

[31] Kevin Bourque et al. “Design Rationale and Preclinical Evaluation of the HeartMate 3 Left Ventricular Assist System for Hemocompatibility”. In: *ASAIO Journal* 62.4 (July 2016), pp. 375–383. DOI: 10.1097/MAT.0000000000000388.

[32] Eva Woelke et al. “Validation of a Miniaturized Test Loop for the Assessment of Human Blood Damage by Continuous-Flow Left-Ventricular Assist Devices”. In: *Annals of Biomedical Engineering* 49.12 (Dec. 2021), pp. 3165–3175. ISSN: 0090-6964. DOI: 10.1007/s10439-021-02849-1.

[33] *Adobe Stock*. URL: https://stock.adobe.com/de/images/circulation-of-blood-through-the-heart-cross-sectional-diagram-of-the-heart-vector-illustration-of-great-and-small-circles-of-blood-circulation/294695184.

[34] Steffen Leonhardt and Marian Walter. *Medizintechnische Systeme*. Ed. by Steffen Leonhardt and Marian Walter. Berlin, Heidelberg: Springer Berlin Heidelberg, 2016. DOI: 10.1007/978-3-642-41239-4.

[35] Karl Kroemer, Hiltrud Kroemer, and Katrin Kroemer-Elbert. “Circulation”. In: *Engineering Physiology: Bases of Human Factors Engineering/ Ergonomics*. Cham: Springer International Publishing, 2020, pp. 153–172. DOI: 10.1007/978-3-030-40627-1{_}6.

[36] Francis D. Pagani. “Understanding the Principles of Continuous-Flow Rotary Left Ventricular Assist Devices”. In: *Mechanical Circulatory Support: a Companion to Braunwald’s Heart Disease*. Elsevier, 2020, pp. 71–81. DOI: 10.1016/B978-0-323-56699-5.00007-3.

[37] J. Timothy Baldwin and John T. Watson. “Historical Aspects of Mechanical Circulatory Support”. In: *Mechanical Circulatory Support: a Companion to Braunwald’s Heart Disease*. Elsevier, 2020, pp. 1–7. DOI: 10.1016/B978-0-323-56699-5.00001-2.

[38] Howard J. Eisen. “Left Ventricular Assist Devices (LVADS): History, Clinical Application and Complications”. In: *Korean Circulation Journal* 49.7 (2019), p. 568. DOI: 10.4070/kcj.2019.0161.

[39] *Abbott Laboratories*. URL: https://www.cardiovascular.abbott/us/en/hcp/products/heart-failure/left-ventricular-assist-devices/heartmate-3/about/system-overview.html.

[40] Jeff Larose and Daniel Timms. "Hemocompatibility in Mechanical Circulatory Support". In: *Mechanical Circulatory Support: a Companion to Braunwald's Heart Disease*. Elsevier, 2020, pp. 83–89. DOI: 10.1016/B978-0-323-56699-5.00008-5.